INVESTIGATION OF THE MADARAS WIND TURBINE USING COMPUTATIONAL TOOLS

By

Philip David Ingram

Thesis

Submitted to the Faculty of the

Graduate School of Vanderbilt University

in partial fulfillment of the requirements

for the degree of

MASTER OF SCIENCE

in

Mechanical Engineering

December, 2012

Nashville, Tennessee

Approved:

Professor Alvin M. Strauss

Professor Jon F. Edd

Professor Thomas J. Withrow

For my loving mother and father.

ACKNOWLEDGEMENTS

I would first and foremost like to thank my advisor Dr. Alvin Strauss for his guidance during this research. I would also like to thank the Tennessee Space Grant Consortium whose funding made this research possible. In addition, I would like to thank Dr. Haoxiang Luo whose expertise in computational fluid dynamics guided the creation and validation of accurate CFD models, and Drs. Jon Edd and Thomas Withrow who reviewed my thesis and ensured the overall accuracy of this document.

I would like to thank the members of the Vanderbilt University Welding Automation Laboratory, especially Chase Cox and Brian Gibson whose advice helped steer this research in the correct directions. I would also like to thank Dr. Nilanjan Sarkar of the Graduate Studies department, Brenda Jordan of the registrar’s office, Suzanne Weiss of the mechanical engineering department, and Myrtle Daniels of the mechanical engineering department for their guidance and help throughout this process.

Finally, I would like to thank my family, especially my parents, Terri and David, and my brother, Peter. You are the backbone of all that I have done, and without your support none of this would have been possible.

TABLE OF CONTENTS

LIST OF TABLES

LIST OF FIGURES

LIST OF NOMENCLATURE

Symbol	
AISI	American Iron and Steel Institute
AR	Aspect Ratio [m/m]
AWEA	American Wind Energy Association
α	Ratio between rotational and translational velocity
BH	Boundary Height [m]
C	Circumferential edge of the cylinder [m]
CFD	Computational Fluid Dynamics
C_L	Coefficient of lift
C_D	Coefficient of drag
CH	Cap Height [m]
d	Diameter [m]
ds	Arc length element along the circumference [m]
DOE	Department of Energy
e/d	Ratio of end cap diameter to cylinder diameter [m/m]
EPA	Environmental Protection Agency
F_i	Force in the i-direction [N]
f_n	Interference loss factor
FEA	Finite Element Analysis
Γ	Vortex intensity [m^2/s]
HAWT	Horizontal Axis Wind Turbine
μ	Dynamic viscosity [kg/(m*s)]
n	Unit vector normal to the cylinder
N	Number of cars in a plant
NREL	National Renewable Energy Laboratory
ω	Rotational speed [rad/s]
p	Static pressure [N/m^2]
φ	Angle between the normal and vertical vectors

r	Radius [m] or Separation distance [m]
Re	Reynolds number
ρ	Density [kg/m^3]
RPM	Revolutions per Minute [rev/min]
r_x	Separation distance in the x-direction
r_y	Separation distance in the y-direction
t	Time [s]
U_w	Wall speed [m/s]
v	Translational velocity [m/s]
VAWT	Vertical Axis Wind Turbine
w	Complex potential of the flow

CHAPTER I

INTRODUCTION

Thesis Objective and Scope

The goal of this thesis is to analyze the performance of a Madaras wind turbine (as described in the section below) if it were built with modern equipment and by modern processes. The most comprehensive analysis of a Madaras wind turbine to date was performed by a team from the University of Dayton Research Institute and commissioned by the Department of Energy [Whitford et al., 1978]. Their technical report was published over thirty years prior to this work, and in the decades between, the field of engineering has changed dramatically. Although new technologies, new materials, new techniques, and new processes significantly impact the performance and cost of a Madaras-type power plant, the scope of this study does not extend to the materials and processes, but instead focuses upon the analysis of a Madaras wind turbine using computational technologies including computational fluid dynamics (CFD) and finite element analysis (FEA).

Using the CFD package produced by COMSOL, single and multi-rotor Madaras wind turbine systems are modeled, and the result of these computational fluid dynamic studies validate the past work performed on these turbines. This study will briefly discuss the mechanical structure of the turbines; however, it will not go into significant structural analysis, analyze the electronic system of the turbines, or determine the optimal geographical placement of them. Control of the system in general is outside the scope of this study.

Madaras Power Plant

The Madaras power plant is named after Julius Madaras who first proposed placing rotating cylinders on top of railcars traversing a circular path and using them to generate electricity. The force that propels the cars forward along the track is due to the Magnus effect, which is described in a section of the same title below. As the cars are propelled forward by this force, the wheels in contact with the track rotate, and a generator connected to the wheels through a system of gears converts the kinetic power into electrical power. As shown in figure 1, Madaras envisioned a circular or near-circular path with the cars situated on top of rails. In his original design, there were 18 cable-connected cars with a total electrical output of 18 MW traveling around a 457 m diameter track. He also considered a 75 car 100 MW system [Whitford et al., 1978].

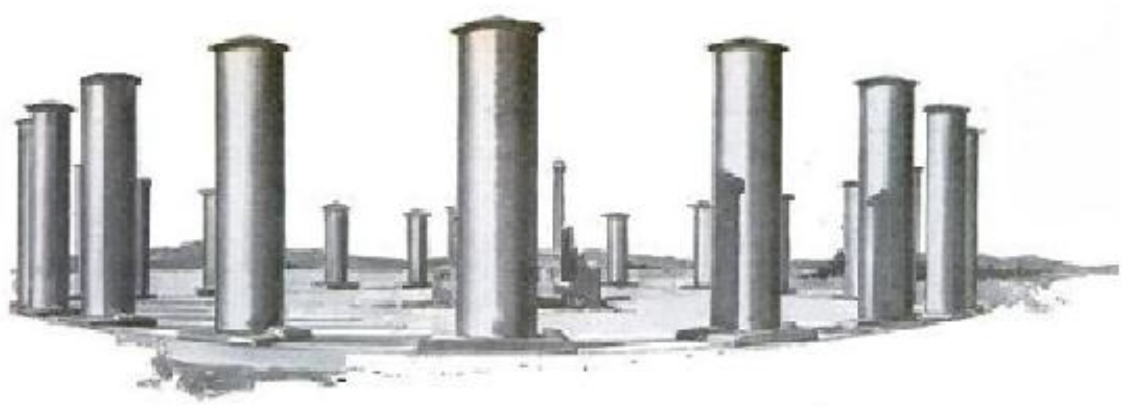

Figure 1: Madaras power plant configuration [Whitford et al., 1978]

The original parameters for the Madaras power plant are given in table 1 below. Julius Madaras built a prototype of one of these full-size cylinders to determine the forces acting upon the cylinder and to prove his concept. He also calculated the optimal track speed to be 13.4 m/s for a mean wind speed of 8.1 m/s [Whitford et al., 1978]. Of note in the parameter tables are the high weight and the large width of the car. These were probably specified to counter a large tipping moment and produce enough normal force to turn the generator without permitting the wheels to slip on the track.

Table 1: Madaras parameters [Whitford et al., 1978]

Cylinder:

Aspect ratio	8
e/d ratio	2
Diameter	4.9 m
Length	38.1 m
End-plate diameter	9.8 m
Rotation speed	186 rpm

Cars:

Height	3.8 m
Length	19.2 m
Width	17.4 m
Weight	328,000 kg
Gauge	11 m

Table 2: Whitford et al. turbine scenario

Rotor and Car Geometry

Aspect ratio	8
Rotor diameter	4.9 m
Cylinder length	38.1 m
End cap diameter	9.8 m
e/d ratio	2
Car weight	328,000 kg
Rotor mid-height	25 m

Plant Geometry

Track gauge	11 m
Track end diameter	1372 m
Track straight section	18,300 m
Area encompassed	7209 acres
Net area purchased *	748 acres
Number of cars	190
Spacing between cars	215 m

*Area encompassed = Net area purchased + area used for other purposes (such as farming)

Operational Conditions

Track speed	11.2 m/s
Rated wind speed	13.4 m/s
Cut-out windspeed	29 m/s
Rotor rotational speed	186 RPM
Viscous braking	

Electrical Equipment

Spin motor -- 450 kW, 500 VDC
Generator -- 1 per car, 4160 V, 60 Hz

Performance

Rated capacity – 227.8 MW
Annual energy yield:
975.4*10^6 kWh at V=8.1 m/s, at sea level
947.7*10^6 kWh at V=9.7 m/s, elevation of 2130 m

Based upon the calculations of Whitford et al., a plant consisting of Madaras turbines should be comparable in power production to a plant of horizontal axis wind turbines (HAWTs). Whitford et al. calculated that the installed cost of a Madaras plant would be $1026/ kW versus $994/kW for a comparable HAWT plant (1978 dollars). The cost they calculated for the Madaras plant includes material, fabrication, location, and other costs. They note that their method of evaluating the Madaras plant is conservative, so the actual cost of a Madaras plant may be even lower. It should be kept in mind that technological advances affect both Madaras wind turbines and traditional wind turbines. Undoubtedly more research has gone into improving the design of the large commercial wind turbines and for this reason it is likely that if the same time and money were invested in Madaras turbine research the gains would be greater. For this reason it is incredibly difficult to compare the costs of the turbines today without a comprehensive study.

The most efficient plant that Whitford et al. were able to design had the parameters given in table 2. These were obtained by testing scaled models in a wind tunnel. Some of these parameters have clearly carried over from the previous study done by Julius Madaras and his team: the turbine diameter selected is still 4.9 meters, the car weight is 328,000 kg, the rotational speed of the turbine is 186 RPM, and the track gauge is 11 meters. Still others are clearly a result of their study. They were able to more accurately describe the parameters of the track as well as the power production that could be expected from this type of setup. Clearly, more research must be performed to truly find the optimized Madaras turbine parameters.

Magnus Effect

The Madaras wind turbine operates upon the principle of the Magnus Effect, which describes the interaction between a moving fluid and a spinning body. When a fluid flows past a spinning body, its path is disrupted by shear interaction with the surface of the body [Borg et al., 1986]. As can be seen in figure 2, the flow decelerates near the side of the cylinder that has a streamwise translational velocity opposing the direction of the flow and accelerates near the side that has a streamwise translational velocity in the direction of the flow. This is termed the Magnus effect after Heinrich Gustav Magnus, the German physicist credited with discovering it.

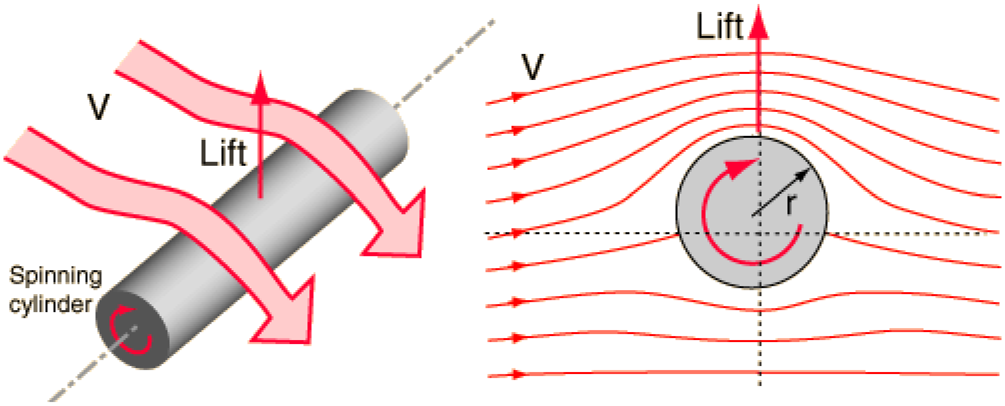

Figure 2: Magnus effect on a cylinder [Borg et al., 1986]

The idea of Julius Madaras was to harness the force produced by the Magnus effect and use it to produce power. Many others had previously utilized this force (probably without truly understanding the physics behind it), to accomplish other goals, specifically in the realm of sports. For ages, tennis players have created top spin with their rackets, baseball pitchers have thrown sideways-deflecting curveballs, and soccer players have “bent” soccer balls; however, Julius Madaras was the first to conceive of a means of producing electricity with the Magnus effect.

Mathematical Formulation

The Kutta-Joukowski Theorem, named after the German and Russian scientists who first derived it, describes the lift caused by a spinning cylinder that is perpendicular to a fluid flow. Kutta and Joukowski treated the flow of the fluid over the cylinder as the superposition of a translational flow and a rotational flow as shown in figure 3. The derivation that follows is found in the book *An Introduction to Fluid Dynamics* [Batchelor, 1967].

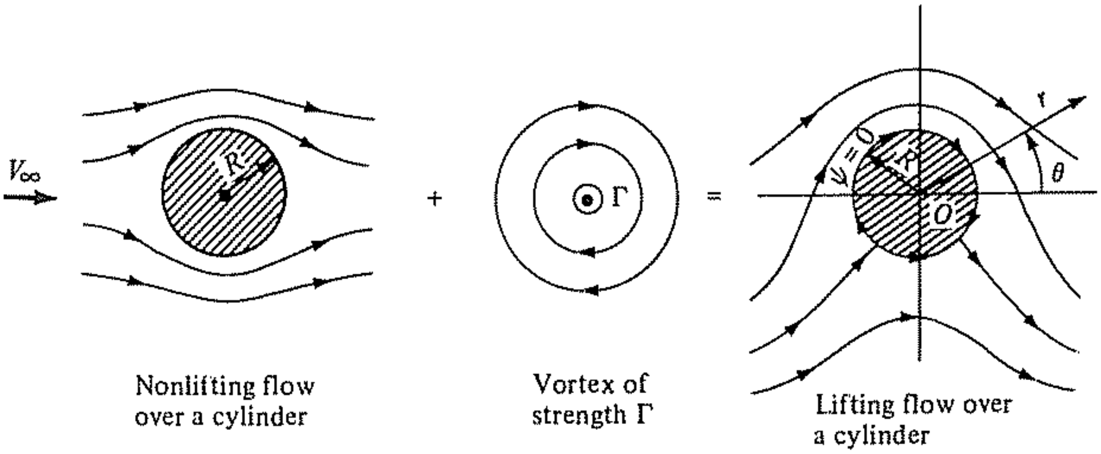

Figure 3: Superposition of vortex [Batchelor, 1967]

The derivation begins with the determination of the force exerted on a unit length of a cylinder of arbitrary cross-section.

$$\boldsymbol{F} = -\oint_C p\boldsymbol{n}\, ds$$

where C is the circumferential edge of the cylinder, p is the static pressure of the fluid, $\boldsymbol{n}$ is the unit vector that is normal to the cylinder, and ds is the arc length element along the circumference. Let φ be the angle between the normal and vertical vectors. The force can then be broken into x and y components.

$$F_x = -\oint_C p \sin\varphi \, ds \qquad \text{and} \qquad F_y = \oint_C p \sin\varphi \, ds$$

Consider the two-dimensional space (x, y) as a complex plane so that each Cartesian vector can be represented by a real component and an imaginary component.

$$F = F_x + iF_y = -\oint_C p\,(\sin\varphi - i\sin\varphi) ds$$

Some simple algebraic manipulation and the application of Euler's formula yield the following:

$$\begin{aligned} \bar{F} &= -\oint_C p\,(\sin\varphi + i\cos\varphi) ds \\ &= -i\oint_C p(\cos\varphi - i\sin\varphi) ds \\ &= -i\oint_C p\, e^{-i\varphi} ds \end{aligned}$$

Surface segments ds are related to the changes dz along them by:

$$dz = dx + idy = ds(\cos\varphi + i\sin\varphi) = ds\, e^{i\varphi}$$

$$d\bar{z} = e^{-i\varphi} ds$$

The result of substituting the expression above into the integral is

$$\bar{F} = -i\oint_C p\, d\bar{z}$$

The Bernoulli equation is used to eliminate the pressure from the integral

$$p = p_0 - \frac{\rho v^2}{2}$$

and substituting it in gives

$$\bar{F} = -ip_0 \oint_C \; d\bar{z} + i\frac{\rho}{2}\oint_C \; v^2 d\bar{z}$$

$$= \frac{i\rho}{2}\oint_C \; v^2 d\bar{z}$$

The next step is to introduce the complex potential of the flow, which is defined as $w = f(z)$. The complex potential can be related to the velocity components as $w'(z) = v_x - iv_y$ where *w'* is the derivative of the complex potential. Manipulating and substituting this into the force equation results in the expression below.

$$F = \frac{i\rho}{2}\oint_C \; w'^2 \, dz$$

This holomorphic function can be written as a Laurent equation. From the physics of the problem, the form of the derivative of the complex function is deduced:

$$w'(z) = a_0 + \frac{a_1}{z} + \frac{a_2}{z^2} + \cdots$$

The Laurent equation does not contain higher order terms because the velocity remains constant at infinity. The derivative of the function at infinity equals a_o, which implies that $a_0 = v_{x\infty} - iv_{y\infty}$. Using the residue theorem on the above series and integrating, a_1 can be determined:

$$a_1 = \frac{1}{2\pi i}\int_C \; w'(z)dz$$

$$\oint_C \; w'(z)dz = \oint_C \; \left(v_x - iv_y\right)(dx + idy)$$

$$= \oint_C \; \left(v_x dx + v_y dy\right) + i\oint_C \; \left(v_x dy - v_y dx\right)$$

$$= \oint_C \boldsymbol{v}\, ds + i \oint_C (v_x dy - v_y dx)$$

The first integral is the circulation, which is denoted by Γ. The second integral can be evaluated as below when φ is the stream function.

$$\oint_C (v_x dy - v_y dx) = \oint_C \left(\frac{\partial\varphi}{dy} dy + \frac{\partial\varphi}{dx} dx\right) = \oint_C d\varphi = 0$$

Since the border of the cylinder *C* is a streamline, the stream function does not change over it, and $d\varphi = 0$. The result is

$$a_1 = \frac{\Gamma}{2\pi i}$$

Taking the square of the series yields

$$w'^2(z) = {a_0}^2 + \frac{a_0 \Gamma}{\pi i z} + \cdots$$

Plugging this back into equation the previous equation and integrating using the residue theorem gives

$$\begin{aligned} F &= \frac{i\rho}{2}\left[2\pi i \frac{a_0\Gamma}{\pi i}\right] = i\rho a_0 \Gamma = i\rho\Gamma\left(v_{x\infty} - i v_{y\infty}\right) \\ &= \rho\Gamma v_{y\infty} + i\rho\Gamma v_{x\infty} \\ &= \quad F_x \quad + \quad iF_y \end{aligned}$$

Wind Power in the US

In the first quarter of 2012, the construction of 1695 megawatts of wind turbines brought the total cumulative installed capacity in the US to 48,611 MW, which is second only to China’s capacity of 62,000 MW [AWEA, 2012]. In February of 2012, the United States saw the production of 11 terawatt-hours of energy, or 3.6% of all electric power, from wind power sources. In addition, wind power capacity in the US is increasing such that it has doubled and will double again in three years. Looking at the current trends, EPA has stated that by 2030 wind power could generate 20% of the US's power. In light of both the concerns over nuclear fission caused by the incident in Fukushima, Japan and renewable power targets set by many developed countries, wind power is more important than ever before.

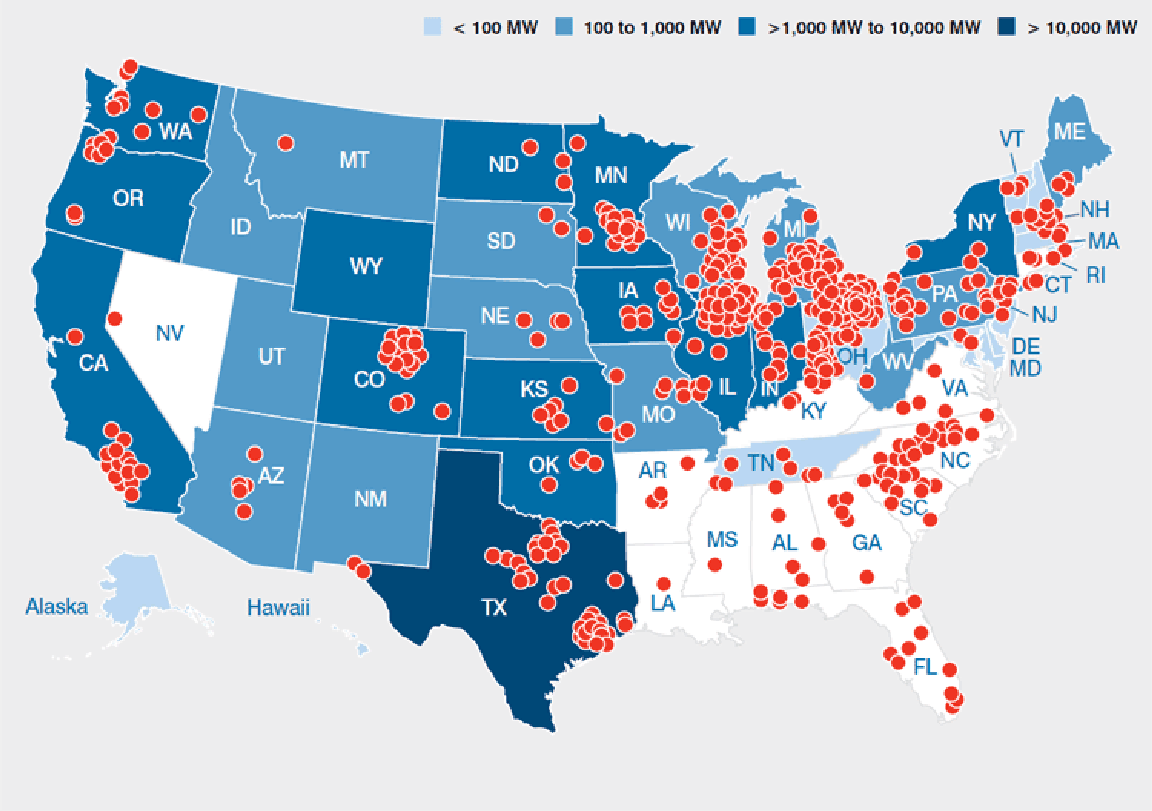

Figure 4: Wind turbines in the United States [AWEA, 2012]

Currently, the United States has 101 large wind farms, classified as producing 120 MW or more. Almost all of these wind farms use exclusively horizontal axis wind turbines.

Although pushes have been made to expand the market to include more novel designs such as vertical axis wind turbines (VAWTs), these are not prevalent in the United States today. Similarly, a Madaras plant has never been used in any country in the past due to the fact that its design is less well-developed than that of traditional wind turbines.

Conventional Wind Turbines

There are two main types of conventional wind turbines: horizontal axis wind turbines and vertical axis wind turbines. In the figures below, the difference as described by the name is clear – the orientation of the axis depends upon the type of turbine. In the case of VAWTs, the axis points skyward, and the turbine blades circle about the structural members of the turbine; in HAWTs the blades are located at the top of the turbine and face into the wind. Another important difference between HAWTs and VAWTs is the placement of the electromechanical components: the horizontal axis wind turbine has all of the electromechanical components elevated to the same height as the axis, creating a top-heavy structure, whereas the electromechanical components in a VAWT are located at the base, reducing weight supported by the turbine's central support.

Horizontal Axis Wind Turbines

One characteristic of the HAWT is the dependence on directionality. Small wind turbines are pointed by a vane extending off the back of the axis whereas large wind turbines are positioned by a wind sensor coupled with a servo motor so that they are pointing into the wind. The blades are placed in front of the tower to avoid interference from the tower and are pitched electronically to the optimal setting depending upon the wind speed. Because the blades are in front of the tower, they must be stiffened to prevent them from bending and rubbing against the tower in high winds. Modern commercial wind turbines have blades in length from 20 to 40 meters, towers that are 60 to 90 meters tall, tip velocities of up to 320 kilometers per hour, and complex gear systems.

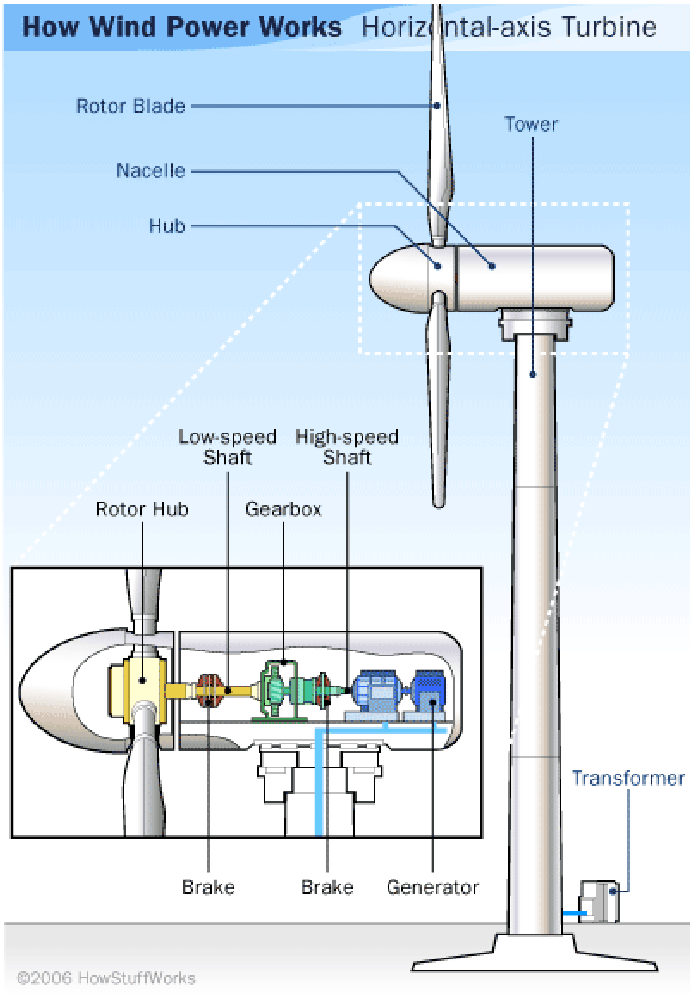

Figure 5: Horizontal axis wind turbine schematic [Layton, 2006]

Vertical Axis Wind Turbines

In comparison, VAWTs have the main rotor axis rotated 90 degrees so that it is perpendicular with the ground. One advantage of this orientation is that the wind turbine is directionally independent, which reduces the electronics required for operation and makes it more responsive in gusty wind conditions. Another advantage is the location of the gearbox and generator at the base of the turbine, which allows for more easy service and maintenance and requires less structural support from the main support. Some disadvantages of this design include the lower rotational speeds with higher torques (requiring a more expensive drive train), the lower power coefficient, and the continual 360 degree rotation of the heavy blades, which results in a highly dynamic loading on the turbine. One other disadvantage of VAWTs is that they are placed on the ground and can experience wind shear or lower wind speeds due to the placement of part of the blade close to the ground. As can be seen in figure 7, due to boundary layer effects much of the air close to the ground is stagnant or near-stagnant, a problem that is not as relative to HAWTs where the blades are elevated tens of meters above the ground. Due to the design of VAWTs and HAWTs, the latter are more efficient in low wind speeds whereas the former are more efficient in high wind speeds. One other item to note is that HAWTs are a much more popular choice for wind power plants, and there are very few VAWT plants in existence today.

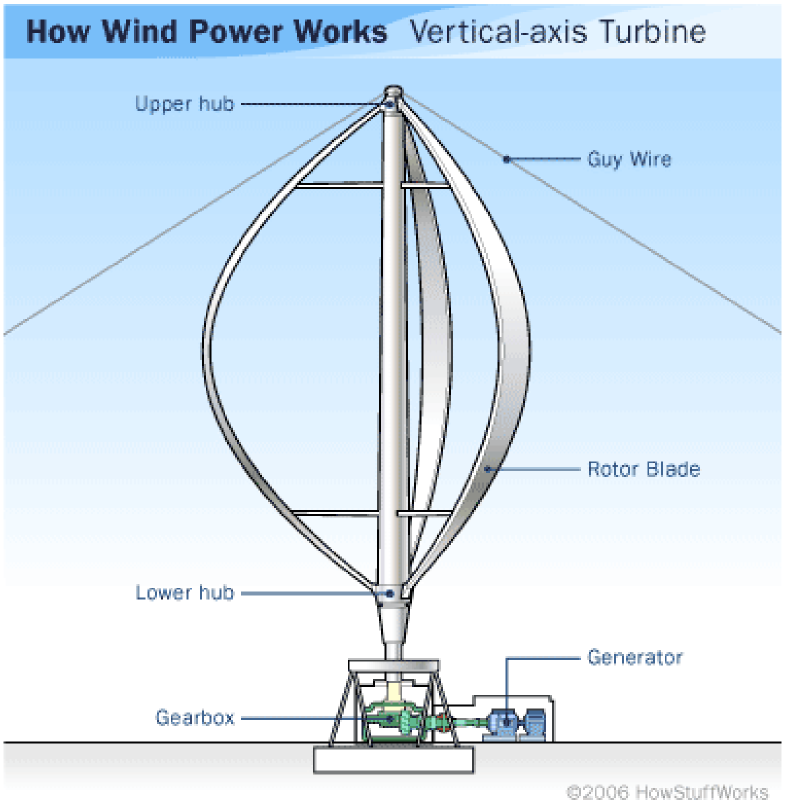

Figure 6: Vertical axis wind turbine schematic [Layton, 2006]

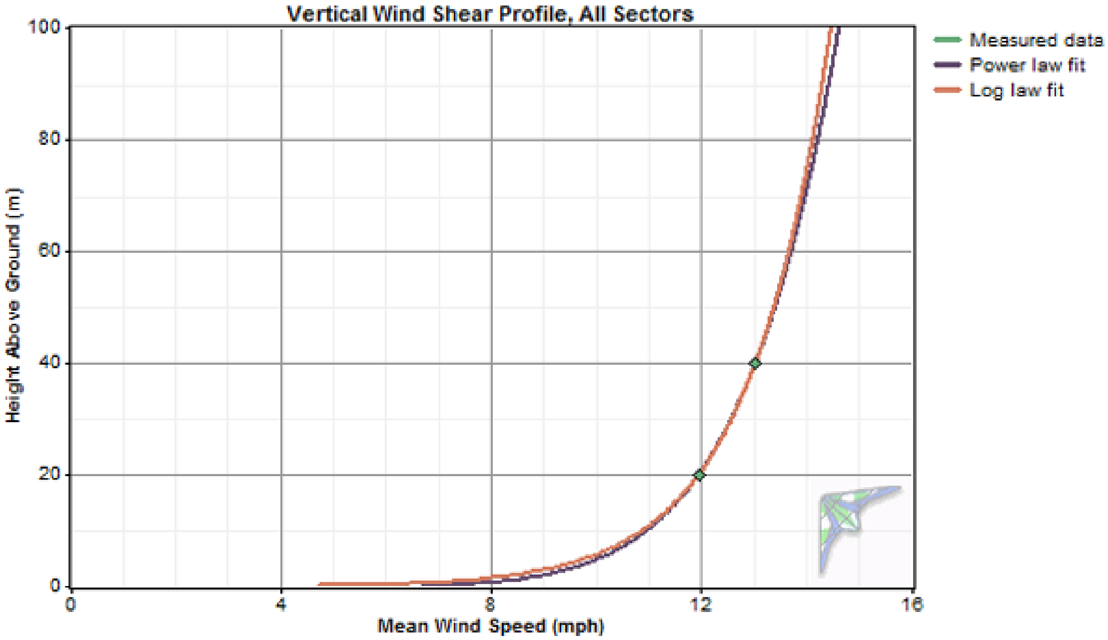

Figure 7: Schematic of wind shear [Lichtabch, 2009]

Advantages of the Madaras Plant

Total Height

One major advantage the Madaras plant has over horizontal axis wind turbines is its structural rigidity. The cylinder, which is the largest component of the system, is 38.1 meters in length. For comparison, a standard wind turbine may have blades 40 meters in length at a height of 80 meters. Clearly, the loads that the bases of wind turbines experience, particularly bending loads, are much greater than the loads that the track of the Madaras plant will experience at the base of the cars' wheels. In addition, the structural reinforcement that goes into the cylinders will be much less than that of HAWT blades and will therefore also cost less. This structural reinforcement can be done on the interior of the cylinders where there is space for bracing. Wind turbine blades, on the other hand, are much thinner and therefore much more complicated to brace.

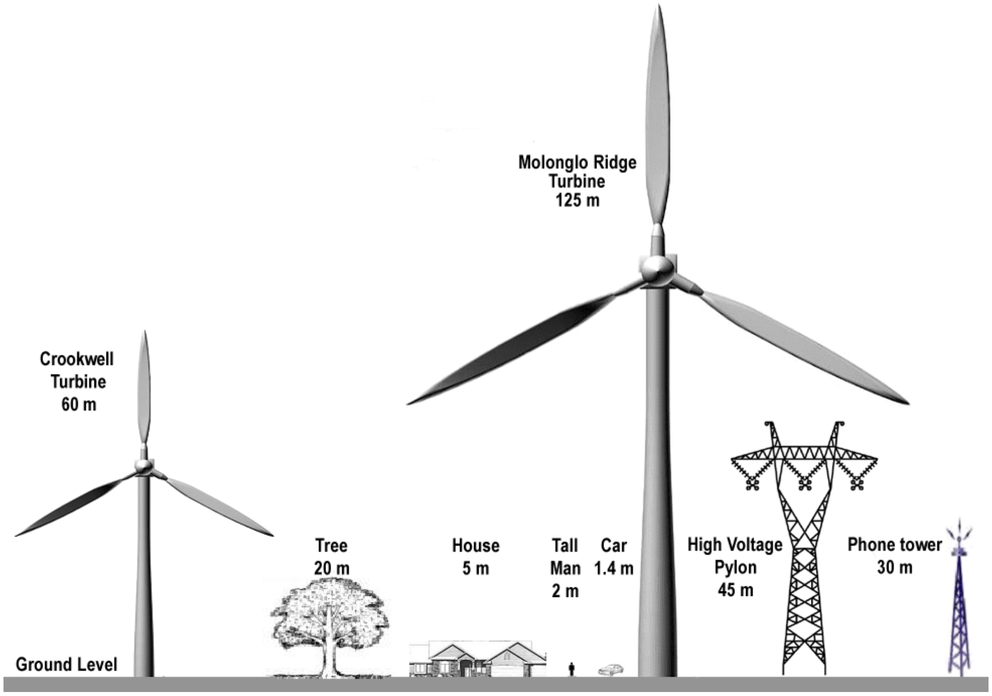

Figure 8: Comparing wind turbine heights to those of other common objects

An added benefit of a lower tower height is that Madaras wind turbines make much less of a visual impact on the landscape. Many people complain that traditional 120 meter tall wind turbines negatively impact the view. This causes housing prices to fall in some places close to wind farms. Madaras turbines, on the other hand, are much lower to the ground and therefore are less visible from a distance.

Environmental Impact

The case can be made that the Madaras wind turbine is more environmentally friendly than either VAWTs or HAWTs. Due to the low velocities of the track cars (no higher than about 10 m/s), it would be easier for birds to avoid collisions with the Madaras turbines. The tips of HAWT blades, in comparison, can move at speeds up to 91 m/s, and the complex open shape of the VAWT could trap and injure wildlife. Estimates of the mortality rates of birds vary greatly depending upon which organization is reporting them. The wind industry estimates that around 58,000 birds are killed by wind turbines in the US whereas the US Fish and Wildlife Service estimate is much greater at 440,000 birds each year. Regardless of the exact number, the design of the Madaras turbine could reduce the bird fatalities caused by wind turbines.

Lift Coefficient

The most important advantage of the Madaras turbine is the high lift coefficient. The rotating cylinders have lift coefficients that are about ten times greater than those of airfoils [Whitford et al., 1978]. This is significant because these turbines can theoretically produce ten times the power produced by a comparable vertical axis wind turbine. Of course, this theoretical limit is not achieved because of the power input to the cylinders, the complexities of turbine location on the track, and the energy required reversing the direction of the cylinder’s rotation. This will be further covered in the next section.

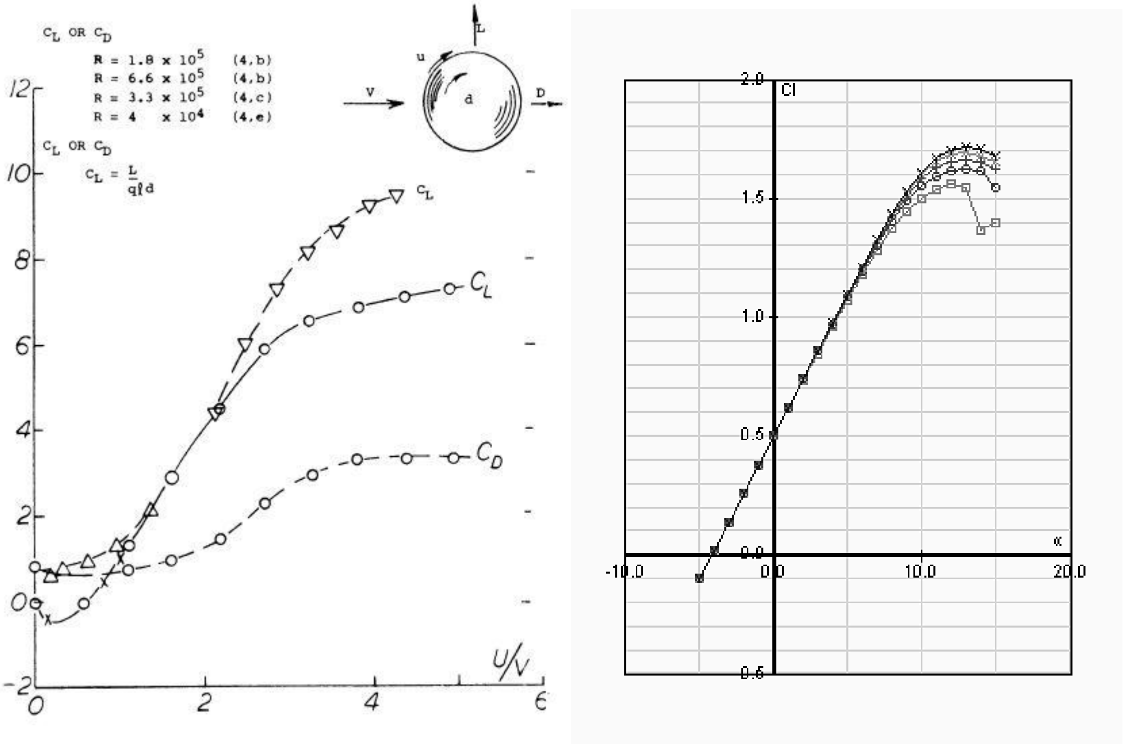

Figure 9: Coefficient of Lift comparison between rotating cylinder (left) and NACA 4412 (right)

Challenges for the Madaras Plant

The design of a Madaras power plant must overcome many hurdles. The most important are described below, and while some of these are common to all wind-powered electricity-producing plants such as the large tipping moments and the spacing between turbines, others such as the reversal of cylinder rotation are unique to the Madaras power plant.

Tipping Moment

An important technical challenge for the creation of an operational Madaras plant is the large tipping moment that the tall cylinders incur on the cars. Due to their large moment arm, a gust of wind could tip over a car if it were not properly balanced and weighed down. This was the reason that the cars of the Madaras plant weighed 328,000 kg and had a width of 17.4 m. In addition, the cars are designed to run on a track with a gauge of 11 m, which should adequately spread the weight out and avoid damaging the structural supports of the track.

One feasible solution to this tipping moment problem which would not involve a heavy car structure is to instead include a weight that shifts depending upon how much restoring moment is required. The weight could be set upon a track running through each car that is perpendicular to both the axis of movement of the cars and the axis of the cylinder. As the cars slowly revolve about the center of the track, the weight could move closer or farther from the car's center of gravity to counteract the changing magnitude of the tipping moment created by the tall cylinders.

Reversing the Cylinder Rotation

Another difficulty to overcome when designing a Madaras plant is the problem of stopping and restarting the rotation of the cylinder each time it passes the point in the track where the air velocity is parallel to the track. If the cars are originally turning counterclockwise and they go through this location without changing spin direction, they will start producing translational force in the opposite direction, and the whole group of cars would grind to a halt. Clearly this is an undesirable scenario that would produce no power; however, stopping and reversing the rotation of a several ton cylinder is no simple feat.

Due to the large friction losses in the rotation of the cylinders, Whitney et al. determined that regenerative breaking was not feasible as is shown in the figure below. They determined that only 20% of the spin-up power could be recovered by a regenerative breaking system, and that therefore the cost would be too great to justify. Part of the problem they no doubt encountered was the difficulty of finding high quality bearings of the correct size with extremely low friction. Large bearings on the order of 5 meters in diameter are not standard, so they may have to be fabricated specifically for the desired application.

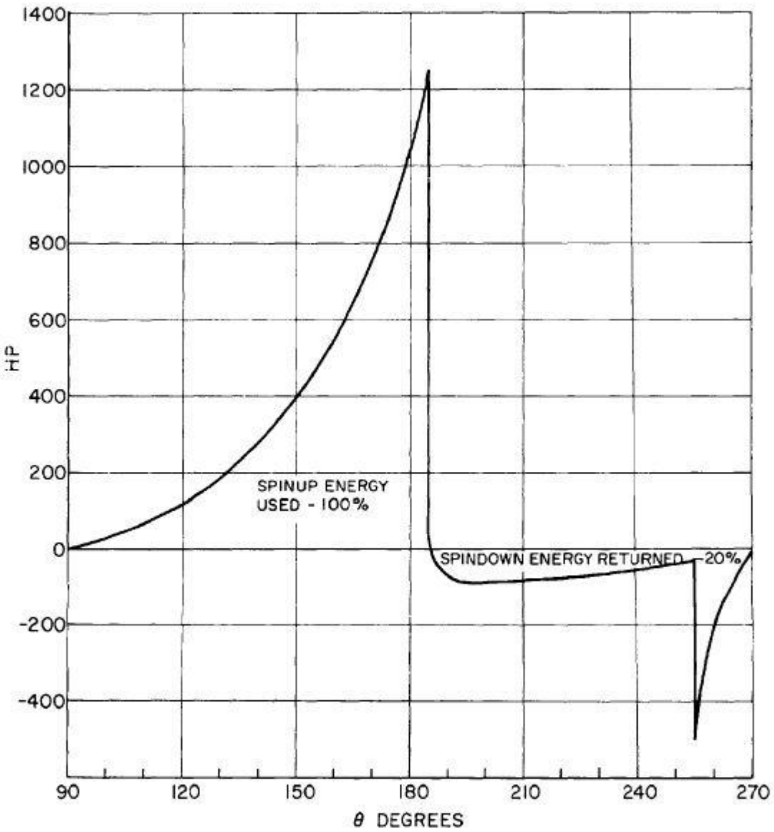

Figure 10: Regenerative braking energy return [Whitford et al., 1978]

This problem may in part be remedied by advances made in bearings since the study in 1978. It is possible that modern bearings have less friction and are comparably cheaper than those used in the previous study though since these are non-standard sizes it is hard to predict. In addition, regenerative braking has been researched and improved to a greater extent in the last few decades. The creation and increasing prevalence of hybrid vehicles shows that regenerative braking can be effective; however, a battery-based regeneration system will most likely be ineffective for a Madaras plant due to the fact that the rate of recharge for the batteries is limited by the rate of chemical reactions. A solution to this problem is to use a large flywheel which would preserve the kinetic energy easily. Though there would be frictional losses, the amount of energy the flywheel acquires would not be limited by the rate of acquisition. The regenerative energy could also be dumped to the power grid, though this may require additional power electronics that decrease the overall efficiency of the system. To date, no literature has studied this solution for a Madaras cylinder, though there are plenty of studies related to other machines.

Yet another solution to this problem proposed by B. Gibson et al. is to bypass the need to brake and then restart the rotation by instead flipping the cars at the midpoints of the track [Gibson et al., 2010]. This is demonstrated in figure 11 in which the cars are originally rotating with the green cylinder on top. As they reach the point where the wind is directed exactly along the line of travel, the cars flip so that the blue cylinder is now on top and they are rotating in the opposite direction with respect to the wind. This would be a great solution to the problem if not for a few large issues. Due to the weight of the cars, the amount of bracing that would be required to perform this operation may complicate things excessively or cost too much to be considered practical. Additionally, the track would need to be at least elevated to the height of a cylinder so that there is sufficient clearance between the top of the cylinder and the ground; however, a greater distance between the ground and the cylinder would be preferable so that there are only minor wind shear effects upon the cylinder caused by the proximity of the ground. Although the lower cylinder would be rotating the same direction as the upper cylinder and thus be producing power, the proximity of the boundary layer of the ground may result in much lower power production for the lower cylinder when compared to the upper cylinder. One last concern is that the switching section would have to be mobile with respect to the track. Otherwise, if the wind comes from an unexpected direction, the cars will be flipping at the wrong location, and by spinning the wrong direction they will reduce the total power produced by the Madaras power plant.

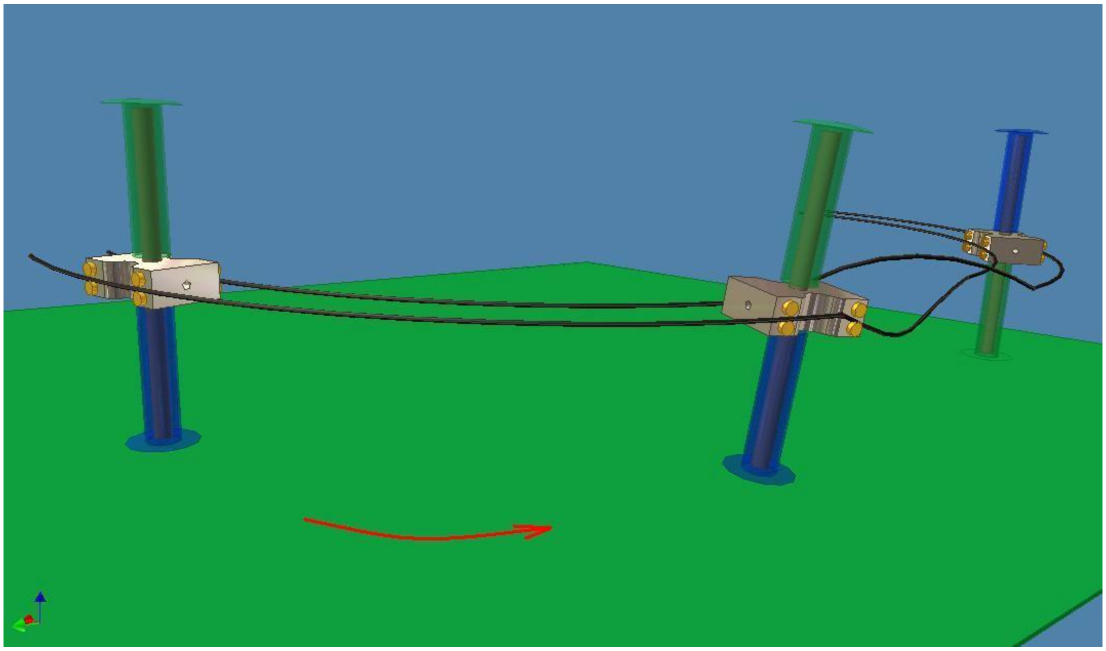

Figure 11: Flipping the cars as suggested by Gibson et al.

Turbine Interaction and Spacing

One other item that needs to be analyzed is the interaction and interference between cylinders. It is unlikely that flow field the downstream cylinders encounter v completely unaffected by the rotation and movement of the upstream cylinders. According to the Whitney et al., the interference can be determined by the equation below where f_n is the interference loss factor, P_n is the gross power generated by an N-car plant at wind speed V_w and track speed V_t, and P_l is the gross power generated by an l-car plant at the same wind speed and track speed as the N-car plant.

$$f_n = \frac{P_n/N}{p_l}$$

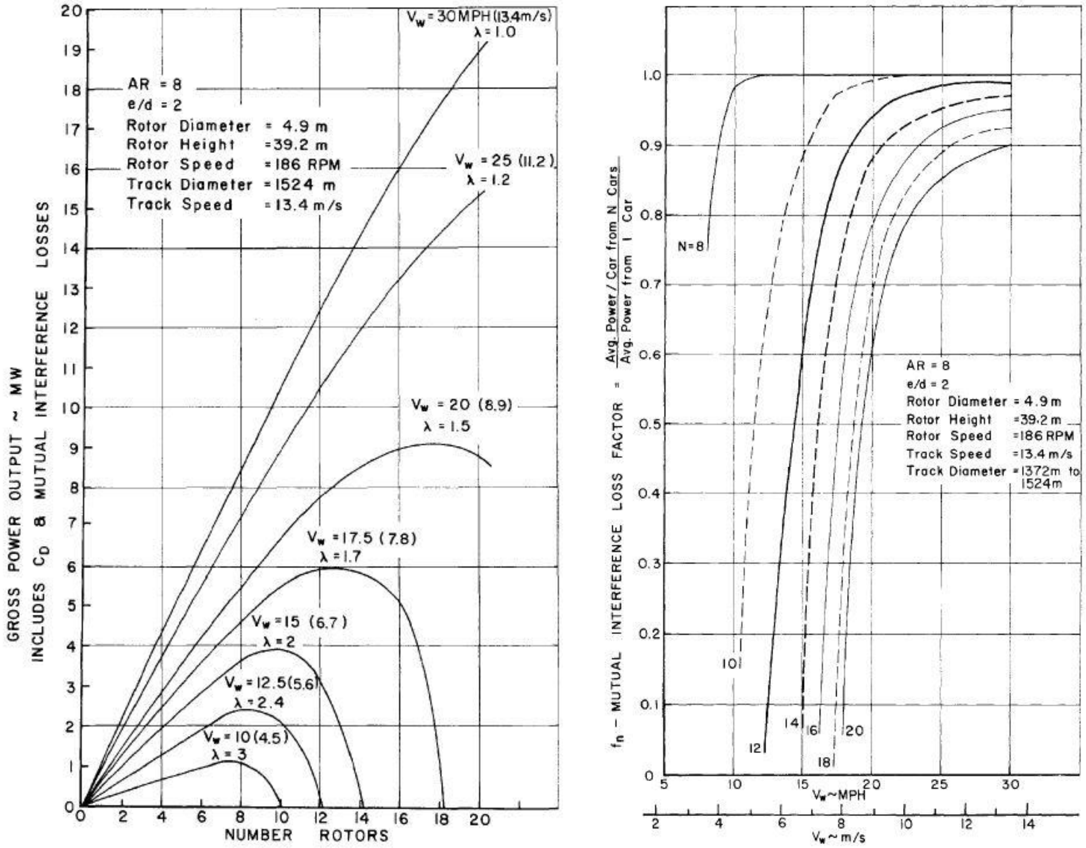

Figure 12: Interference from other cars [Whitford et al., 1978]

Location

The final major problem associated with creating a Madaras plant is finding a suitable location. All wind turbines suffer from a lack of good locations in which to place them. Like fossil fuel-burning plants, wind plants must be located where the power can be distributed easily to where it is needed; however, they must also have consistent and strong winds. Ideal locations may be populated, owned by others, or far from major cities. A Madaras plant suffers from all of these problems and the problem that the land must be relatively level. Since a Madaras plant is based upon the concept of cars moving along tracks, the land must either be very flat or made flat by human intervention. In this way, Madaras plants cannot be located in some prime spots such as mountain ridges. Luckily, many great locations such as open grassy plains have relatively flat land. In the wind map below showing the annual average wind power in the US as compiled by the National Renewable Energy Lab (NREL), the large expanses of plains spreading across the Midwest have moderate wind power production capabilities. Two areas that are both flat and have high average wind power are the Dakotas and the Pacific Northwest.

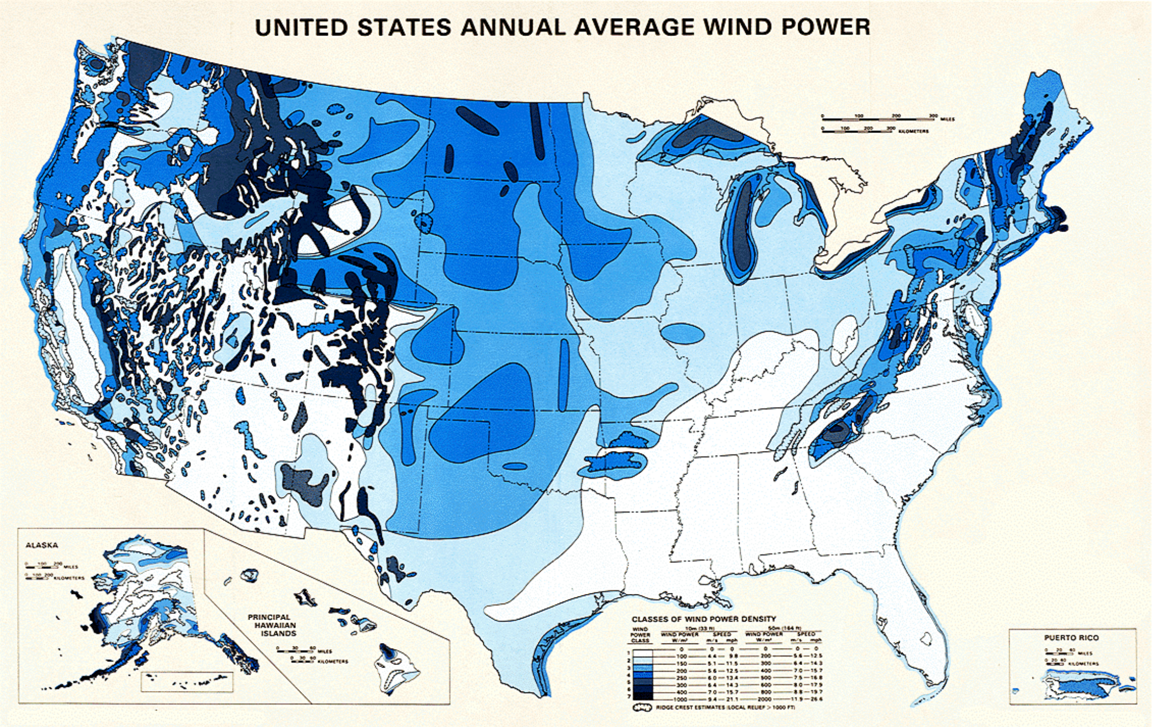

Figure 13: US Average Annual Wind Power [NREL]

Other Implementations of Rotating Cylinder Lift

Although only one full-size prototype of a Madaras cylinder was ever built, others have utilized the architecture for various purposes. In fact, Anton Flettner applied the Magnus effect as early as 1922 to design a sailing ship. Flettner's ship employed two rotating cylinders 15 meters tall and 3 meters in diameter, one mounted near the bow and the other near the stern of the refitted schooner as shown in the figure below. The rotors were powered by a 37 kW electric propulsion system. The ship was completed in October of 1924 and shortly thereafter set out on its maiden voyage. On its first voyage in February of 1925, the ship traveled from Danzig, Germany to Scotland across the North Sea. The rotors survived the stormy weather without problem. Possibly even more impressive is the fact that the ship could tack at an angle of 20-30 degrees whereas with the original sails it could only approach an angle of 45 degrees. Unfortunately, the rotors were less efficient than diesel engines in powering the vessel, and the ship was dismantled.

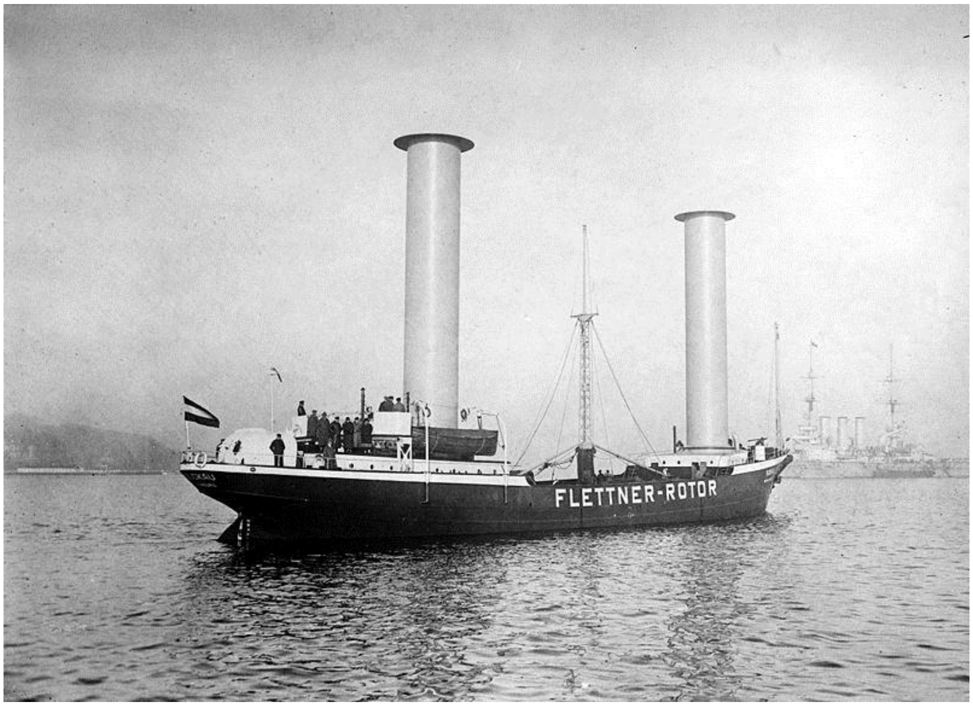

Figure 14: Flettner's ship [Ragheb, 2010]

Other copies of Flettner’s ship have shown up during the past few decades but the most widely-known and anticipated was the cargo ship E-Ship 1. In 2008, the ship was commissioned by Germany’s Enercon to transport wind turbine components. As can be seen in figure 15, four large Flettner rotors line the top of the ship. In total, the ship weighs 10,500 metric tons and is 130 meters in length. The ship is powered by two 3.5 MW diesel engines, and it can travel at a speed of up to 17.5 knots. The rotors on the ship are 27 meters tall and 4 meters in diameter. With the Flettner drive, experts have predicted fuel savings of 30-40%.

Figure 15: E-Ship 1 [Ragheb, 2010]

One other example of rotating cylinder lift that is not utilized for ship propulsion is the set of prototype wind turbines developed by Siyar Mehmetoglu. Below are two prototypes developed by him. As can be seen, the turbines function because of the Magnus effect; however, the turbines do not stand alone but are mounted on the top of a supporting structure like a horizontal axis wind turbine. These turbines are essentially a hybrid design between vertical axis wind turbines and Madaras turbines. Unfortunately, no studies have been performed to date that analyze the performance of these hybrid turbines.

Figure 16: NSM 21 Prototype 1 [Mehmetoglu, 2008]

Figure 17: NSM 21 Prototype 2 [Mehmetoglu, 2008]

CHAPTER II

MODELING AND SIMULATION

Modeling Process Overview

All modeling was performed using COMSOL 4.2 with the CFD module. Although this build of the CFD module came with Rotating Machinery physics, due to the simple nature of the walls use of this was not necessary; instead, walls were modeled as moving with velocities in the x- and y-directions. Using the Madaras parameters for the cylinders results in turbulent air as defined by its Reynolds number interfacing with the cylinder.

2D Validation

Before any 3D models were built and solved, a model using 2D geometry was created. This model was made for comparison against the one given by Ingham and Tang in their paper “A numerical investigation into the steady flow past a rotating circular cylinder at low and intermediate Reynolds numbers” [Ingham et al., 1990]. In their study, they used a Reynolds number of 20 but did not disclose any further parameters. Thus, the density and dynamic viscosity of air at 20 degrees Celsius (1.2047 kg/m^3 and $1.8205*10^{-5}$ kg/m-s, respectively) along with a diameter of 1 cm and a free stream flow velocity of 3.02 cm/s (0.0302 m/s) were used. In this case, the flow velocity was the result of plugging the rest of the parameters into the equation for the Reynolds number and solving for its value at a Reynolds number of 20.

The rotational velocity of the cylinder was the parameter that Ingham and Tang varied in their study. They computed α, which is the ratio between the rotational velocity and the translational velocity, as $\alpha = a\omega_0/U$ where a is the radius, ω_0 is the rotational velocity in radians per second, and U is the free stream velocity in m/s. This ratio was computed for values of 0, 0.1, 0.5, 1, 2, and 3. Rearranging and solving for the quantity $a\omega_0$ gave 0, 0.00302, 0.0151, 0.0302, 0.0604, and 0.0906 for the corresponding α values to be used in this study.

After determining what to analyze, the COMSOL model was created. The geometry consisted of a circle of diameter 0.005 m enclosed by a rectangle of 0.25 m by 0.125 m. Although this is much smaller than the diameter of a Madaras turbine, it was used only to compare the accuracy of the COMSOL model to the CFD model created by Ingham and Tang. The rectangular boundary of 0.25 m by 0.125 m was deemed sufficient to ensure that there were no noticeable boundary effects upon the fluid near the cylinder. The model was solved using the Turbulent Flow, k-ε physics with incompressible flow, the RANS model type, and the low Reynolds number turbulence model. Although the flow is nearly laminar at this Reynolds number, a model that could be used for the higher Reynolds number Madaras cylinder studies was desired, so a turbulent flow model was used. All other COMSOL parameters were set to their default values as determined by COMSOL.

The inlet of the fluid flow located on the negative-x vertical boundary had a uniform velocity of 0.0302 m/s, a turbulent intensity of 0.05, and a turbulence length scale of 0.1 m. The outlet was defined on the positive-x vertical boundary as a location with no pressure difference between the domain and the outside; it also had no viscous stress. The rotating wall was defined so that the velocity was a function of position. By parameterizing the x- and y-velocity equations, a counterclockwise rotating wall could be modeled as given in the equation below.

$$U_w = \begin{cases} -\alpha U \sin\big(atan2(y,x)\big), & U_{w,x} \\ \alpha U \cos\big(atan2(y,x)\big), & U_{w,y} \end{cases}$$

The mesh was created using the default parameters given by COMSOL with the exception of the size and type. The mesh is a free triangular configuration with an extra fine element size (as determined by COMSOL). An image of the mesh is shown below in figure 18. A close-up view of the mesh near the cylinder is shown in figure 19. As can be seen, the mesh is fairly fine throughout the domain. It was easily fine enough to capture the effects away from the cylinder, but since the 2D geometry was not too computationally demanding, no effort was required to make a fine mesh near the cylinder and a coarse mesh far from it. Also, the mesh captured all the flow effects near the cylinder, so creating a finer mesh would have been a waste of time.

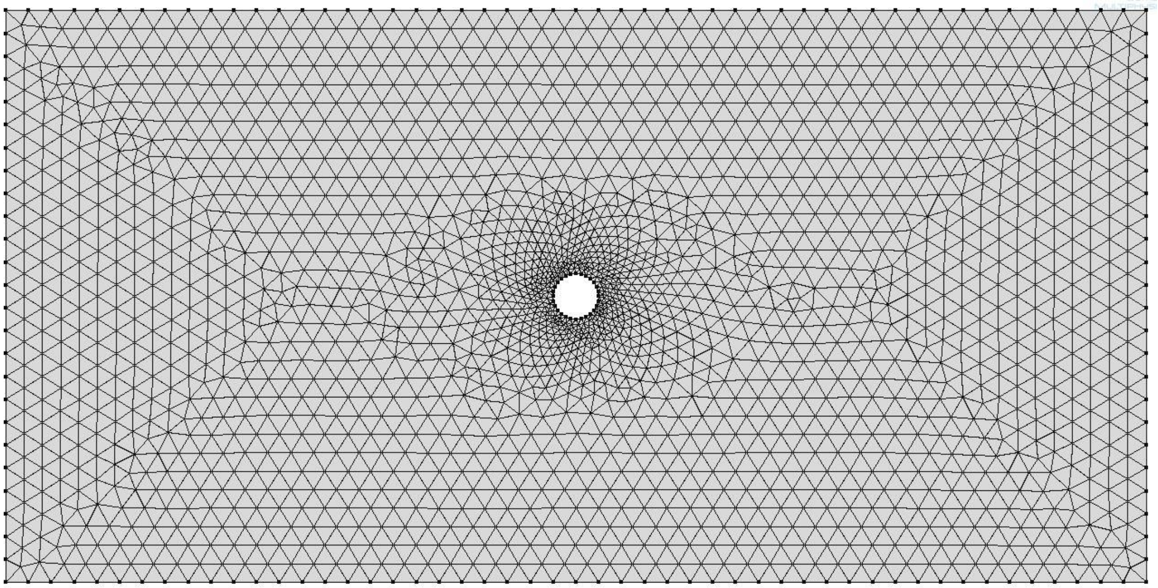

Figure 18: 2D mesh in COMSOL

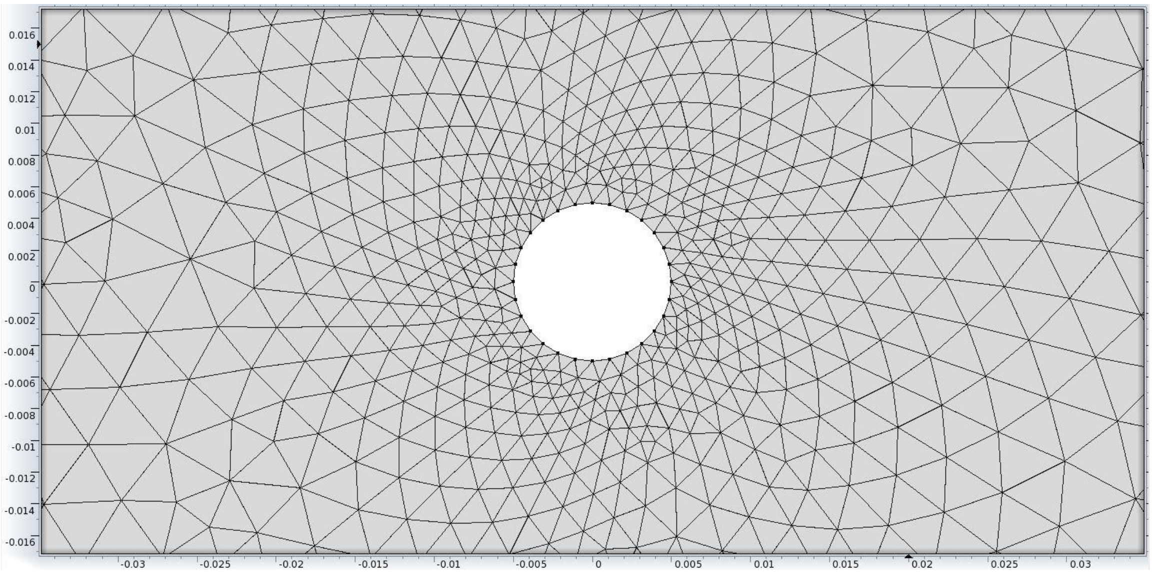

Figure 19: 2D mesh close-up

After building the mesh, the model was solved for steady flow using all the default parameters set by COMSOL. The following images were produced for the six different α values in order from top to bottom. It is clear that the results obtained in this study very nearly match the results obtained by Ingham and Tang. Thus, the computational fluid dynamics model created in COMSOL was deemed valid for 2D flow.

α = 0

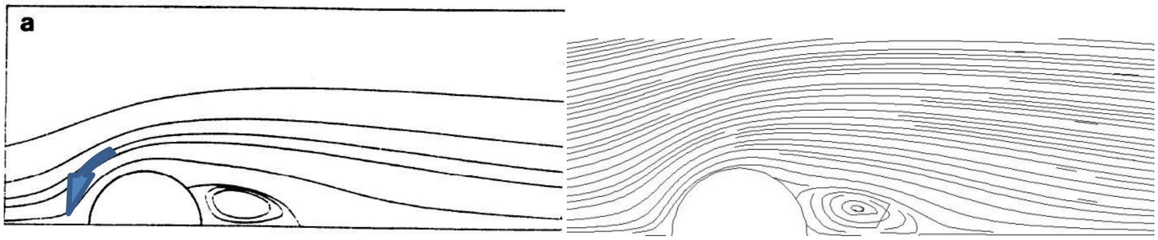

α = 0.1

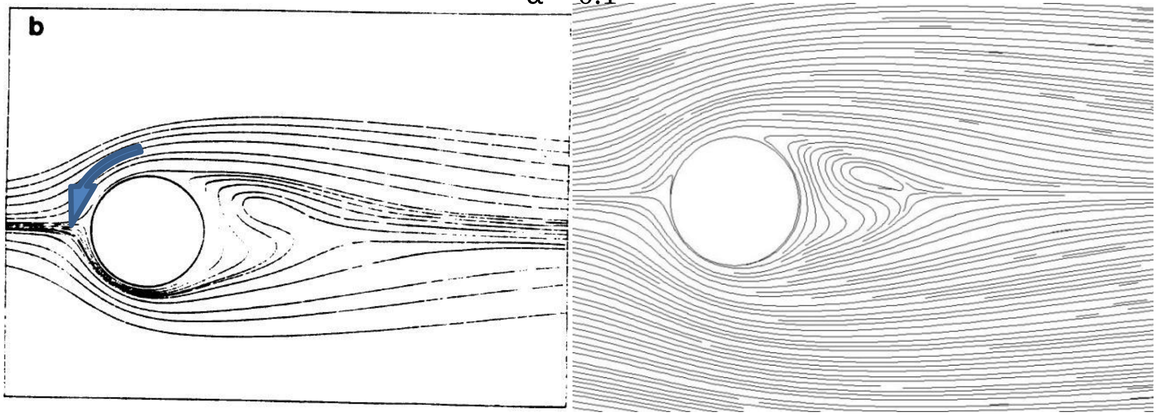

α = 0.5

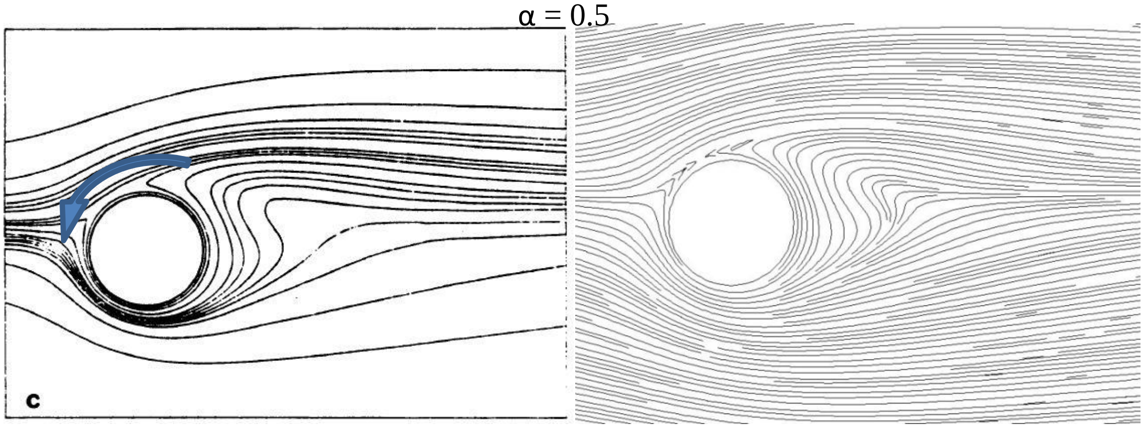

α = 1

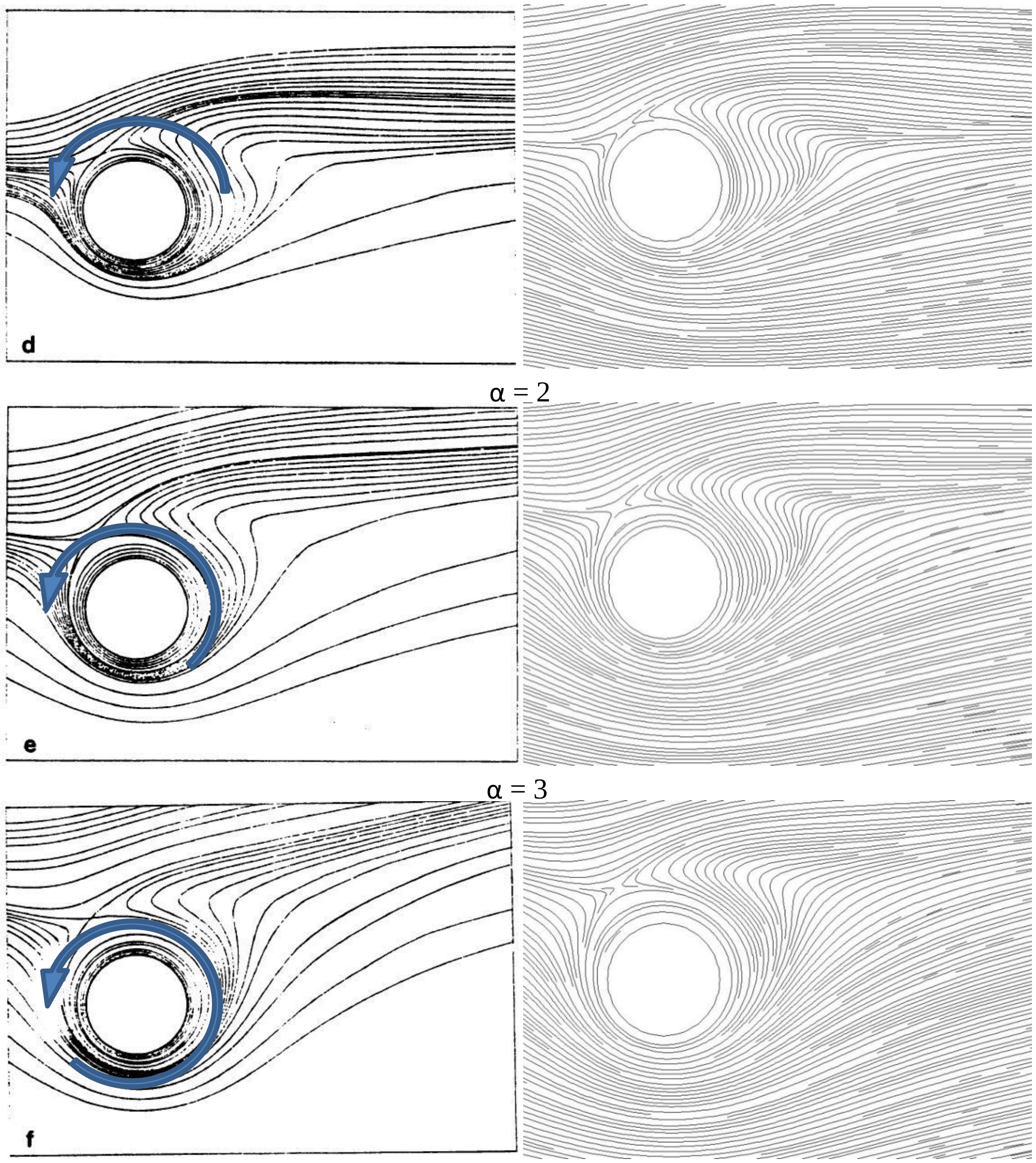

Figure 20, a-f: 2D comparisons with Ingham and Tang streamlines [1990]

To ensure accuracy of the studies, an additional set of tests was run. Hoerner et al. in the book *Aerodynamic and Hydrodynamic Lift* presented a series of tests for rotating cylinders and determined the coefficients of lift and the coefficients of drag for various conditions. These results are shown in figure 21 [Hoerner, 1985]. As can be seen in the figure, the values for the coefficient of lift increase nearly linearly until approximately a value for *U/V* (which is the same as ω_0/U used previously) of 3. At this point, both the coefficient of lift and the coefficient of drag start increasing at slower rates. Also interesting to note is that for a *U/V* value between 0 and 0.5, the cylinder produces negative lift. This seems counterintuitive, but Hoerner explains that it appears to be caused by a bubble on the lower surface that reattaches, creating negative lift.

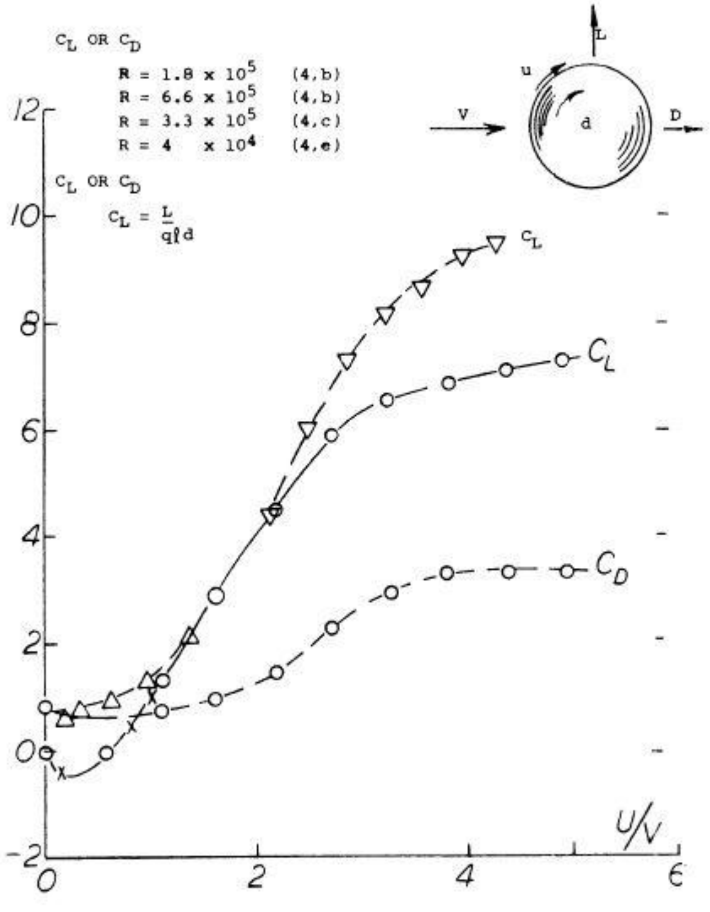

Figure 21: Rotating cylinder coefficient of lift [Hoerner, 1985]

Tables in appendix A contain the data from the tests performed for the 2D analysis of a rotating cylinder. All of these tests were performed for a 1-meter diameter cylinder in air at 20 degrees Celsius (density = 1.2047 kg/m^3, dynamic viscosity = 1.82*10^5 kg/m*s). It should be noted here that a 1-meter diameter cylinder was used since the diameter does not affect the performance of the cylinder and a unity diameter cylinder would be easier to compare with the 3D cylinders since one would only need to multiply by the aspect ratio of the 3D cylinder to compare them. The inlet velocity was varied to get data for Reynolds numbers in the range from 4.14*10^4 to 4.30*10^6. All tests were performed for relative speeds (defined as $\omega D/2v$) from 1 to 5. The rotational speed required for model input was determined by solving the relative speed equation for ω. It was determined that the turbulent flow, low RE k-ε COMSOL model was the most accurate for the parameters specified. For the inlet, a turbulent intensity of 0.01 (or 1%) and a turbulence length scale of 0.01 m were chosen as adhering to results from current research of low turbulence steady wind and from the documentation for turbulence modeling in Fluent [Drakos]. The domain for the 1m-diameter cylinder was a rectangle 5 meters wide and 10 meters in length. It should be noted that larger domains were also tried, but they did not significantly impact the results, so the smaller more computationally efficient domain was used. To ensure accuracy near the rotating cylinder, COMSOL's built-in extra fine mesh was used with 8 boundary layers with a stretching factor of 8 around the cylinder.

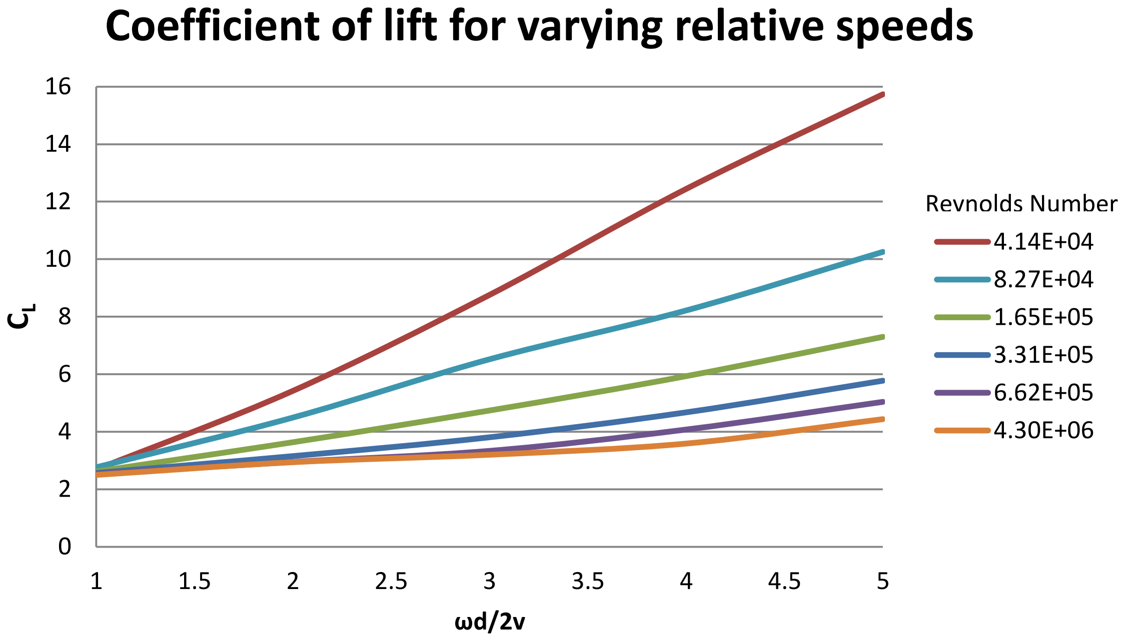

Figure 22: C_L versus ωD/2v for varying Reynolds numbers

The figure above shows the results, which were calculated as follows. The pressures P1 and P2 are opposing pressures that split the cylinder in two. If a line were drawn splitting the cylinder along the streamwise direction, these two pressures would be the result: P1 is the pressure along the lower surface semicircle (negative y), and P2 is the pressure along the upper surface semicircle (positive y). These pressures were determined in COMSOL by taking the line integral along the surface of half of the cylinder of $-y/sqrt(x^2+y^2)*p$ where p is the point's pressure and x and y are its coordinates. DelP is the difference between P1 and P2. The coefficient of lift C_L was calculated as $delP/(\rho * v^2 * D/2)$ where ρ is the density, v is the velocity of the freestream flow, and D is the cylinder diameter. The figure below is a comparison of the Hoerner curve on the right with the data from the study with the axes scaled equivalently. To facilitate comparison the Reynolds numbers were removed from the graph of the study's data.

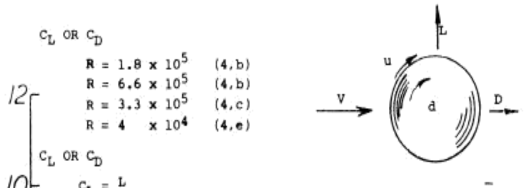

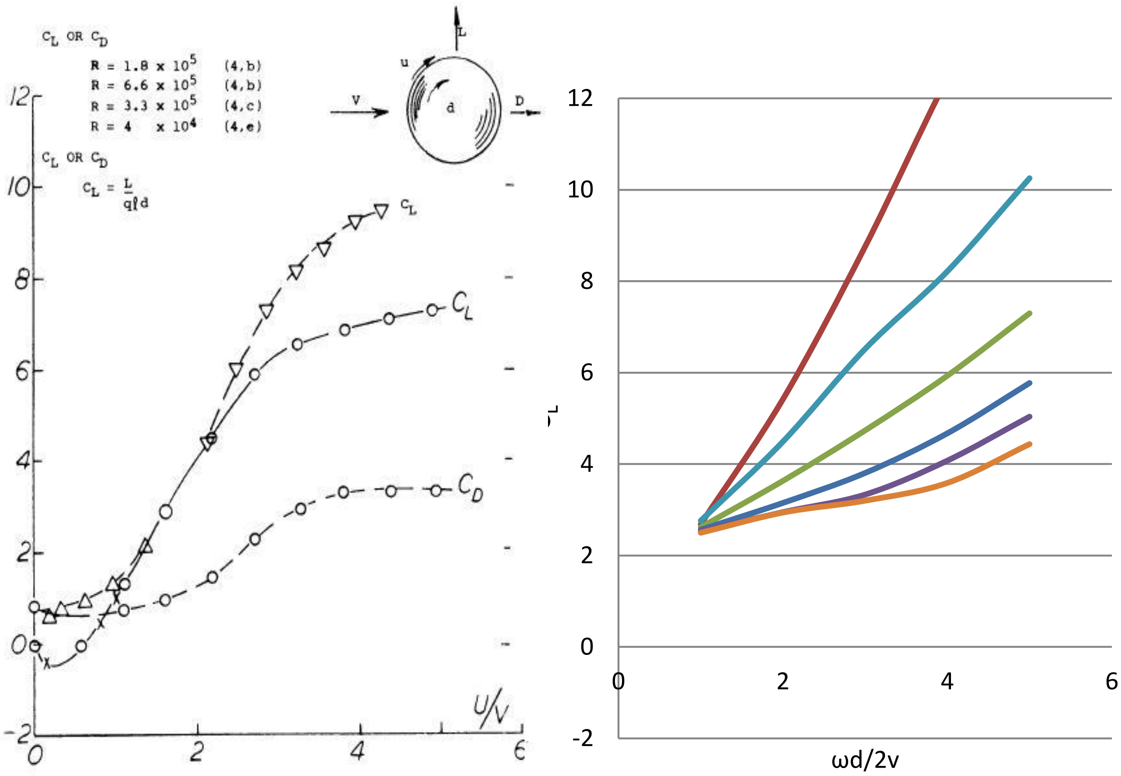

Figure 23: Comparison of Hoerner Cl with study Cl

As can be seen, the results from the CFD modeling did not follow Hoerner's curves as accurately as desired. The general upward trend was the same as in Hoerner's curves, but the magnitude varied much more depending upon the Reynolds number. For a Reynolds number of $4.14*10^4$, the coefficient of lift at a relative speed ratio of 5 was nearly 16, whereas for a Reynolds number of $6.62*10^5$ at the same relative speed ratio, the coefficient of lift was only 5. In addition, within the relative speed ratio range, no nonlinearity occurred unlike in Hoerner's results. Instead, the coefficients of lift increased nearly-linearly with the relative speed ratio. Though much thought was given as to why this occurred, no clear solution was arrived at. Most likely, the differences in these results stem from parameters used in Hoerner's experiment that were different than those used in this one. These may include the inlet conditions, the surface treatment of the cylinder, the boundary size, the fluid properties (temperature, relative humidity), and others. Unfortunately, in Hoerner’s book there is no elaboration on the way the experiment was conducted, and he passed away several years ago, so it is unlikely that what he did will ever be determined. It is clear that his results are based upon experimental data, not CFD, and this may also affect the data depending upon how well-designed the wind tunnel was.

Another likely explanation for the discrepancy between the study performed here and that done by Hoerner is the inability to solve turbulence problems accurately using computational models. According to Ferziger et al (2002), “predictions obtained when turbulence models are used are not accurate enough that they can be accepted without testing.” They continue on to note that the design that performed the best in the computational studies will perform the best in tests. For this reason, many groups will perform CFD analyses of turbulent flows to determine the best solution to a problem and then physical model it to obtain useful and accurate data. Thus, it is possible that even though the results obtained above did not follow Hoerner’s results extremely accurately, they are the best that can be produced computationally. Importantly, they show the correct general trends, and these are the most important.

Before moving on to the analysis of the Madaras model, one last study was performed to validate the two-dimensional Madaras model: a comparison to the 1 meter diameter model for similar Reynolds numbers. Though coefficient of lift values were expected to be near those for different diameters but the same Reynolds numbers, this was validated and data is shown in the appendix for diameters of 0.5, 1, and 2 meters. As shown below, the coefficients of lift were almost identical for the 2.5-meter diameter Madaras cylinder and the 1-meter diameter test cylinder. The small difference may be caused by the fact that the Madaras Reynolds number is actually $4.43*10^6$.

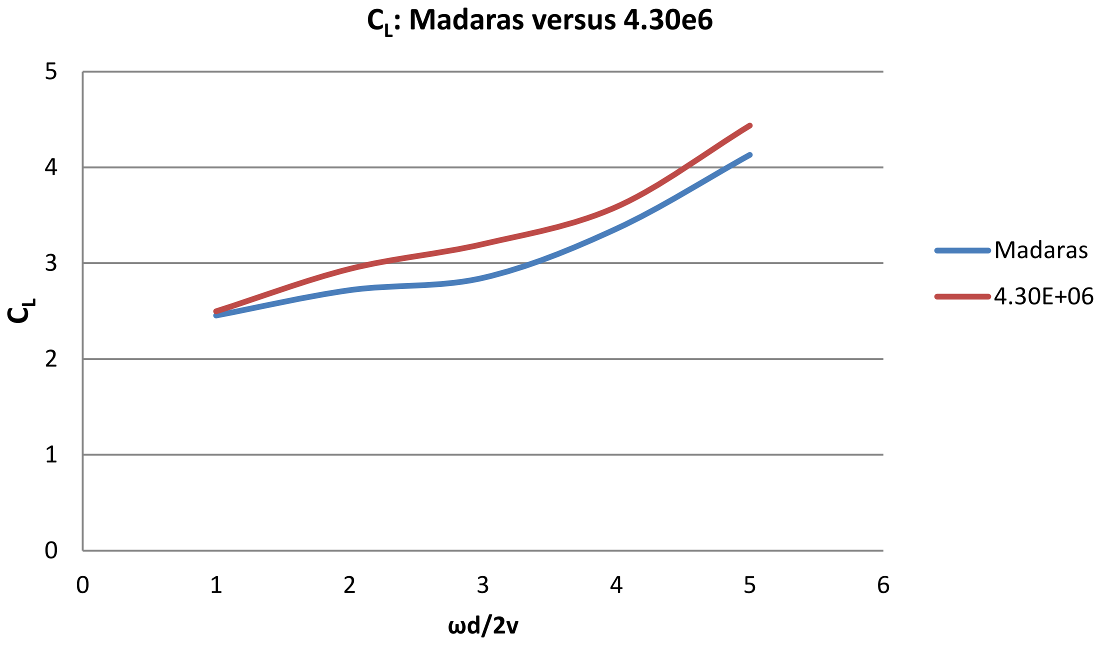

Figure 24: CL for Madaras and RE 4.30e6

After seeing coefficients of lift higher than 10, a C_L of 3 seems quite low. However, this must be placed in context with the lift coefficients of traditional wind turbines. Since standard vertical axis wind turbines blades are essentially rotating airfoils, they cannot achieve coefficients of lift remotely close to that achieved by a rotating cylinder. In the table below, some of the better airfoils that were designed by the National Renewable Energy Laboratory are listed along with their coefficients of lift [Buhl, 2009]. The maximum coefficient of lift found in the whole table is that of 1.68 for airfoil S818. Most of the coefficients of lift are somewhere between 1 and 1.5 – much lower than that for a rotating cylinder.

Table 3: Selected NREL S-Series Airfoils [Buhl, 2009]

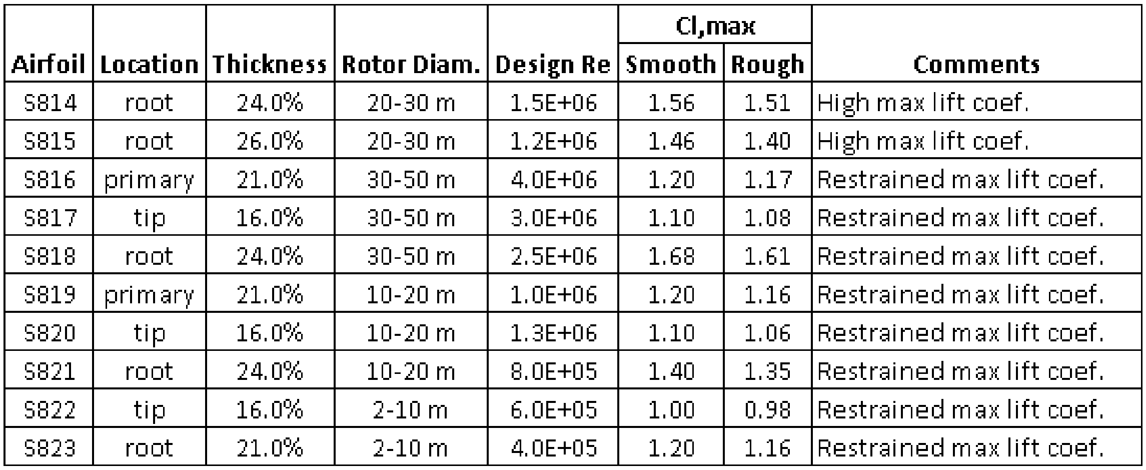

Airfoil	Location	Thickness	Rotor Diam.	Design Re	Cl,max Smooth	Cl,max Rough	Comments
S814	root	24.0%	20-30 m	1.5E+06	1.56	1.51	High max lift coef.
S815	root	26.0%	20-30 m	1.2E+06	1.46	1.40	High max lift coef.
S816	primary	21.0%	30-50 m	4.0E+06	1.20	1.17	Restrained max lift coef.
S817	tip	16.0%	30-50 m	3.0E+06	1.10	1.08	Restrained max lift coef.
S818	root	24.0%	30-50 m	2.5E+06	1.68	1.61	Restrained max lift coef.
S819	primary	21.0%	10-20 m	1.0E+06	1.20	1.16	Restrained max lift coef.
S820	tip	16.0%	10-20 m	1.3E+06	1.10	1.06	Restrained max lift coef.
S821	root	24.0%	10-20 m	8.0E+05	1.40	1.35	Restrained max lift coef.
S822	tip	16.0%	2-10 m	6.0E+05	1.00	0.98	Restrained max lift coef.
S823	root	21.0%	2-10 m	4.0E+05	1.20	1.16	Restrained max lift coef.

2D Madaras Analysis

After the validation of the 2D model, a model using the Madaras parameters listed in the introduction was created. Using the 2D geometry, data for an infinitely long rotating cylinder could be computed. The temperature of the air was chosen to be 20 degrees Celsius, which corresponded to a density of 1.2047 kg/m^3 and a dynamic viscosity of 1.8205*10^{-5} kg/m*s. The cylinder had a diameter of 5.0 m. It should be noted that this is not exactly the 4.9 meters used for the Madaras cylinder but has a slightly larger diameter to make the numbers cleaner and therefore easier to understand quickly. The uniform velocity entering the domain from the inlet was 13.4 m/s with a turbulence intensity of 0.01 and a turbulence length scale of 0.01 m. The rotational speed was 186 rpm ($\alpha U = a\omega_0 = 47.7$ m/s). Given the above, the Reynolds number as calculated by $Re = \rho V d/\mu$ is 4.35*10^6. The domain was 50 meters long and 25 meters wide. All the other parameters not previously mentioned were configured exactly the same as in the 2D validation models, and the mesh appeared extremely similar.

The first variable analyzed was the velocity profile, which can be seen below in figures 25 and 26. Figure 25 shows the streamlines for the steady-state analysis, which are extremely similar to those in the 2D validation models. Figure 26 just below it shows the velocity magnitude in which dark blue corresponds to a velocity of 0.17 m/s and dark red corresponds to a velocity of 50.9 m/s. Though it is difficult to see, the highest velocity occurs at the boundary layer of the counter-clockwise rotating cylinder as should be expected. On the top half of the cylinder there is fairly low velocity, and on the bottom half there is fairly high velocity. In addition, a region of high velocity extends pretty far out in the negative-y direction (to the boundary of the domain in this study). Thus, a second study was performed with a domain 70 meters wide and 140 meters in length. When the boundary was expanded, there was no change in the velocity profile, so the smaller domain is considered an accurate result.

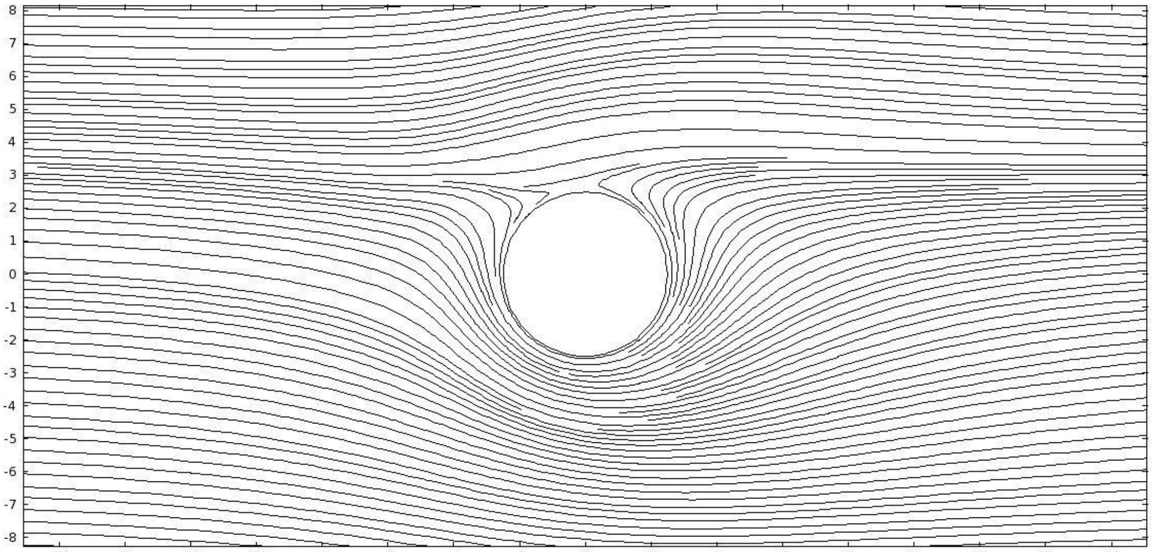

Figure 25: 2D Madaras streamlines

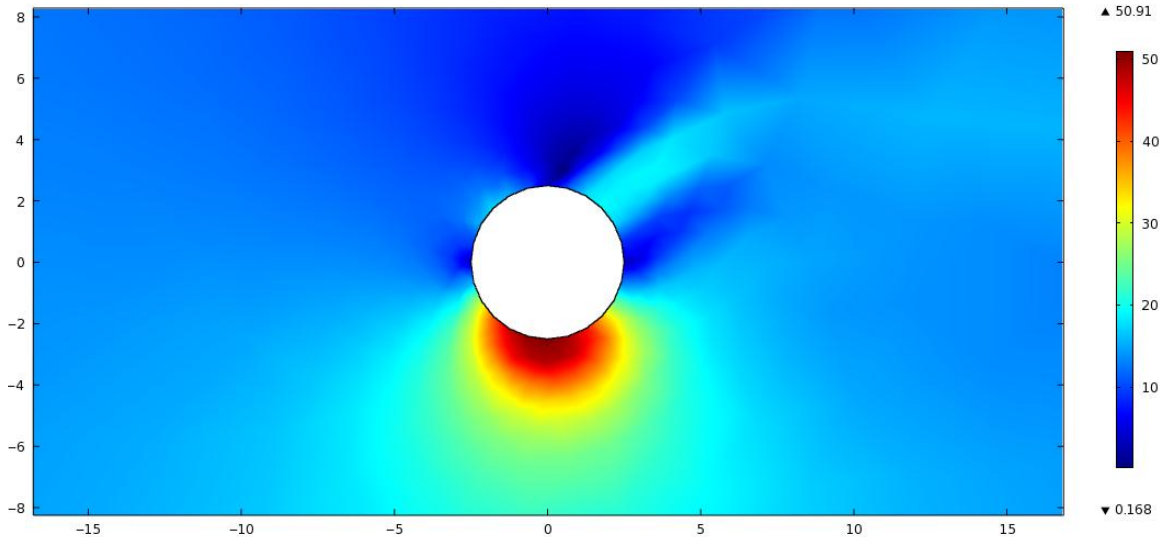

Figure 26: 2D Madaras velocity magnitude

The most important part of this analysis is the pressure contour because the pressure determines how much lateral force a Madaras cylinder can generate (and thus how much energy). Below in figure 27 is a pressure contour with values ranging from -2515 Pa to 24 Pa. It looks extremely similar to the velocity magnitude profile as expected.

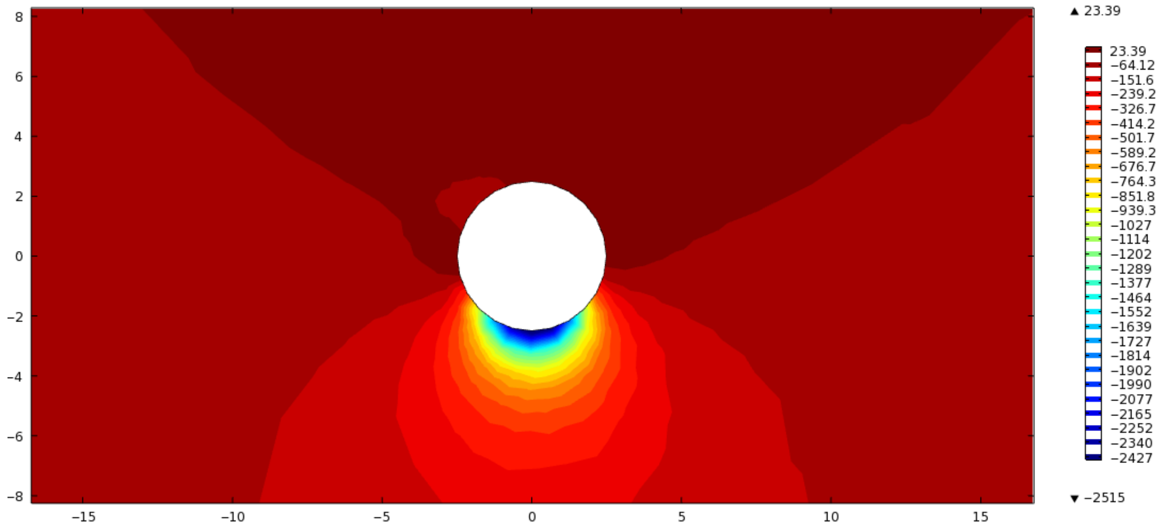

Figure 27: 2D Madaras pressure contour

Below in figure 28 is a close-up image of the pressure for the rotating cylinder. A black dotted line has been added bisecting the y-direction to show more easily the pressure between the two halves of the cylinder that create the lateral force. It can be seen in the image that the top half has a higher total pressure than the bottom half. This will create a force in the negative y-direction, which will allow power to be generated as the cylinder translates in the spanwise direction.

One other item of interest in the image below is the difference in pressure between the negative-x side (front) of the cylinder and the positive-x side (back) of the cylinder. This pressure difference is typically known as the drag force that a blunt object experiences. However, since the cylinder is translating in the negative-y direction, the term “drag” doesn’t apply in the traditional sense. Instead, this pressure difference will create a tipping moment about the base of the car which must be counteracted by design of the interface between the wheels and the track, a greater car weight, a slightly more innovative method such as a mass that travels along a track perpendicular both to the direction of travel and the axis of cylinder rotation, or a combination of these. If a weight were to be used to counteract the tipping moment, it could be actively controlled so that the car only experienced the forward force caused by the Magnus effect and the downward weight force of the vehicle.

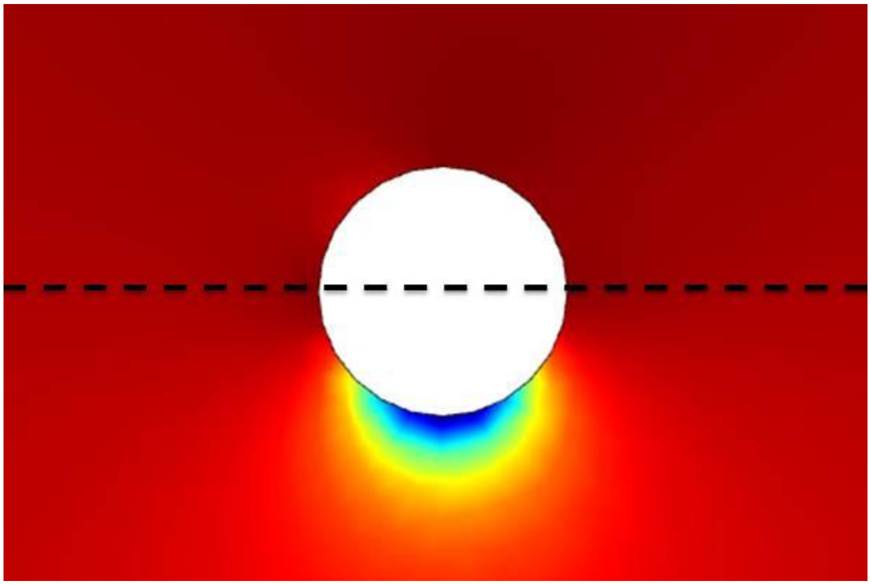

Figure 28: 2D Madaras pressure hemispheres

3D Validation

The 3D analysis was validated under the assumption that the total force that acts upon a 3D cylinder is roughly the same as the force that acts upon a 2D cylinder of equivalent length. To evaluate this, two surface integrals were used on the lateral sides of the 3D cylinder and then their difference was computed. It was expected that the total force that acts upon a 3D cylinder would be marginally less than the total force that acts upon a 2D cylinder multiplied by the length of the 3D cylinder because of two effects: 1) interaction with the "ground" at the base of the 3-dimensional boundary and 2) interaction between the top of the cylinder and the surrounding fluid. The 2D cylinder did not suffer from these two inefficiencies, so the pressure difference between the two lateral sides should be greater than it is in the 3D case. (Note that this is similar to the fact that a 2D airfoil will produce greater lift than a 3D airfoil due to the boundary effects.)

3D Testing

Testing of the Madaras cylinders using the COMSOL software required the variation of two primary parameters: aspect ratio (AR) and the ratio of cap diameter to cylinder diameter (e/d). As in the two-dimensional case, a base cylinder diameter of 5 meters was used as opposed to the Madaras cylinder, which has a diameter of 4.9 meters. It was assumed that this difference of a 2% increase in cylinder diameter would not significantly impact the results. For the tests, the aspect ratio was varied between 4 and 10 while the cap diameter to cylinder diameter ratio was varied from 1 to 3. To determine the cap height (CH), the aspect ratio was multiplied by the cylinder diameter of 5 meters. For all the tests, the boundary depth (the dimension of the spanwise direction) was set at 60 meters and the boundary width (the dimension of the streamwise direction) was set at 80 meters. In addition, a rotational speed of 186 rpm and a fine tetrahedral mesh were used.

Table 4: CFD test matrix

Test #	AR	e/d	Cap Diameter (m)	Cap Radius (m)	CH (m)	BH (m)
1010	10	1	5	2.5	50	70
1015		1.5	7.5	3.75		
1020		2	10	5		
1030		3	15	7.5		
810	8	1	5	2.5	40	60
815		1.5	7.5	3.75		
820		2	10	5		
830		3	15	7.5		
610	6	1	5	2.5	30	50
615		1.5	7.5	3.75		
620		2	10	5		
630		3	15	7.5		
410	4	1	5	2.5	20	40
415		1.5	7.5	3.75		
420		2	10	5		
430		3	15	7.5		

For all tests: cylinder diameter = 5m, boundary depth = 60m, boundary width = 80m, fine tetrahedral mesh

The boundary height (BH) was one part of the setup that required further analysis. The initial boundary height was set at 10 meters greater than the cylinder height (i.e. 30m for the 20m cylinder and 50m for the 40m cylinder). Unfortunately, many of the runs failed to converge, and so this condition needed to be modified. The table below shows several runs with different boundary heights for various cylinder heights. The column “Success?” was marked with a “Y” for a simulation that did converge or an “N” for a simulation that did not converge. In addition, many of the simulations that did not converge showed up with an error that read “Ill-conditioned preconditioner,” which simply stated that there was an error with the simulation setup. The only two cylinder height and boundary height setups that did not suffer from this error were 25m / 50m and 40m / 60m. Other solutions were tried for eliminating this problem including increasing the boundary size or increasing the fineness of the mesh, but neither of these provided a solution. Based upon the trial runs, boundary heights were chosen so that the boundary height was simply 20 meters greater than the cylinder height.

Table 5: Boundary height determination

CH	BH	Success?	Additional Comments
40	50	Y	
20	30	N	
20	50	N	
30	40	N	
30	50	Y	
25	50	Y	No Ill-conditioned preconditioner!
40	60	Y	No Ill-conditioned preconditioner!
20	40	Y	
20	35	Y	
20	35	Y	Boundary size 100x80x35
20	35	Y	Fine mesh
40	80	Y	
50	75	Y	
50	70	Y	
50	65	Y	

The results from the 3D studies were very illuminating though some of the results were exactly as expected. Below is a figure showing slices of the velocity magnitude at various locations along the cylinder’s length. Not surprisingly, the velocity profile around the cylinder is extremely similar for all points along the main shaft of the cylinder. This compares very well with the 2D study.

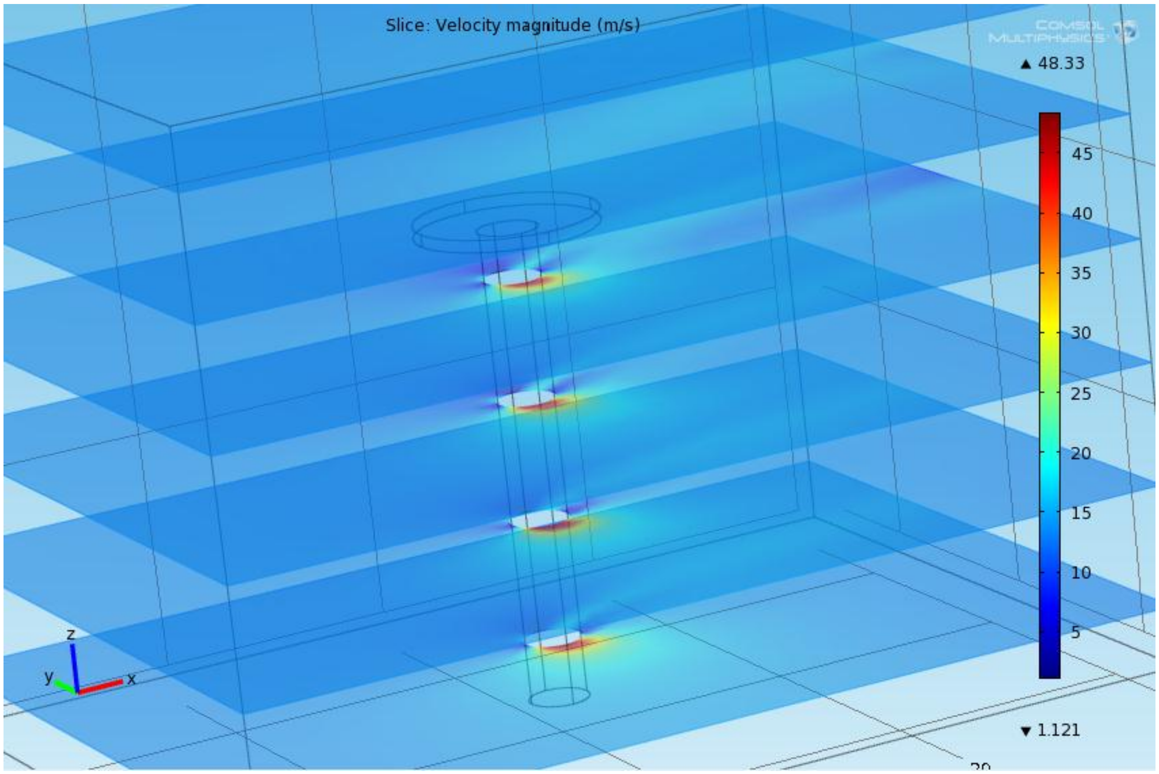

Figure 29: Velocity profiles along the cylinder's body, AR=8, e/d=3

One major difference between the 2D simulations and the 3D simulations is the addition of the cap on top. The cap is added for the same reason that winglets are added to airplanes. All airplanes experience wingtip vortices, which are created because the high pressure region under a wing curls up onto the low pressure region on the upper part of a wing. To remedy this problem, little fins called "winglets" are added to the wing, and this greatly reduces the vortex strength as illustrated in the figure below. Like a winglet, the cylinder cap prevents some of the pressurized air created by the rotation of the cylinder from escaping around the top of the cylinder. In this way, a drastic reduction in the Madaras cylinder's lift near the cylinder top is avoided.

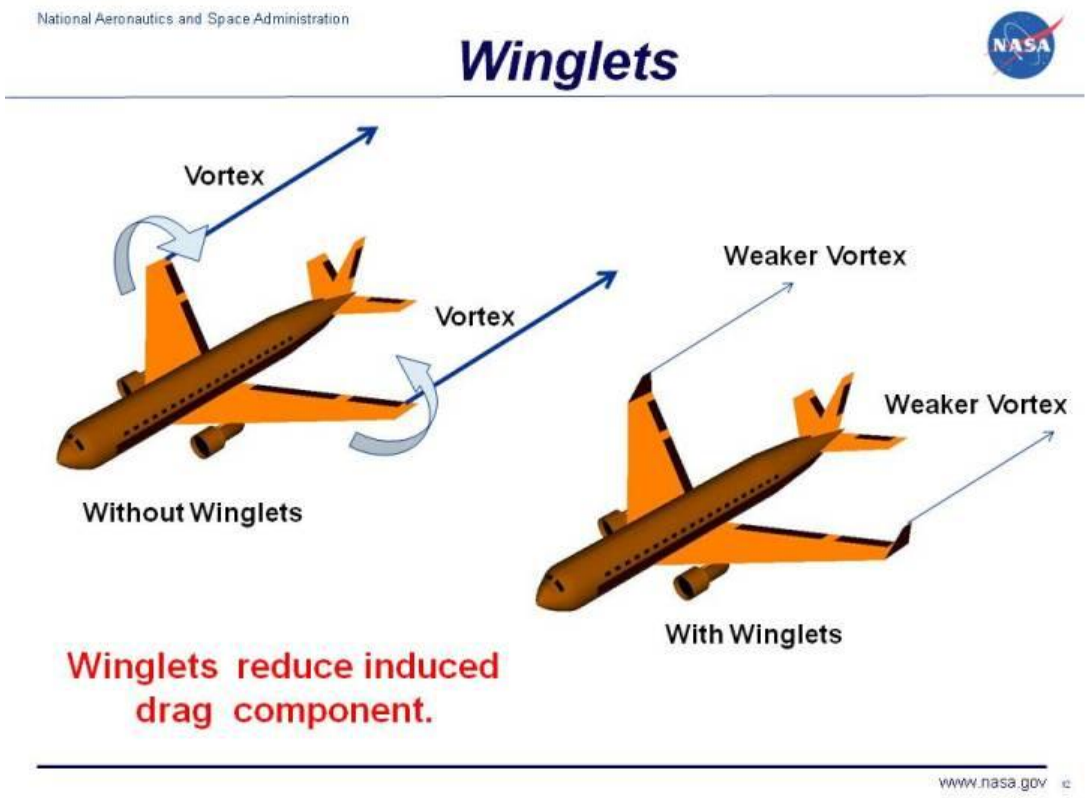

Figure 30: Winglet function for comparison to cylinder cap [NASA, 2010]

The effect of the cylinder cap on the airflow is visualized in the figures below. The first one is a frontal view looking from the direction of the incoming flow, and the second one is a side view in which the fluid is flowing from left to right. As can be seen, as the air passes the cylinder, some of it is deflected upward and some of it is deflected downward. The coloring on the cylinder denotes the pressure in Pascals: the large section of blue on the cylinder’s face is a section of low pressure and high velocity. As the incoming flow is spun around the cylinder, it encounters the wall of high pressure on the other side of the cylinder and is diverted upward. Simultaneously, the flow above the cylinder moves downward after passing the cylinder to fill this low pressure region. This is exactly the type of inefficient behavior that is decreased (though clearly not eliminated) by the cap.

Although this behavior still occurs, a cap on the end of the cylinder greatly reduces its effect as will be shown shortly.

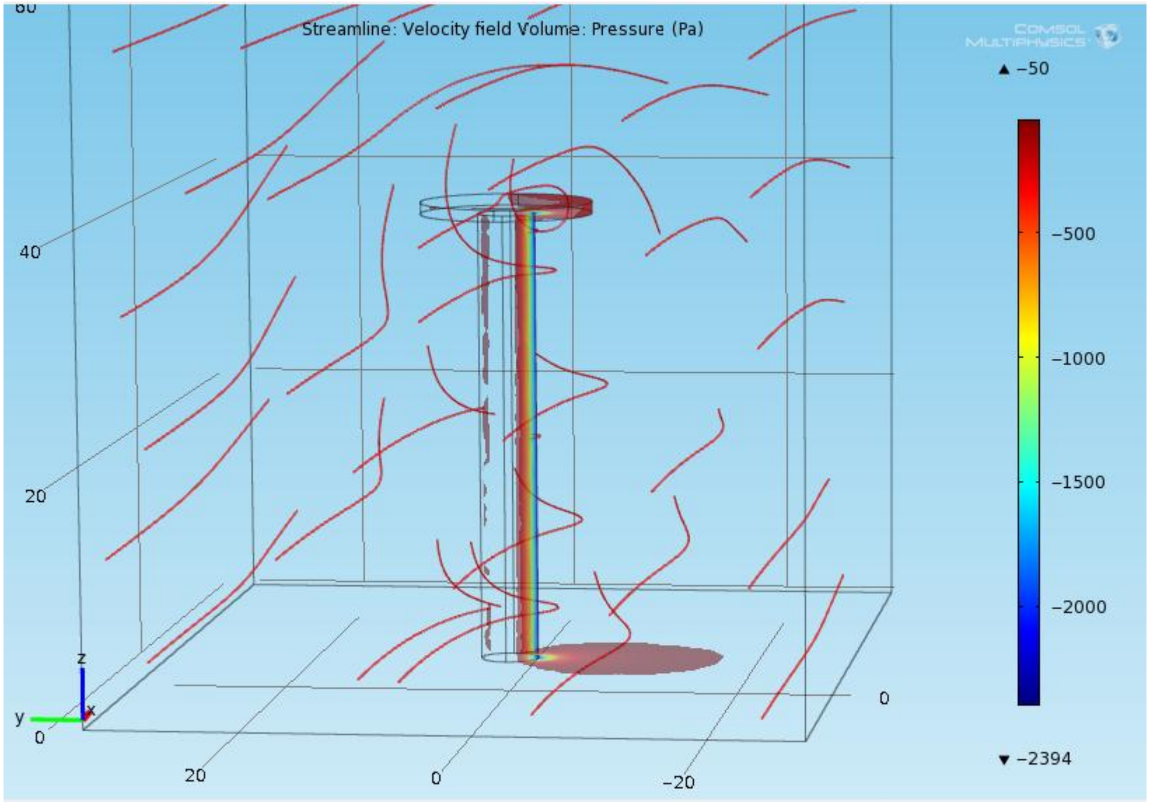

Figure 31: Streamlines and pressure profile on the cylinder viewed from the perspective of the incoming flow, AR=8, e/d=3

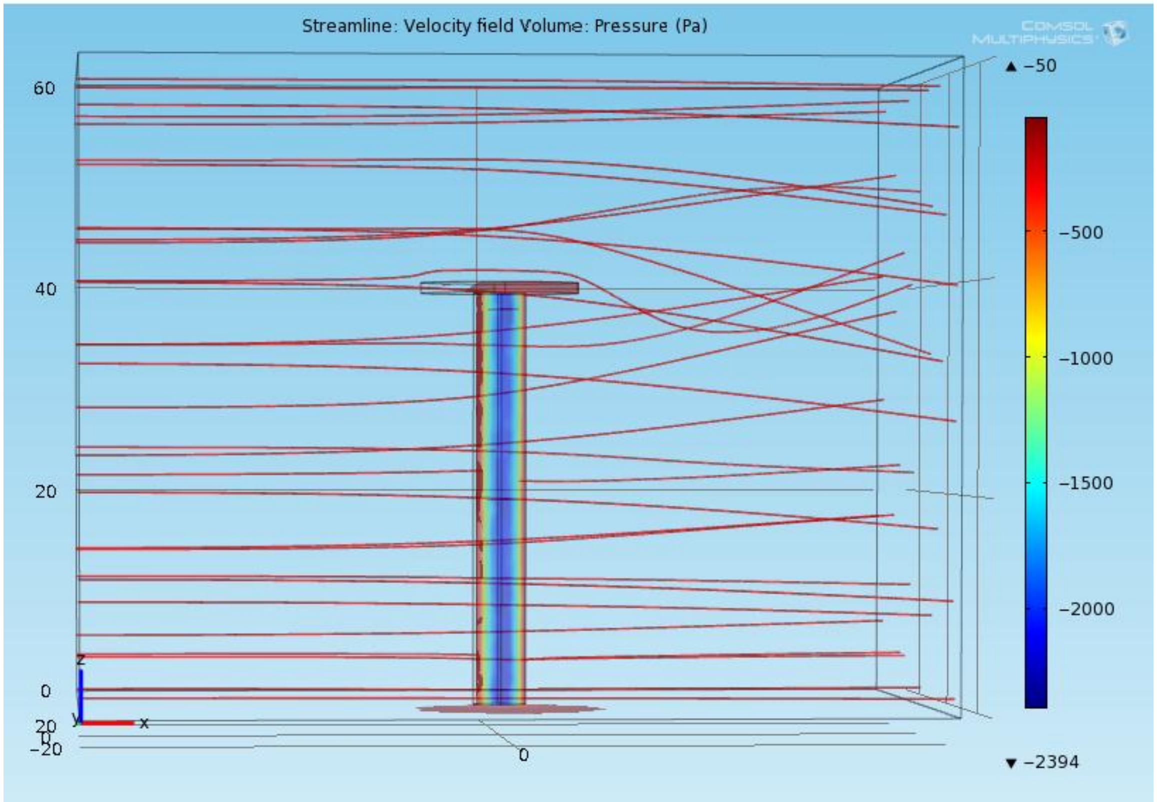

Figure 32: Streamlines and pressure profile on the cylinder viewed from the low pressure side of the cylinder, AR=8, e/d=3

First, however, it is important to look a little more closely at exactly what is happening around the cap. The figure below shows the pressure at a height of 39.5 meters or exactly in the middle of the 40-meter turbine's cap. Pressure regions similar to those observed on the body of the cylinder can be seen here too; however, the magnitude of the pressure difference on the opposite sides of the cap is much less than that on the sides of the body. Due to the fact that it has a greater radius, the cylinder cap is spinning much faster than the cylinder body. Thus, it should create higher velocities and a greater pressure difference. Unlike the cylinder's body, though, the air can escape high pressure regions by simply moving vertically, which is why this is not the case.

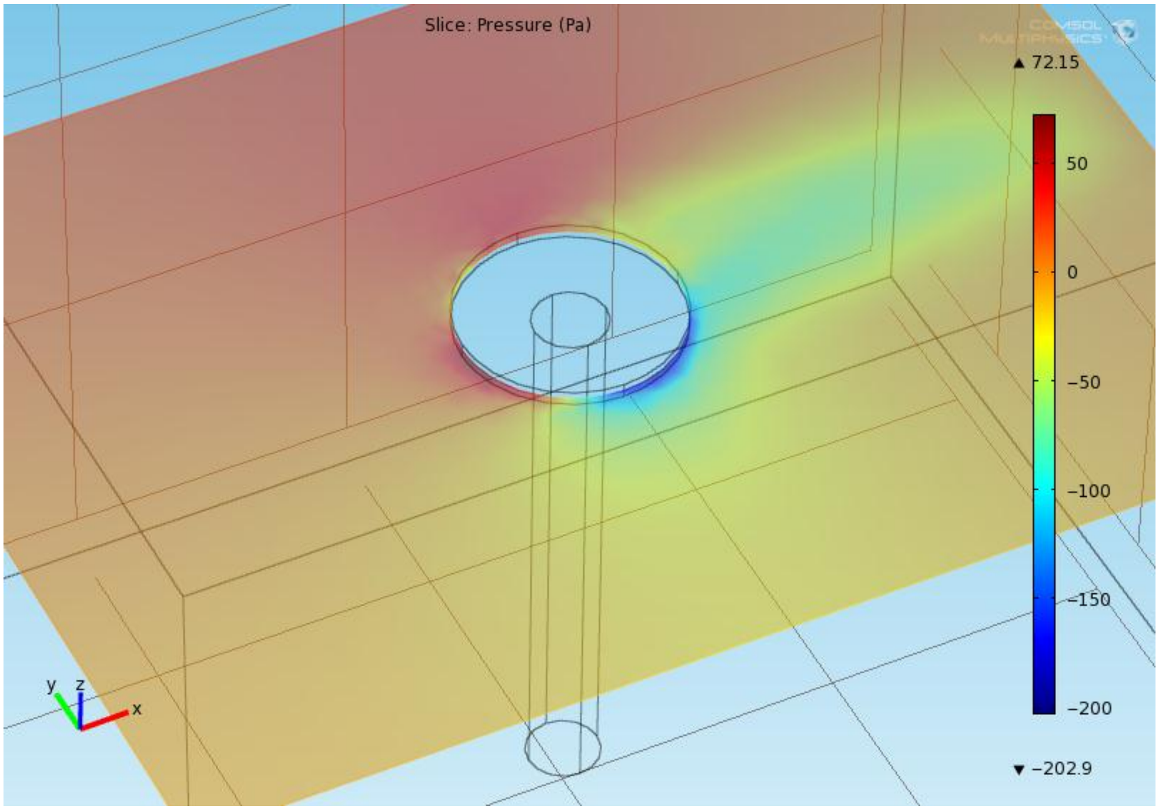

Figure 33: Pressure magnitude around the cylinder cap, AR=8, e/d=3

Taking a look at the velocity profile below, this is indeed what occurs. On the higher pressure side of the cylinder, the flow is diverted upward, and on the lower pressure side of the cylinder it is diverted downward. This is the difference between the 2D and the 3D studies: in 3 dimensions the fluid at the top of the cylinder is mobile in the vertical direction.

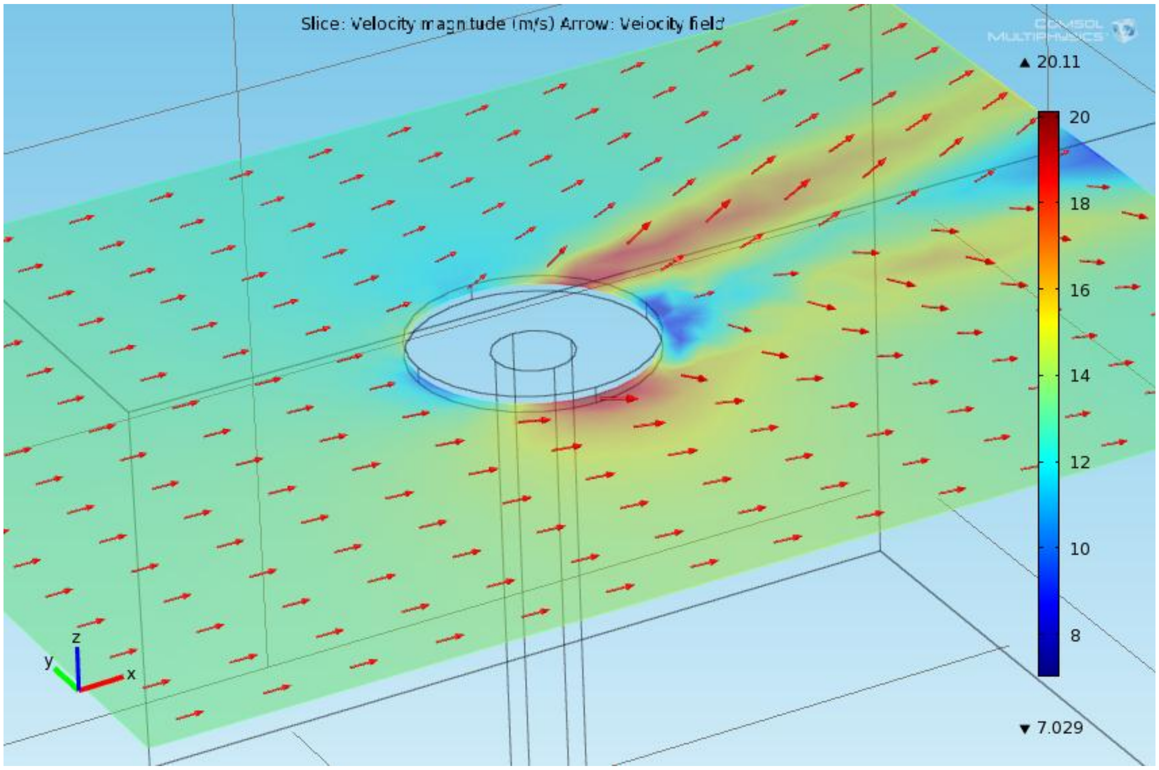

Figure 34: Velocity around the cylinder cap, AR=8, e/d=3

Knowing this, the magnitudes of the pressure differences across the cylinders were plotted as a function of both the aspect ratio and the end cap to cylinder ratio. In order to create more easily comparable results, the actual pressure developed across the cylinder was divided by the cylinder’s aspect ratio. In this way, all of the pressure magnitudes were scaled to a unit length. The plot is directly below. On the x-axis is the end cap length divided by the cylinder diameter, which ranges from 1-3, and on the y-axis is the normalized pressure difference. The different lines represent different aspect ratios.

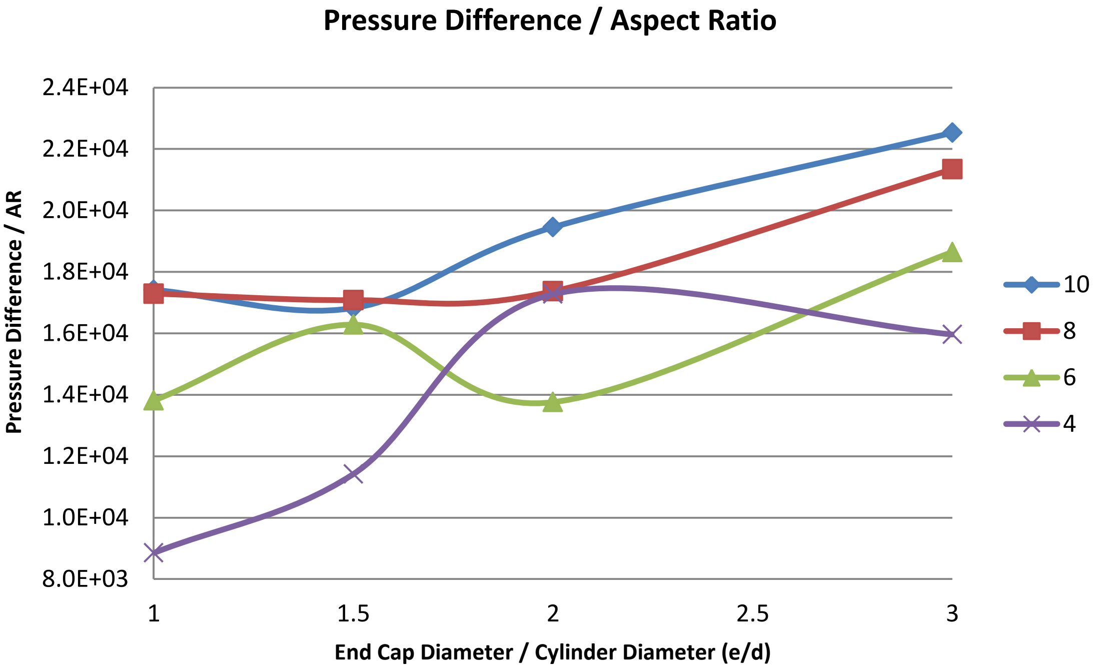

Figure 35: Pressure difference / AR for varying e/d ratios

One clear trend is the increase in the pressure difference with aspect ratio; as aspect ratio increases, so does the force that the cylinder experiences. This is exactly the behavior predicted from aerodynamics in the study of airplane wings: as aspect ratio increases, the coefficient of lift increases and moves closer to that of an actual airfoil with no 3-dimensional effects. In this way, it makes sense for the C_L of the Madaras cylinder to increase with aspect ratio.

The other major trend in the graph is the increase in pressure difference with the end cap length to cylinder diameter ratio. This can be attributed to the fact that the larger the cap, the less the air flow can move vertically. If the cap were infinitely large, the results would be the same as that for a 2D cylinder (assuming no boundary fluid-wall interaction inefficiencies).

Given these two trends, it is clear that the cylinder that will create the most lift and produce the most power will be the one with the greatest aspect ratio and the largest end cap to cylinder diameter ratio. Unfortunately, both of these require a more rigid and heavier structure to prevent buckling and other failure. Additionally, as the end cap ratio increases, more power will be required to rotate the cylinder. The true challenge is designing a cylinder such that net power will be maximized, which requires the optimization of the lift, the rotational inertia, the structure strength, and the friction-producing surfaces to start.

Streamwise Separation Analysis

One important design parameter in these turbines is the distance between each cylinder. Just as in traditional wind turbine farms, the flow behind the turbines can become very turbulent, so some distance is required between the turbines to allow the flow to return to near free flow conditions prior to encountering the second turbine. The streamwise separation distance is the parameter studied here. It should be remembered from previous discussion that the original study by Witford et al. called for a separation between the cars of 215 m.

Streamwise separation distance is important in two locations: 1) when the cylinders are moving in a direction parallel to the wind (just before rotation switches direction), and 2) when the cylinders are moving perpendicular to the wind. For the first scenario, the cylinders were assumed to be most disruptive to each other when rotating in the same direction as they would be right before the first cylinder starts rotating in the opposite direction. In this case, the second cylinder is trying to speed up a faster flow on one side and slow down a slower flow on the other side. If the cylinders had been rotating in opposite directions, the cylinder would be trying to speed up a slow flow and slow down a fast flow, and due to the greater difference in the velocity of the cylinder's walls versus that of the local flow this would probably affect to a lesser extent the pressure differential created by the cylinder. For the second scenario, the cylinders would be separated by a much greater distance, and it was assumed that the direction of rotation was not as pertinent. Thus, only the case where the cylinders were rotating in the same direction was studied.

One other important consideration is the effect of the translational velocity of the cars on the total velocity direction for each cylinder. Unfortunately, this is a very complicated issue that could not be resolved in this analysis. To actually model this translational velocity, a moving mesh would need to be implemented. In addition, multiple cylinders for both the first and second lines of cylinders would need to be modeled since it is likely that the secondary line of cylinders would not encounter the wake of the cylinder directly in front of it but instead they would encounter the wake of a cylinder that had already passed. The amount of computational power required for such a study would be tremendous and was not available. Thus, the translational velocity of the cars was assumed to be zero.

Model Setup

This computational model built in COMSOL consists of two rotating cylinders in a 2D domain. The average fluid flow is directed along the axis of separation so that the second cylinder is located directly behind the first cylinder. The separation distance between the two cylinders is denoted by the parameter r_x, and how it affects the performance of the cylinders is analyzed. To simplify the model, parameters were chosen so that the incoming flow would be laminar with a Reynolds number of 1000. For a cylinder diameter of 1 m, the density of the fluid was 1 kg/m^3, the viscosity of the fluid was 10^{-2} kg/(m*s), and the velocity of the fluid was 10 m/s. The rotational speed of the cylinders was 5 m/s at the radius of the cylinder.

All length dimensions that follow in this paragraph are given in meters. The domain is composed of a circle of radius 40 centered about x = 0 and y = 0 combined in union with a square of side length 40 and center at x = 20, y = 0 in union with a rectangle of height 40 and width r centered about $x = r_x/2 + 40$ and y = 0 where r_z is the distance between the two rotating cylinders. The first cylinder is located at x = 0 and y = 0 while the second cylinder is located at $x = r_x$ and y = 0. This domain adequately captured all flow patterns associated with the two rotating cylinders.

The boundary conditions include an inlet on the curve of the semicircle with a velocity of 10 m/s in the x-direction and zero velocity in the y-direction (it should be noted that a curved mesh inlet was used to mimic a similar example from the COMSOL tutorials posted by their documentation team). At the opposite end of the domain an open boundary condition was used to allow the fluid to leave the domain. The walls located along y = -20 and y = 20 were specified with a slip condition so that there would be minimal boundary effect on the flow while still preventing any of the fluid from leaving the domain via the top and bottom walls. The rotation of the two cylinders was the most difficult condition to model. A moving wall condition was used with x-velocity *Uw*sin(atan2(y,x))* and y-velocity *Uw*cos(atan2(y,x))* where *Uw* is the speed of the wall and is equal to 5 m/s. For the second cylinder, a correction factor of $x-r_x$ was used (i.e. the x-velocity of the second cylinder was *Uw*sin(atan2(y,x-rx))* and the y-velocity of the second cylinder was *Uw*cos(atan2(y,x-rx))*). The reason this was necessary is that the second cylinder is offset from the x-origin by the amount *rx*; subtracting this from the value of *x* will yield the correct arctangent value.

Dimensional analysis is an important part of fluid mechanics, and here it can be applied as well. The Reynolds number is common to all flows, and its value of 1000 indicates that this flow field is laminar. However, a more interesting non-dimensional parameter that is applicable specifically to this flow field is the ratio of the rotational speed of the cylinder to the translational speed of the flow or, in mathematical terms, *wd/U*. For this study, the ratio is equivalent to 0.5 (5 m/s divided by 10 m/s). This indicates that the flow is most likely dominated by the lateral motion. This assumption is validated visually from the velocity fields generated, and it is important to note that although it is desirable to have cylinders rotating quickly for the purpose of power production, if the wake is thrown to the side by the rotating cylinder, defining a streamwise separation distance becomes pointless. This was not the purpose of this study since the cylinders could be set to rotate extremely quickly, and (provided that the model converged) be placed almost on top of each other with no problems. Instead, a flow in which the rotational effects did not dominate the translational effects was desired.

When meshing, it was important to use a very fine mesh so that it could capture all the intricacies of the flow near the cylinders. To achieve this, a boundary layer condition consisting of 12 boundary layers at a stretching factor of 1.2 and a thickness adjustment factor of 1 was used. This resulted in the dense mesh around the cylinder as shown in the zoomed-in part of the figure below. Then an extremely fine mesh was generated over the rest of the domain, resulting in the below mesh.

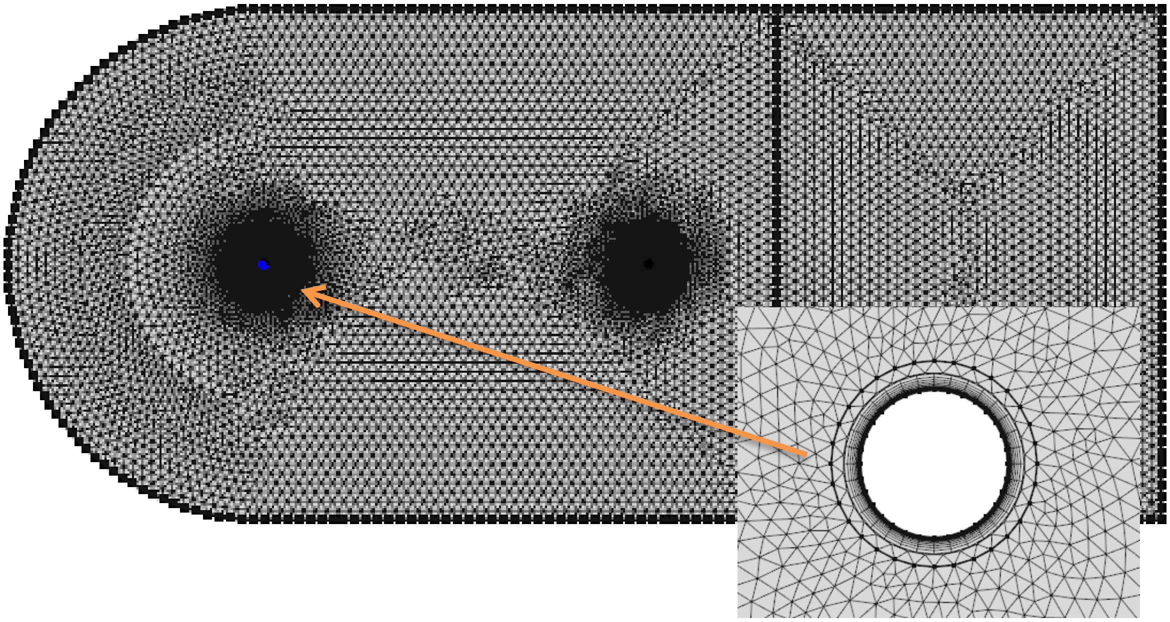

Figure 36: Mesh for streamwise separation analysis

The mesh statistics are shown to the right. The mesh consists of 18,037 elements, of which 95.7% were triangular elements. Adaptive mesh refinement was performed with very limited success. The minimum element quality is bad, but it is clear that not many elements are of this quality since the overall element quality is 0.9295, which is very acceptable.

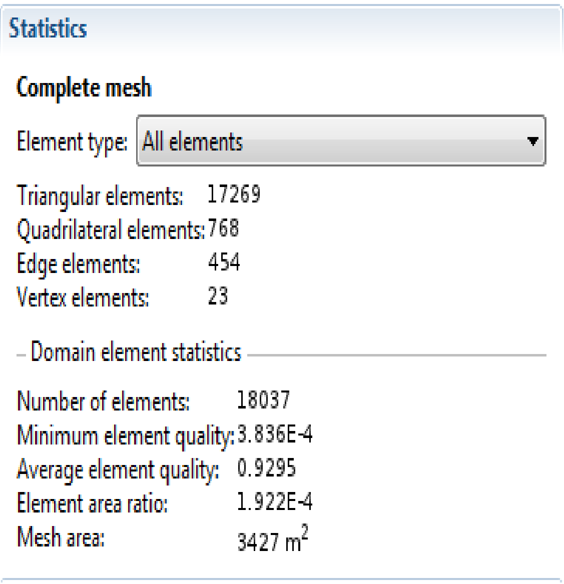

Statistics

Complete mesh

Element type: All elements

Triangular elements: 17269
Quadrilateral elements: 768
Edge elements: 454
Vertex elements: 23

Domain element statistics

Number of elements: 18037
Minimum element quality: 3.836E-4
Average element quality: 0.9295
Element area ratio: 1.922E-4
Mesh area: 3427 m^2

Figure 37: Mesh statistics

The COMSOL functions used to create this model are those available with the time-dependent laminar flow study. The flow is assumed to be incompressible, so the equations used to model it are simply the conservation of momentum and the conservation of mass (continuity) equations:

$$\begin{aligned}
&\rho\frac{\partial \mathbf{u}}{\partial t} + \rho(\mathbf{u}\cdot\nabla)\mathbf{u} = \\
&\nabla\cdot\left[-p\mathbf{I} + \mu\left(\nabla\mathbf{u} + (\nabla\mathbf{u})^T\right)\right] + \mathbf{F} \\
&\rho\nabla\cdot\mathbf{u} = 0
\end{aligned}$$

in which ρ is the density, u is the velocity, and F is the force acting on a fluid element. The dependent variables are the velocity components, the pressure, the reciprocal wall distance, the corrected velocity components, and the corrected pressure. COMSOL also lists turbulent dissipation rate, specific dissipation rate, and undamped turbulent kinematic viscosity as dependent variables, but since this is a laminar flow problem, these variables should be zero.

Achieving Convergence

Rather than starting with the whole model first and expecting convergence, an iterative approach was used to build up the model. The first actual simulation was performed with just one stationary cylinder located at x = 0 and y = 0. To obtain a converging model, the velocity of the inflow needed to be increased gradually or else the model would not be able to obtain initial conditions, and the simulation would fail immediately. To remedy this problem, both the inflow velocity and the initial conditions of the flow (both 10 m/s) were multiplied by a step function with a magnitude of 1 so that the velocity increased gradually over a time of 80 seconds. (Note that the built-in COMSOL "step function" is smooth and is not an instantaneous increment from 0 to 1; the distance over which the step function increases in value is the "smoothing section" discussed.)

The next issue was similar: the model diverged as soon as the cylinder started rotating. Again, the solution was found in a step function with a smoothing section of 100 seconds in length. The step function began at time t = 100 s and ended at t = 200 s (chosen so that the fluid flow in the model was steady-state before the cylinder starting rotating). This ended up fixing the cylinder convergence issue, and the rotation of the cylinder produced a steady offset region with some recirculation

The last component to be added to the model, and definitely the most difficult, was the second rotating cylinder. The cylinder was initially added pretty close to the first cylinder (r_x = 10), but this model would not converge no matter what was tried. The cylinder had to be placed further back, and when it was placed at x = 30 (separation between the mid-lines of 30 meters and between the walls of 25 meters) the model converged. This didn't prove to be an issue because no cylinder could be placed less than 30 meters from the first cylinder in an actual Madaras plant since the cylinders are on a large circular (or near-circular) track.

After the model with a stationary second cylinder converged, the second cylinder rotation had to be incorporated. Initially, rotation of the second cylinder was set equal to rotation of the first cylinder so that at t = 100 s the cylinder began rotating and at t = 200 s it had reached full speed. However, even when the smoothing of the step function was increased so that it was spread over a greater amount of time, the model still would not converge. Instead, an alternative approach was taken in which first the first cylinder would be sped up to full rotational speed and then the second cylinder would be sped up.

To get this model to converge, a larger smoothing was needed for the first cylinder so that it occurred over the region t = 100 s to t = 300 s and the second cylinder sped up over the region t = 425 s to t = 675 s. After these modifications, the entire model finally functioned as desired and the separation analysis could begin.

Results

When determining how far the turbines should be spaced, the most important design parameter is the pressure developed across each cylinder and the requirement that it does not decrease significantly for the second cylinder. To determine how this pressure varied with separation distance, the distance was varied to from 3200 meters to 30 meters. The full data is appended.

The figure below shows the velocity magnitude of the flow just before the rotation of the cylinders starts for the case where r = 30. As can be seen, the second cylinder is located in the slow-moving wake of the first cylinder where the velocity is approximately 6 m/s (much lower than the ambient 10 m/s). It should be noted that the dark blue region behind each cylinder is where the flow is recirculating.

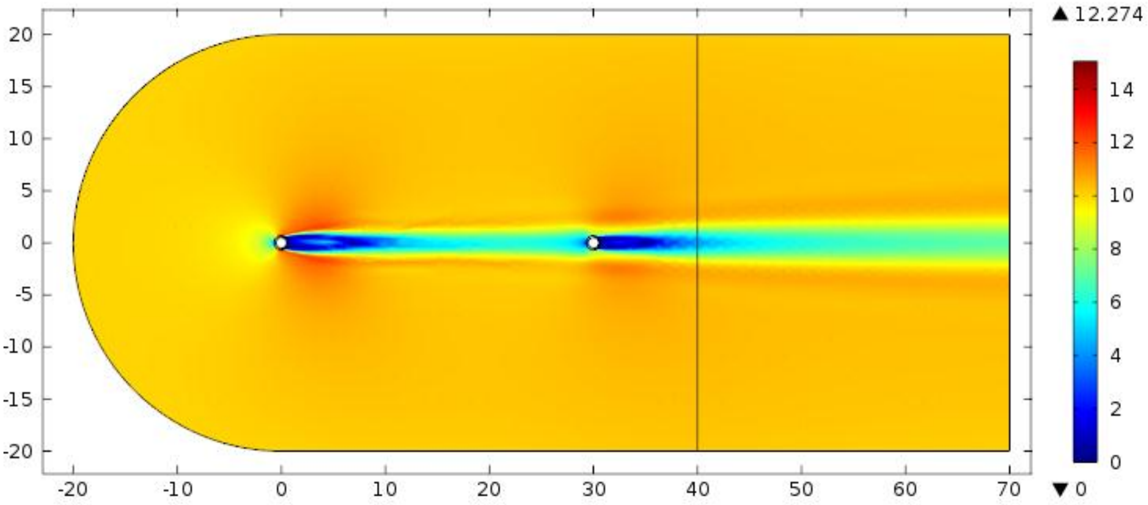

Figure 38: Steady flow (velocity profile)

Then, the first cylinder starts rotating as shown in the figure below. As the first cylinder rotates, it creates a region of faster-moving fluid on its upper surface and slower-moving fluid on its lower surface. This also causes the flow that encounters the second cylinder to be slower on the bottom side than on the top side. If the second cylinder is rotating counter-clockwise also, this means that it will be slowing down the lower fluid and speeding up the upper fluid even more.

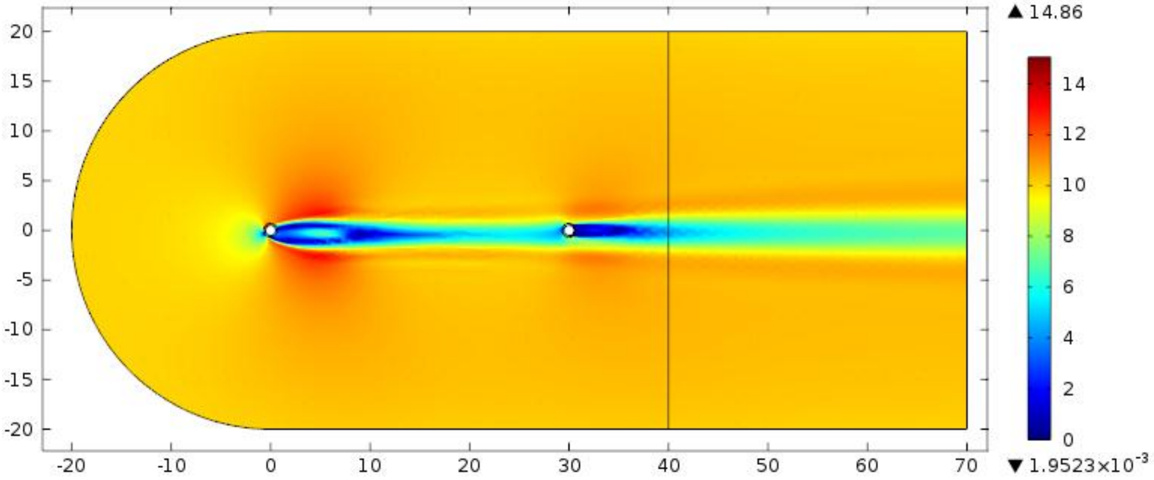

Figure 39: First cylinder rotating (velocity profile)

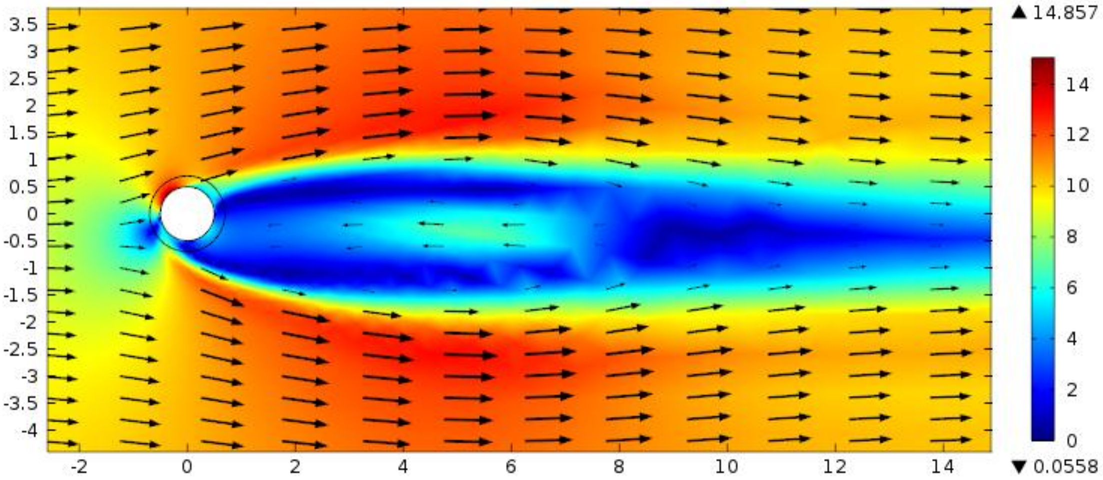

Figure 40: Close-up of cylinder in rotation (velocity profile)

By the end of the simulation, both cylinders were rotating as shown in figure 41. To compare the flow near each cylinder, the velocity of a ring about each cylinder was used. This ring is 2 meters in diameter, and the maximum velocity, minimum velocity, and average velocity about this ring were calculated. One important thing to note is that the magnitude of the maximum velocity between the case of one cylinder rotating and that of both cylinders rotating is zero for $r_x = 30$ m. For this case the second cylinder is located in the slow-moving wake of the first cylinder, so while it does in fact speed up the flow, it does not cause the flow to go faster than the point on the top of the first cylinder. This will be important because it is the difference in the velocity of the flow that causes a pressure differential to develop across the flow.

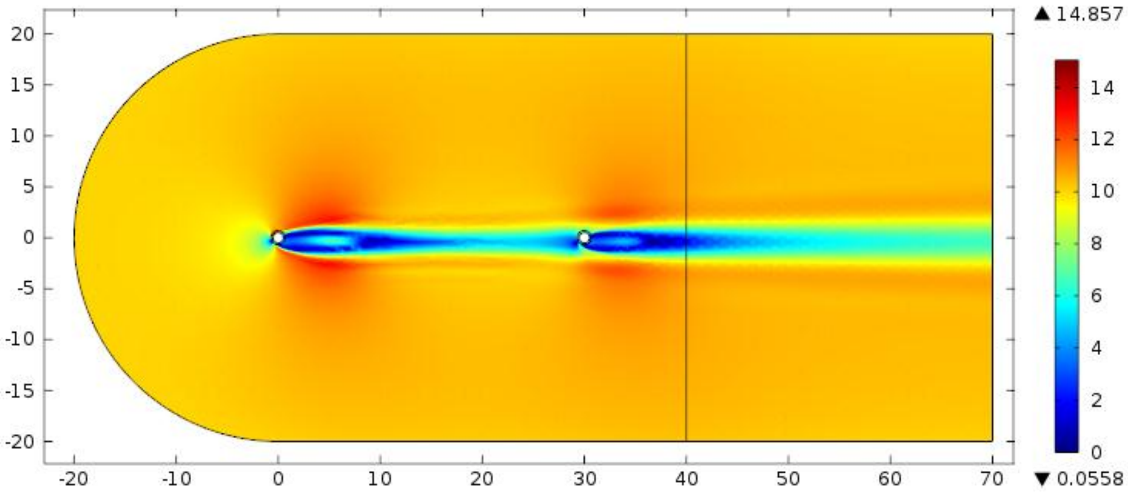

Figure 41: Both cylinders rotating (velocity profile)

The pressure around the cylinders when steady-state had been achieved is shown for the same case ($r_x = 30$) in figure 42 below. As can be seen, both the highest and lowest pressures occur on the first cylinder as evidenced by the darker blues and reds. This signifies that the second cylinder develops less pressure across it and thus is not as effective in producing power as the first cylinder is. However, this is just one case, and since the cylinders are so close together the result may have been obvious prior to the study. As mentioned previously, many different values for separation distances were analyzed all the way up to $r_x = 3200$ m.

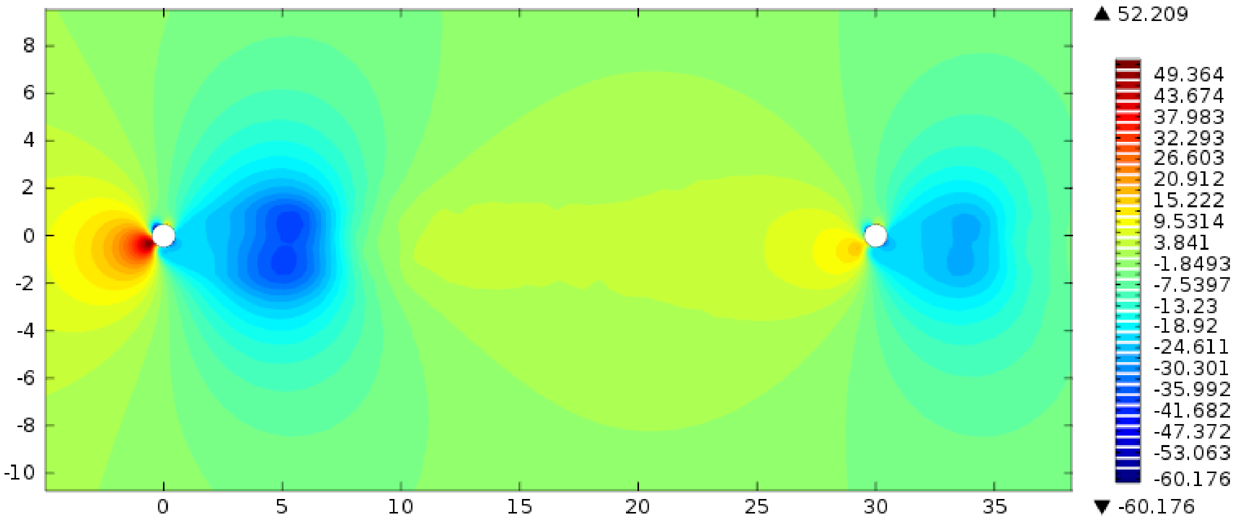

Figure 42: Both cylinders rotating (pressure profile)

Plots for other separation distances are not shown, but as the second cylinder is removed from the vicinity of the first cylinder, the pressure developed across it increases up until a limit. This limit is just above 21 Pa. The pressure across the first cylinder varies a little as the separation distance changes, which is probably caused in part by the backpressure created from the second cylinder, but over the full range of separation distances its average is 21.3 Pa, and its standard deviation is pretty low. Thus, when the second cylinder is separated from the first by 3200 meters, the pressure difference across it has not only converged to a value as shown in the graph below, but the cylinder is also generating the same pressure difference across it as the first cylinder. When the second cylinder is separated this far from the first both the pressure profile and the velocity profile appear similar to that across the first cylinder. Looking at the below plot, for a separation distance of only 30 meters the pressure gradient is actually in the opposite direction. This means that the flow from the first turbine interacts and so heavily interferes with the functioning of the second turbine that the second turbine experiences negative lift. Clearly this is undesirable as is any sub-peak output. While a separation distance of 3200 meters might give near-perfect turbine independence, a separation distance of 400 meters may be more reasonable and gives across the second cylinder a pressure difference only 14.3% less than that across the first cylinder.

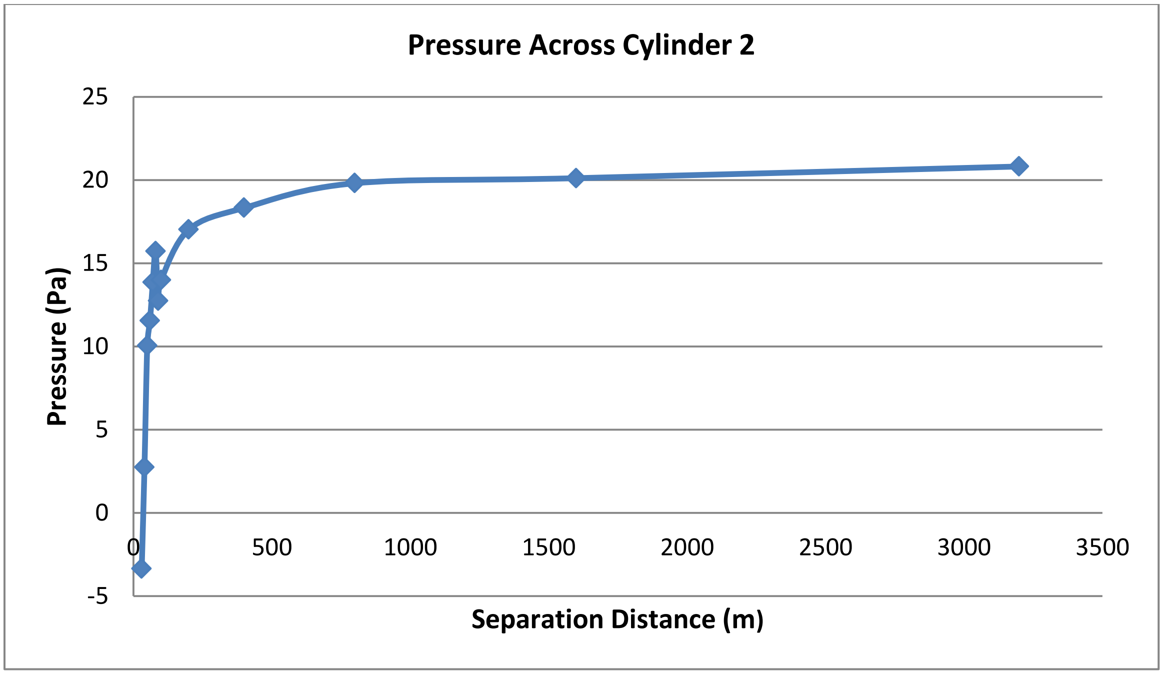

Figure 43: Plot of pressure difference for second cylinder

Table 6: Pressure differences across both cylinders and total parameter percent deviation as separation distance varies

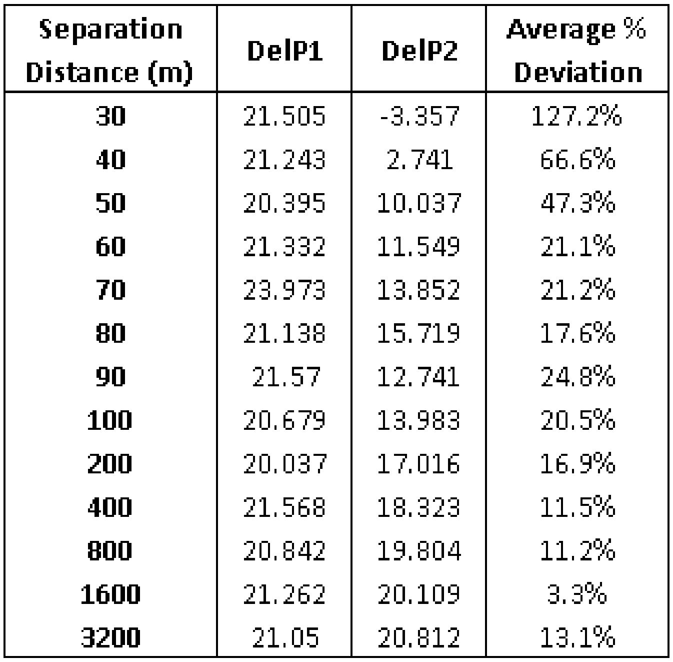

Separation Distance (m)	DelP1	DelP2	Average % Deviation
30	21.505	-3.357	127.2%
40	21.243	2.741	66.6%
50	20.395	10.037	47.3%
60	21.332	11.549	21.1%
70	23.973	13.852	21.2%
80	21.138	15.719	17.6%
90	21.57	12.741	24.8%
100	20.679	13.983	20.5%
200	20.037	17.016	16.9%
400	21.568	18.323	11.5%
800	20.842	19.804	11.2%
1600	21.262	20.109	3.3%
3200	21.05	20.812	13.1%

This was briefly mentioned previously, but in addition to pressure across cylinders, some other values were computed for comparison and in order to determine where convergence occurs. These include the pressure on the top, the pressure on the bottom, the maximum velocity around a diameter of 2 m, the minimum velocity, and the average velocity; all of the values for these simulations are listed in the appendix. After obtaining these values, the percent deviation between the first cylinder values and the second cylinder values was determined by the formula: abs((x1-x2)/x1) where x signifies one of the aforementioned variables. The value for the percent deviation decreases rapidly from 127% for the first point ($r_x = 30$) to 13% for the last point ($r_x = 3200$) as shown in table 6.

Spanwise Separation Analysis

The spanwise separation analysis was performed using the exact same setup as the streamwise separation analysis; however, the variable changed between each study was the distance between the cylinders in the spanwise direction. To ensure that the cylinders were adequately interfering with each other for a spanwise separation of 0 meters, the cylinders were placed 50 meters apart in the streamwise direction since at this distance it is known from the previous study that there is significant interference. The only change that was required in the model between the previous analysis and this analysis was the introduction of the spanwise separation variable r_y. This change necessitated an updated wall velocity to account for the spanwise separation, so that the x-velocity became *Uw*step3((t)[1/s])*sin(atan2(y-ry,x-rx))* and the equation for the y-velocity became *Uw*step3((t)[1/s])*cos(atan2(y-ry,x-rx))* for the second cylinder. The separation distance was varied between 0 and 12 meters and the results are shown below.

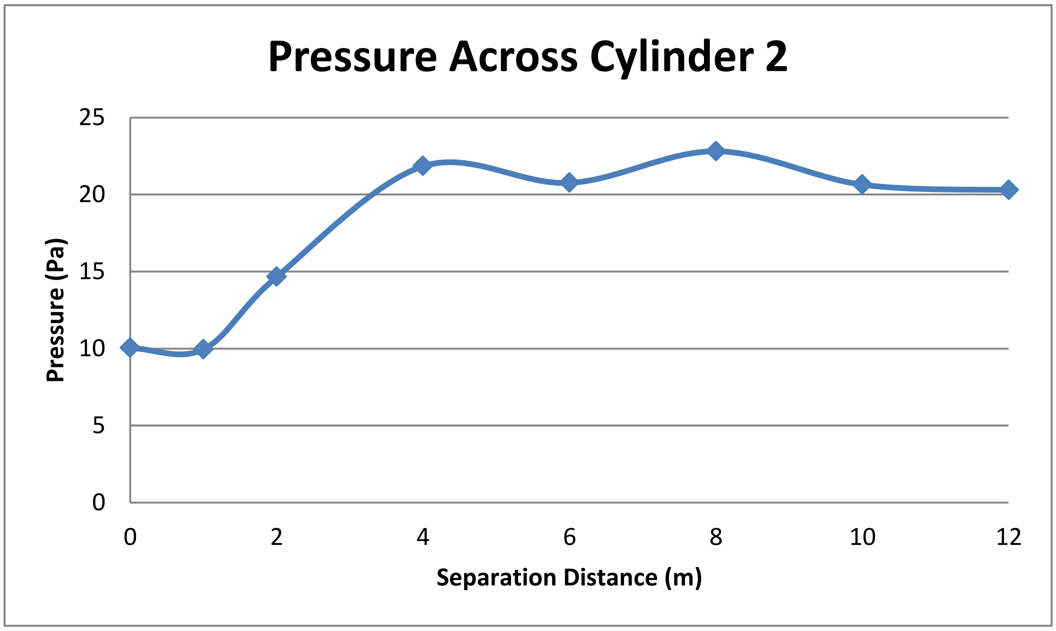

Figure 44: Pressure across the second cylinder as spanwise separation distance is varied

As can be seen, after about 4 meters of separation, the pressure difference across the second cylinder reaches an asymptote of just over 20 Pa as expected. Below is a plot showing the velocity magnitude for a separation of 4 meters. It’s clear from this visual that the second cylinder is still in the path of the first cylinder’s wake. However, the cylinder in this case must be sufficiently removed from the very slow moving central section of the wake so that the cylinder is unaffected by it. Removing the cylinder by 12 meters shows that the wake from the first cylinder and the second cylinder are almost completely independent.

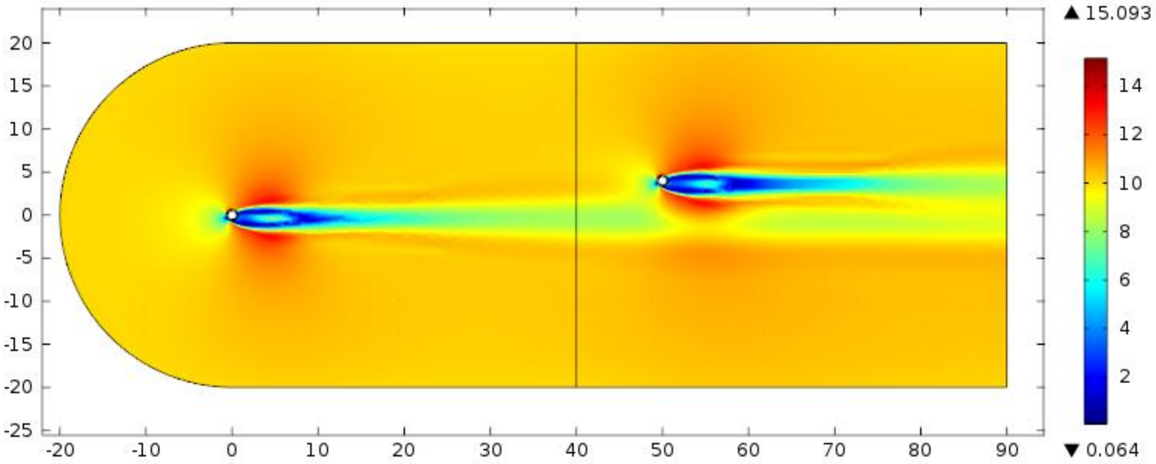

Figure 45: Two cylinders shown at a separation distance of 4 meters

One item of interest here is the fact that the slow region of the wake created by the first cylinder is surrounded by a sheath of faster moving air. In figure 46, the velocity range plotted has been changed to between 9 m/s and 11 m/s to allow easier viewing of the differences of velocity around the wake of the first cylinder. Clearly, the second cylinder is located not in ambient air flowing at 10 m/s, but in air at a faster velocity somewhere around 10.5 m/s. Clearly this affects how the cylinder performs, and this is one of the probable causes of the fluctuations in the exact value of the pressure across the cylinder after it surpasses 4 meters separation (in the plot above, there are 2 points that show elevated pressures: that of 4 meters separation and that of 8 meters separation).

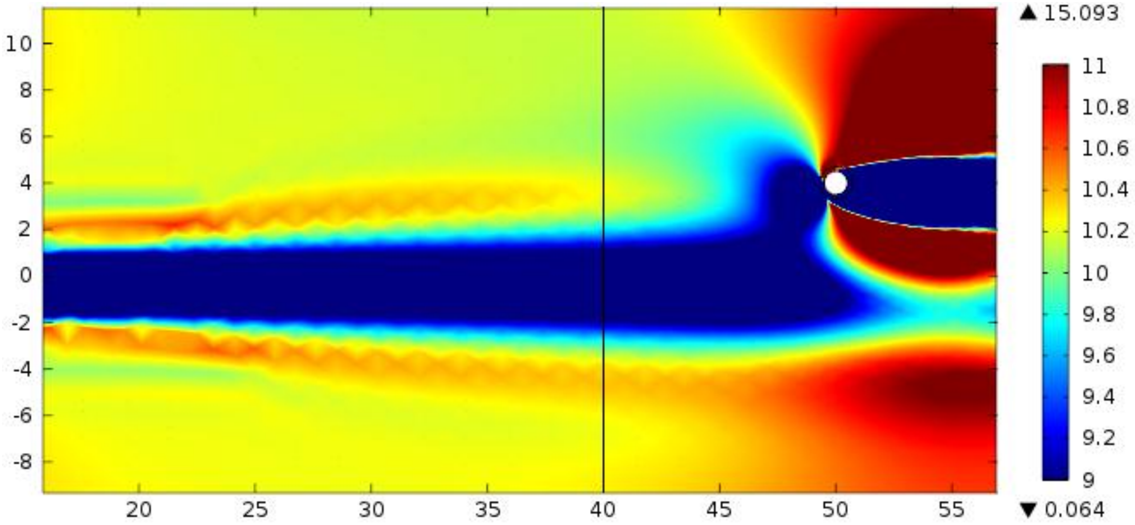

Figure 46: Velocity profile illuminating the wake of the first cylinder

The pressure contour for the cylinders is shown below in figure 47. The figure shows near-identical pressure distribution across the two different cylinders. The only difference that can be seen between the cylinders is that the rear low-pressure region of the second cylinder appears to extend slightly farther out. However, the region of interest is that around the cylinder surface itself, so this does not pose a problem.

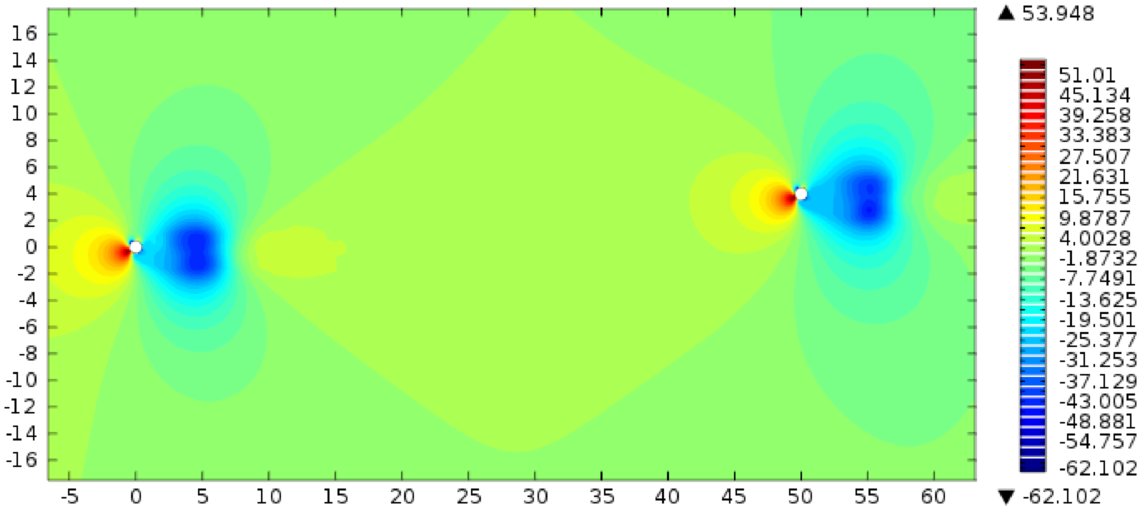

Figure 47: Pressure contours for the two cylinders at a spanwise separation distance of 4 meters

It can be safely stated that for the parameters chosen here, 4 times the diameter of the cylinder is an adequate separation distance. Unlike the previous study, the dissipation of the first cylinder's wake is not necessary, which is why a much smaller distance is required.

A further study to analyze the spanwise separation distance when the cylinders are rotating in opposite directions would be desirable, but limited computational time precluded that study from being part of this research. In addition, as can be seen in the velocity magnitude profile, it appears that at these rotational speeds the wake from the first cylinder is most affected by the pressure drag.

Weight Carrying Optimization Study

After the preliminary force validation, it was necessary to perform some finite element analysis (FEA) to determine whether the turbine could stand up to the forces exerted on it. The solid modeling was done using ProEngineer 5.0 and is based upon the results obtained from the CFD analysis – a cylinder with an aspect ratio of 8 and an e/d ratio of 3. Although an aspect ratio of 10 improved performance slightly, it was determined that the additional cost and structural instability caused by this increase in height would not be worth the marginal benefit. The most important part to decide was how to design the interior bracing to withstand buckling but also endure the lateral effects of the wind and the torsional moment created by the shear from the wind. First, however, a turbine was designed to carry its own weight since this would be by far the largest force affecting the structural integrity of the turbine.

Some sources were referenced to help with the design of the bracing, but much of the interest in shell design is focused on the improvement of oil pipeline design. Oil pipelines experience very different forces than Madaras cylinders since they have liquid inside them and sometimes outside of them (depending on whether they are transporting it large distances along the ground or vertically to an oil platform). In either case, the major concern for oil pipelines is the lateral pressure on the cylinder walls and not cylinder buckling. Though some of the material on shell design was instructive, most is not applicable to this study due to the difference in the type of forces experienced by Madaras turbines compared with oil pipelines. For this reason, the majority of the design was done iteratively using finite element analysis.

Important parameters when performing an FEA analysis include the material properties, the constraints, and the loads to which the structure is subjected. The model was built in ProEngineer5.0, and the material used was the standard “Steel” provided by ProEngineer. Its properties can be seen in the figure below. These properties are within the range of steel material properties given by MatWeb. Structural steel was used in this study though it is possible a more malleable alloy would be required to make the desired geometry. The load in the model is simply the gravitational load – an acceleration of 9.81 m/s^2 directed in the negative z-direction.

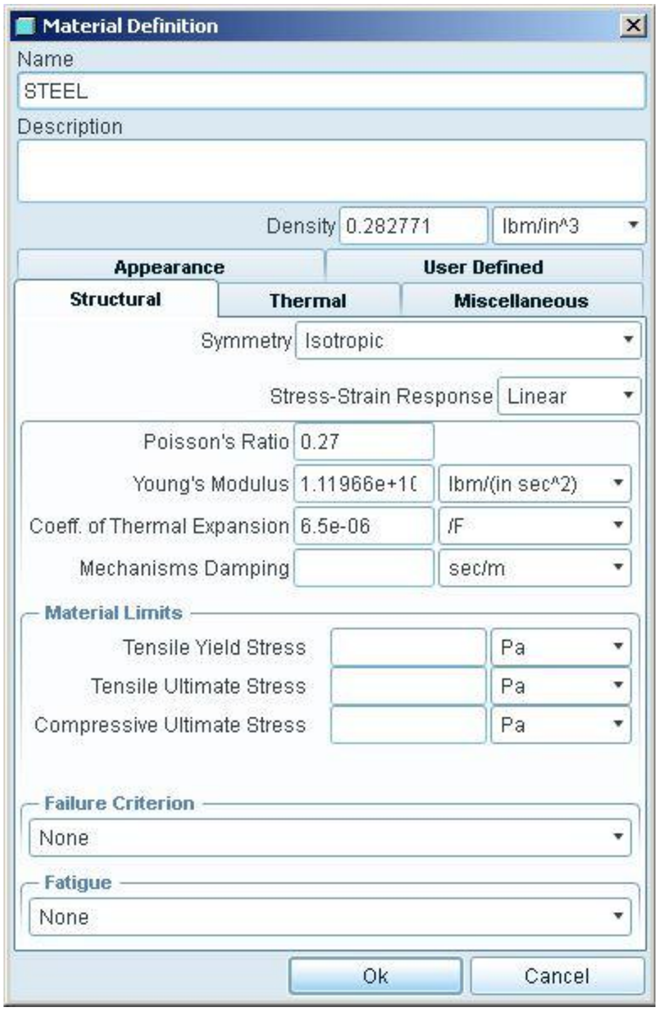
Material Definition

Name
STEEL

Description

Density 0.282771 lbm/in^3

Symmetry Isotropic

Stress-Strain Response Linear

Poisson's Ratio 0.27
Young's Modulus 1.11966e+1 lbm/(in sec^2)
Coeff. of Thermal Expansion 6.5e-06 /F
Mechanisms Damping sec/m

Material Limits
Tensile Yield Stress Pa
Tensile Ultimate Stress Pa
Compressive Ultimate Stress Pa

Failure Criterion
None

Fatigue
None

Figure 48: ProEngineer 5.0 built-in steel properties

First, studies were performed to determine how to internally brace a steel structure that would be subjected solely to gravitational loads to acquire a baseline from which to construct further bracing. Below in figure 49 is a picture of the base model of the original bracing design. The structure is 40 meters tall with a diameter of 5 meters. As mentioned previously, the e/d ratio is 3, so the diameter of the cap is 15 meters. The cylinder wall was originally designed to be the load bearing section of the cylinder, so a thickness of 15 centimeters was used throughout. The circular rods protruding out from the center of the structure to brace the walls are 25 centimeters in diameter. The circular structures that they attach to represent bearings that would be modeled more in depth later (and with a secondary central connection). For the purpose of analysis, all of the connections were

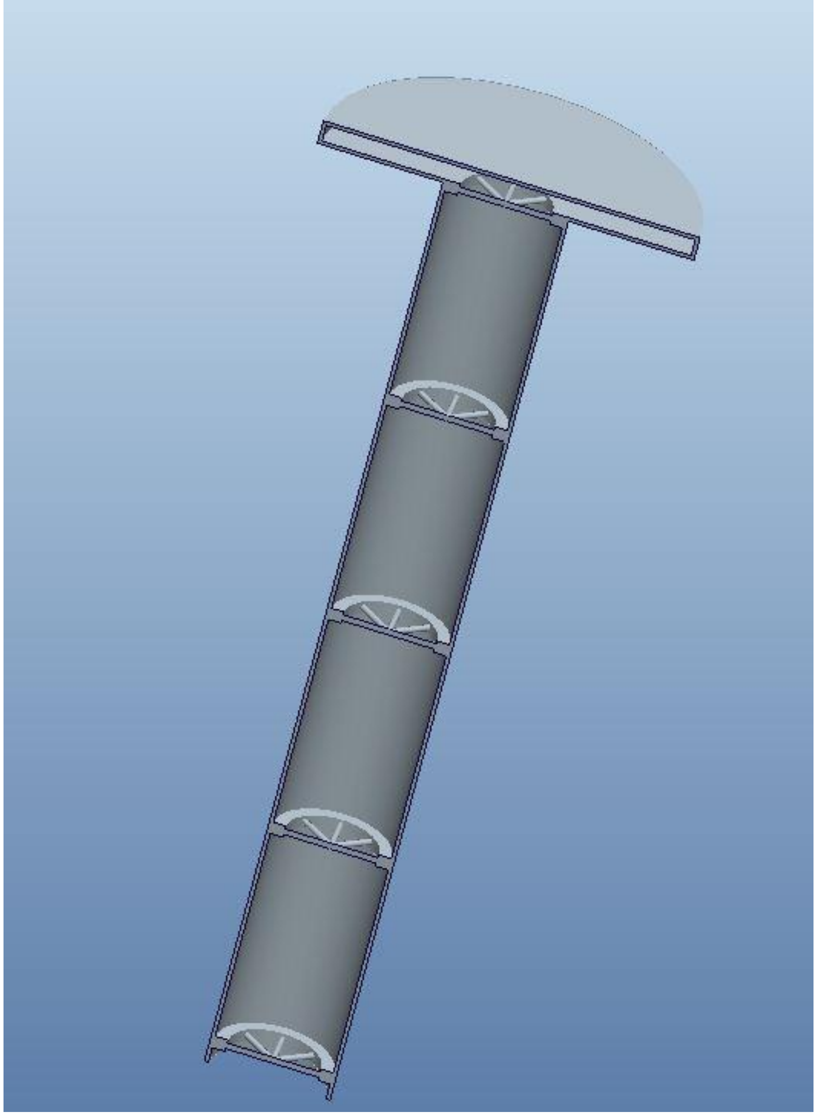

Figure 49: Original Structure Design

assumed to be rigid though in reality there would be welds, pins, and bearings among other connectors. There are clearly many areas that could be improved in this preliminary design, and over several iterations many of them were.

The final weight-optimized design is shown below in figure 50. As can be seen, more central bracing has been added to alleviate the vertical compressive forces to which

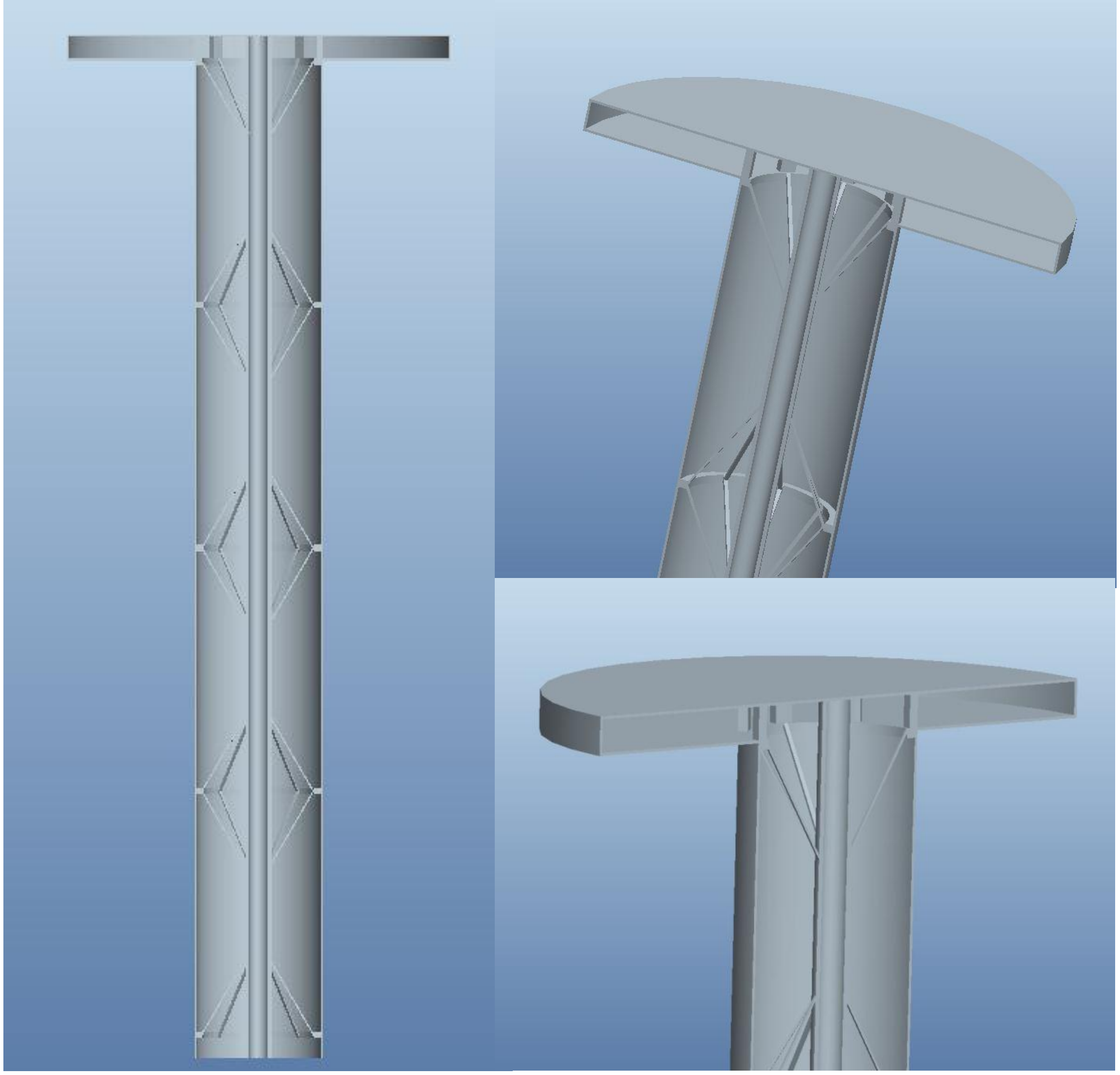

Figure 50: Weight-Optimized Structure

the walls are subject. This along with the central column support resulted in the walls being decreased in thickness by a factor of two to 7.5 centimeters. The central column is hollow in order to reduce total weight since a slightly larger diameter with a hollow interior gives a better strength-to-weight ratio.

It should be noted here that fabrication of the internal bracing may be difficult, and in reality it would most likely consist of pinned connections, not welded connections. However, pinned connections at the ends of each bracing rod could not be modeled for this study just as the bearings could not be properly modeled. In addition, it is unlikely that the external structure would be made as one gigantic cylinder. In reality, it would more likely consist of modules several meters long that could be coupled to each other to form a whole Madaras turbine.

Below is a figure showing the FEA results derived from ProEngineer's built-in utility. The material used was the standard steel defined in ProEngineer and had similar properties to AISI 4000 series steel. The major design constraint for the weight-optimized design was that the highest stress in the model was lower than the steel's fatigue strength. To get the shapes desired, mild steel would most likely have to be used, which has a fatigue strength of about 120-175 MPa (MatWeb).On the right-hand side of the figure are the stress concentrations in megapascals. As can be seen, the highest is 171.2 MPa. Although this is higher than the 120-175 MPa range, it is impossible to tell whether 171.2 MPa is an accurate number or results from computational limitations near sudden geometrical changes. From the coloration of the figure, it is clear that the majority of the structure is well below these fatigue failure limitations and only the ring near the end cap mounting location is close to 120 MPa. In further analyses, the lateral and torsional stresses induced by the cylinder movement and wind force should be studied, though they would most likely affect the cylinder much less than the cylinder's own weight.

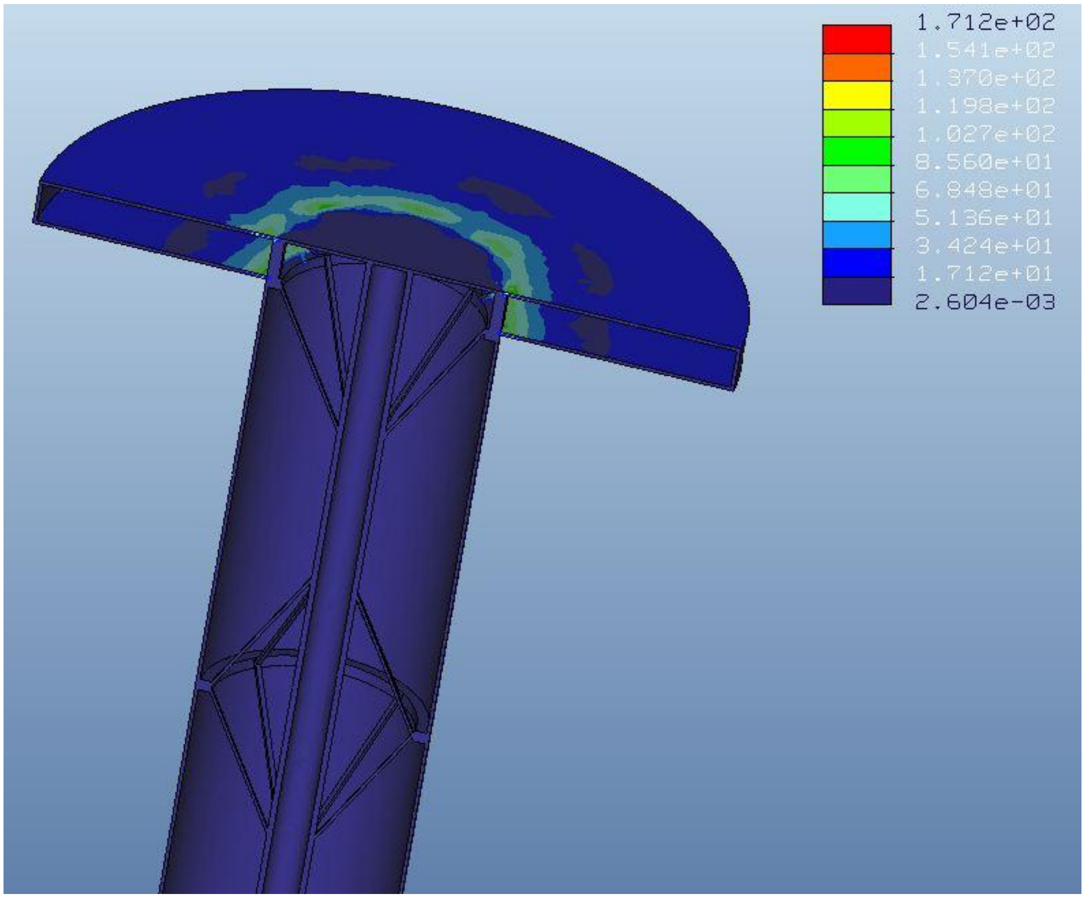

Figure 51: Weight-Optimized FEA

CHAPTER III

CONCLUSIONS AND RECOMMENDATIONS

Madaras Turbine Performance

The Madaras turbine design for use in capturing wind kinetic energy and transforming it into electrical power has been shown to be as effective as if not more effective than traditional turbine designs. Depending upon the Reynolds number associated with the free stream flow and the ratio of the rotational speed of the turbine to the linear speed of the flow, the turbine can achieve a coefficient of lift up to about 15 for the 2D case. The coefficient of lift a Madaras turbine might experience in the 2D case is between 3 and 4. Though much lower than the peak lift coefficient for a rotating 2D cylinder, it is still much greater than the lift coefficient in a typical VAWT turbine of around 1.5 [Ishihara, 2010].

Transitioning to a 3-dimensional case of course involves some efficiency loss when a finite-length cylinder is used. This is due to the end effects on the cylinder in which the higher pressure region is not separated from the lower pressure region, and energy-dissipating eddies are generated. Looking at the data, two major trends are observed: the pressure difference experienced across a cylinder, and thus the coefficient of lift, increases with both the ratio of the end cap diameter to the cylinder diameter and the aspect ratio. Each of these trends is to be expected since a larger aspect ratio and a greater e/d ratio are both closer approximations to the ideal infinitely long cylinder. Clearly, the tallest cylinder with the largest cap is desired for power production, but a real

Madaras turbine is limited due to the structure and strength of materials as well as the cost.

In the design of any wind turbine plant, the spacing between turbines is an important object of study. Placing cylinders too far apart results in higher land and grid connection / maintenance costs; however, placing the cylinders too close together results in low performance as the cylinders interfere with each other. In the streamwise separation distance study, the pressure difference calculated across the first cylinder was a consistent 21 Pa. As the second cylinder was changed from a separation distance of 30 meters (cylinder diameters of 1 meter) to a separation distance of 3200 meters, the pressure difference developed across the second cylinder approached an asymptote at the same value of 21 Pa. Here again a compromise must be used to achieve a balance between sufficient cylinder independence and minimal separation distance.

As an attempt to better describe Madaras turbine spacing, the spanwise separation distance was also analyzed. The separation distance was varied from 0 to 12 meters for cylinder diameters of 1 meter. To ensure that the wake from the first cylinder was sufficiently interfering with the second cylinder, the streamwise separation distance was only 50 meters. It was shown that for this separation distance and no spanwise separation, the second cylinder would produce approximately 50% the power that the first cylinder produced. For the spanwise separation distance study, the second cylinder reaches the asymptote of 21 Pa much more quickly than in the streamwise separation analysis: it takes just 4 meters of separation to ensure that the cylinders are sufficiently independent.

Optimal Madaras Plant Design

Based upon the studies performed, an optimal Madaras power plant would consist of cylinders with an aspect ratio of 8 and an end cap to cylinder diameter ratio of 3. This would be the best compromise between performance and practicality in terms of structural design. The structure itself would be a hollow cylinder with a hollow cap on top. Bracing would be needed in the interior of the cap between the top of the cap and the start of the cylinder. A hollow cylinder would be used as the main support on the interior. Welded onto this main support would be many spokes for vertical and lateral bracing. The upper braces from one set of spokes and the lower braces from a different set of spokes would meet up every 5 meters to a large diameter bearing. This bearing would ensure that the exterior cylinder could rotate with low friction while still allowing the central support to hold up the structure.

A drawing of a possible turbine is shown below. The car in this drawing is 12 meters wide and 20 meters long. The wheels are placed at widths of 9 meters and 10 meters; 16 wheels were used to distribute the weight of the vehicle over as much surface as possible. One major difference between this design and previous designs is that there are two weights located on the car that translate from side to side in order to counterbalance the tipping moment. This results in a lower total weight of the car and also a lesser width since less weight is needed to prevent the tipping moment caused by the wind. The reason that two weights were used instead of one is that room was needed in the center of the car for the anchoring of the cylinder.

Figure 52: Rendering of a possible Madaras turbine

The other major design consideration in a Madaras plant is the track. The actual number of cars on the track and the size of the track are very complicated issues. Studies performed in this analysis have shown that there is a minimum amount of separation distance necessary to have effective and independent turbines. For the streamwise direction this value was determined to be 400 times the diameter of the cylinders, and for the spanwise direction this value was determined to be only 4 times the diameter of the cylinders; in the spanwise direction a separation coefficient can be much less due to the fact that the second cylinder is not directly behind the first cylinder. The study performed by Whitford et al. suggested an oval shaped track with an end diameter of 1372 meters and a straight-length section of 18,300 meters. Using a cylinder diameter of 5 meters, the recommended end diameter of the track would actually be 2000 meters. At the same time, it is difficult to tell how the cylinders may affect each other when they are moving. Due to the fact that a cylinder is not directly behind another cylinder most of the time, the low spanwise separation distance necessary may result in a smaller diameter track being possible.

For illustration purposes, the oval track below has end diameters of 2000 meters and a spacing of 2000 meters between the centers of these ends. This results in a track that is 4000 meters long at its longest point and 2000 meters wide at its widest point. The turbines on this track are spaced 200 meters apart. It should be noted that the turbines appear more close to one another than they actually are. Since this is an overhead view, the part of the turbine that is seen is the 15 meter cap, not the 5 meter body.

Figure 53: Overhead view of an oval track set up with end diameters of 2000 meters

Further Studies

One point that requires further analysis is the placement of the motor that rotates the cylinder. Ideally, the motor would be located in the car body of the turbine at the base of the cylinder. This would create a lower center of gravity and cause the cylinder to be less prone to tipping. One major flaw in this design is that it requires a long driveshaft to transfer the power between the motor and the top of the cylinder where the torque must be applied. This is in fact the reason that modern VAWT designs have the electrical generator located on the very top of the support just behind the turbine blades' hub. The vertical height of a Madaras turbine is less than that of a VAWT, but it may still be too great to avoid failure in the driveshaft with a reasonable size shaft.

Another point of interest is how the cylinders would actually affect each other in a full plant setup. Streamwise and spanwise separation analyses were performed here, but a large-scale analysis involving multiple cylinders moving about a track would be very enlightening. Due to the fact that the spacing between the cars is much greater than the actual cylinder diameters, in a real Madaras plant, a turbine would spend very little time directly behind another turbine. However, there are also other effects to consider like the transient nature of the turbines' movement along the track. If a sufficient amount of time had not passed between when one cylinder passes through a point on the track and when a second cylinder passes through the same point, it is probable that the second cylinder would experience lower power production. A transient study would need to be performed both with cylinders moving through a point and, if computational power or experimental ability permits, with many cylinders moving along a track.

Final Remarks

The studies performed above are certainly an excellent start toward verifying the potential of a Madaras power plant but are by no means the end. The promise of high coefficients of lift and thus more efficient power production by Madaras turbines certainly makes a case for their further development. Funding of a program to fully analyze and develop a Madaras turbine power plant could thus be extremely rewarding. Though further analysis will reveal more, the Madaras turbine may one day replace conventional HAWT turbines as the industry standard for the best and most preferred turbine design.

APPENDIX

A. 2D DATA

The following set of tables contains the data from the tests performed for the 2D analysis of a rotating cylinder. Plots of the cL values can be found in section II: 2D validation.

Table 7: 2D data for 1 meter cylinder including coefficient of lift

Density	1.2047		wd/2v	1	2	3	4	5
Dyn Visc	1.82E-05		w (rad/s)	10	20	30	40	50
Vel	5	m/s						
Diameter	1	m	P1	35.16	48.58	60.97	75.43	92.53
RE#	**3.31E+05**		P2	-3.47	1.12	3.65	5.06	5.59
			delP	38.63	47.45	57.32	70.37	86.94
			cL	2.57	3.15	3.81	4.67	5.77

Density	1.2047		wd/2v	1	2	3	4	5
Dyn Visc	1.82E-05		w (rad/s)	1.25	2.5	3.75	5	6.25
Vel	0.625	m/s						
Diameter	1	m	P1	0.63	1.31	2.02	2.76	3.38
RE#	**4.14E+04**		P2	0.00	0.03	-0.04	-0.16	-0.32
			delP	0.63	1.28	2.06	2.93	3.70
			cL	2.68	5.42	8.76	12.44	15.73

Density	1.2047		wd/2v	1	2	3	4	5
Dyn Visc	1.82E-05		w (rad/s)	5	10	15	20	25
Vel	2.5	m/s						
Diameter	1	m	P1	9.2119	14.2111	18.7677	23.2758	28.1516
RE#	**1.65E+05**		P2	-0.6404	0.5319	0.9337	0.9399	0.6736
			delP	9.8523	13.6792	17.834	22.3359	27.478
			cL	2.62	3.63	4.74	5.93	7.30

Density	1.2047		wd/2v	1	2	3	4	5
Dyn Visc	1.82E-05	kg/m*s	w (rad/s)	20	40	60	80	100
Vel	10	m/s						
Diameter	1	m	P1	135.791	179.122	213.906	266.94	330.126
RE#	**6.62E+05**		P2	-16.729	1.4845	13.1174	21.4482	26.6915
			delP	152.521	177.637	200.789	245.491	303.435
			cL	2.53	2.95	3.33	4.08	5.04

Density	1.2047		wd/2v	1	2	3	4	5
Dyn Visc	1.82E-05		w (rad/s)	2.5	5	7.5	10	12.5
Vel	1.25	m/s						
Diameter	1	m	P1	2.5344	4.4291	6.2996	7.7037	9.339
RE#	**8.27E+04**		P2	-0.065	0.2017	0.1639	-0.0297	-0.3114
			delP	2.5994	4.2274	6.1357	7.7334	9.6504
			cL	2.76	4.49	6.52	8.22	10.25

Density	1.2047		wd/2v	1	2	3	4	5
Dyn Visc	1.82E-05		w (rad/s)	130	260	390	520	650
Vel	65	m/s						
Diameter	1	m	P1	5606.28	7406.52	8607.59	10049.8	12548.2
RE#	**4.30E+06**		P2	-750.06	-75.202	465.441	919.903	1257.57
			delP	6356.34	7481.72	8142.15	9129.91	11290.6
			cL	2.50	2.94	3.20	3.59	4.44

The table below is similar to those above except that it has been configured using the Madaras parameters.

Table 8: 2D data for Madaras cylinder including coefficient of lift

Density	1.2047		wd/2v	1	2	3	4	5
Dyn Visc	1.82E-05		w (rad/s)	5.36	10.72	16.08	21.44	26.8
Vel	13.4	m/s						
Diameter	5	m	P1	1167.88	1471.46	1666.32	2053.16	2552.96
RE#	**4.43E+06**		P2	-159.15	1.60	126.87	236.70	319.14
			delP	1327.04	1469.86	1539.45	1816.46	2233.82
Madaras			cL	2.45	2.72	2.85	3.36	4.13

The following is a 2D study that varies the diameter and the relative speed ratio for a Reynolds number of 3.31e5. The results in the table are the coefficients of lift. As can be seen, there is no influence of diameter on the results – the relative speed ratio is the only variable that caused change in this study.

Table 9: Compiled coefficients of lifts

		ωd/2v				
		1	2	3	4	5
Diameter	0.5m	2.56	3.15	3.81	4.67	5.77
	1m	2.57	3.15	3.81	4.67	5.77
	2m	2.57	3.15	3.81	4.67	5.77

B. 2D MESH ANALYSIS

Before continuing on to data collection, it was determined that the mesh should be analyzed to determine the size and type that would best fit the problem. Unfortunately, computational resources were not available for the 3-dimensional analysis of multiple types of meshes, so it was done in 2-dimensions. The variable of most interest is the pressure difference between the positive-y side of the cylinder and the negative-y side of the cylinder, so the line integrals of the pressure acting upon both sides of the cylinder were computed. In the next two figures are plots showing how the mesh type and size affected the results.

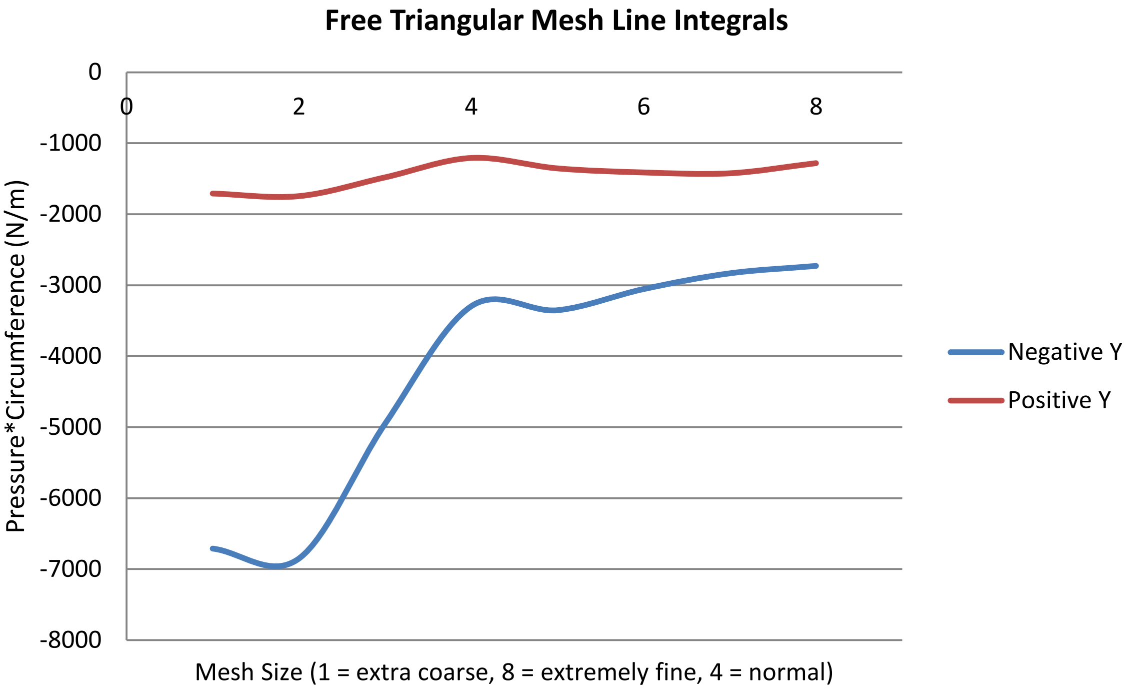

Figure 54: Free triangular mesh line integrals

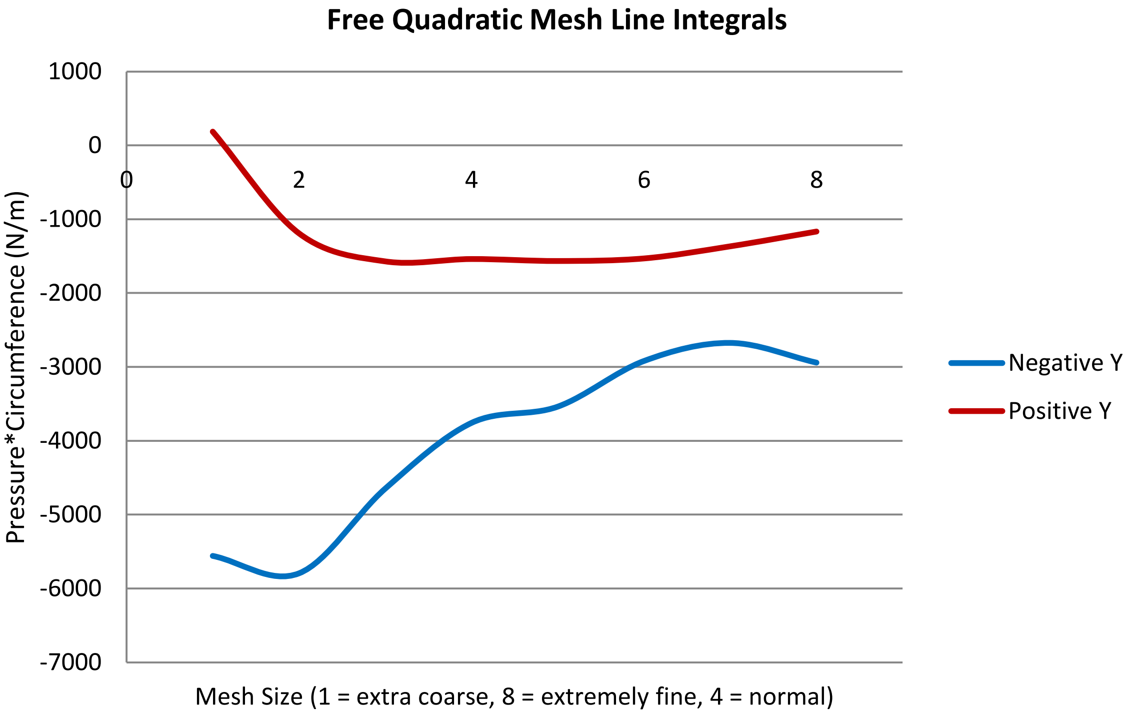

Figure 55: Free quadratic mesh line integrals

When reading the graphs, it is important to keep in mind that the quantity shown is the line integral of the pressure, which is why the units are N/m (or Pa*m). Thus, if the difference between the positive-y side and the negative-y sides was computed and then multiplied by 38.1 m, the total lateral force on the cylinder could be calculated assuming that the cylinder were infinitely long. An additional key point of the graphs is the labeling of the x-axis. This axis contains the mesh size ranging from extra coarse to extremely fine where 4 is normal (the extremely coarse mesh size was left out of this analysis since it would likely add no insight).

As expected, both graphs flatten out as the mesh size becomes increasingly finer. Importantly, the difference between the two pressure integrals is nearly the same for both graphs after the mesh becomes sufficiently fine. However, the quadratic meshes do not flatten out nearly as much as the triangular mesh. In addition, the triangular meshes reach a consistent pressure difference more quickly than the quadratic meshes (the pressure difference in the quadratic mesh graph fluctuates a little at the very end). For these two reasons, a triangular mesh was chosen for the remainder of the studies that was at least no more coarse than the predefined "normal" mesh size.

C. CYLINDER SPACING

Below is a table showing all the values measured across the cylinders. The "1" in the titles signifies the first cylinder, or the cylinder upstream in the flow, and the "2" signifies the second cylinder. The most important quantities displayed are the pressures across the cylinders since they determine the lift that a cylinder can generate. The velocities taken around the cylinders at a diameter of 2 meters were also calculated for comparison and to help determine where the cylinders are sufficiently separated (similar values for both cylinder 1 and cylinder 2).

Table 10: Vertical cylinder spacing data

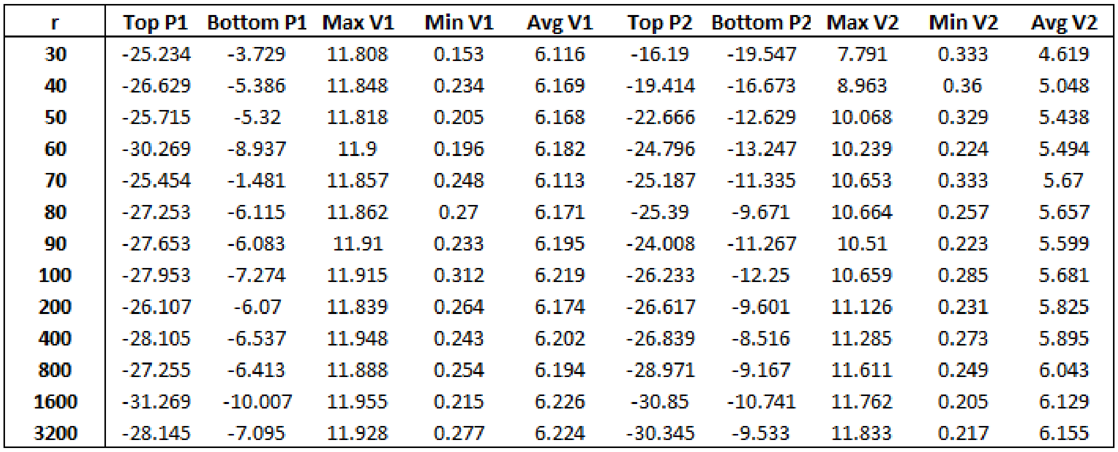

r	Top P1	Bottom P1	Max V1	Min V1	Avg V1	Top P2	Bottom P2	Max V2	Min V2	Avg V2
30	-25.234	-3.729	11.808	0.153	6.116	-16.19	-19.547	7.791	0.333	4.619
40	-26.629	-5.386	11.848	0.234	6.169	-19.414	-16.673	8.963	0.36	5.048
50	-25.715	-5.32	11.818	0.205	6.168	-22.666	-12.629	10.068	0.329	5.438
60	-30.269	-8.937	11.9	0.196	6.182	-24.796	-13.247	10.239	0.224	5.494
70	-25.454	-1.481	11.857	0.248	6.113	-25.187	-11.335	10.653	0.333	5.67
80	-27.253	-6.115	11.862	0.27	6.171	-25.39	-9.671	10.664	0.257	5.657
90	-27.653	-6.083	11.91	0.233	6.195	-24.008	-11.267	10.51	0.223	5.599
100	-27.953	-7.274	11.915	0.312	6.219	-26.233	-12.25	10.659	0.285	5.681
200	-26.107	-6.07	11.839	0.264	6.174	-26.617	-9.601	11.126	0.231	5.825
400	-28.105	-6.537	11.948	0.243	6.202	-26.839	-8.516	11.285	0.273	5.895
800	-27.255	-6.413	11.888	0.254	6.194	-28.971	-9.167	11.611	0.249	6.043
1600	-31.269	-10.007	11.955	0.215	6.226	-30.85	-10.741	11.762	0.205	6.129
3200	-28.145	-7.095	11.928	0.277	6.224	-30.345	-9.533	11.833	0.217	6.155

In the table to the right, the differences in pressure across a cylinder in Pascals are denoted for various separation distances in meters. As the separation distance increases, the values converge to approximately 21 Pa, which is near the average of the pressure difference across the first cylinder of 21.3 Pa. It should be noted that for a separation distance of 30 meters, the second cylinder actually has a pressure gradient acting in the wrong direction. This placement of the second cylinder is clearly much too close to the first cylinder to make an effective Madaras turbine. It seems like the minimum necessary separation distance before getting reasonable results is about 400 meters. Although the value for the pressure difference at 400 meters is still 85.9% that of the first cylinder value, this is a much more reasonable distance to separate the cylinders than 3200, which provides a better pressure difference.

Table 11: Cylinder pressure differences for both cylinders

r	DelP1	DelP2
30	21.505	-3.357
40	21.243	2.741
50	20.395	10.037
60	21.332	11.549
70	23.973	13.852
80	21.138	15.719
90	21.57	12.741
100	20.679	13.983
200	20.037	17.016
400	21.568	18.323
800	20.842	19.804
1600	21.262	20.109
3200	21.05	20.812

The table below shows the percent deviation in various variables when comparing the second cylinder against the first cylinder. This was used as another way to determine whether the cylinders were sufficiently separated so that they could be called independent. For a separation distance of only 30 meters, the average deviation is 127.2%, which is extremely high. However, as the distance increases, the average deviation decreases to just over 10%.

Table 12: Percent deviation for various calculated variables between cylinders as vertical separation distance changes

Separation Distance (m)	%Dev Top Pressure	%Dev Bottom Pressure	%Dev Max. Velocity	%Dev Min. Velocity	%Dev Avg. Velocity	Average % Deviation
30	35.8%	424.2%	34.0%	117.6%	24.5%	127.2%
40	27.1%	209.6%	24.4%	53.8%	18.2%	66.6%
50	11.9%	137.4%	14.8%	60.5%	11.8%	47.3%
60	18.1%	48.2%	14.0%	14.3%	11.1%	21.1%
70	1.0%	53.2%	10.2%	34.3%	7.2%	21.2%
80	6.8%	58.2%	10.1%	4.8%	8.3%	17.6%
90	13.2%	85.2%	11.8%	4.3%	9.6%	24.8%
100	6.2%	68.4%	10.5%	8.7%	8.7%	20.5%
200	2.0%	58.2%	6.0%	12.5%	5.7%	16.9%
400	4.5%	30.3%	5.5%	12.3%	5.0%	11.5%
800	6.3%	42.9%	2.3%	2.0%	2.4%	11.2%
1600	1.3%	7.3%	1.6%	4.7%	1.6%	3.3%
3200	7.8%	34.4%	0.8%	21.7%	1.1%	13.1%

REFERENCES

AWEA U.S. Wind Industry First Quarter 2012 Market Report. Rep. American Wind Energy Association, Apr. 2012. Web. 26 May 2012. <http://www.awea.org/learnabout/publications/reports/upload/AWEA_First_Quarter_2012_Market_Report_Public.pdf>.

Batchelor, G. K. (1967). *An Introduction to Fluid Dynamics*, p 406

Bernard, P. S. and J. M. Wallace (2002). *Turbulent Flow: Analysis, Measurement, and Prediction*. Hoboken, NJ: John Wiley & Sons.

Buhl, M. "Wind Turbine Airfoil List." National Renewable Energy Laboratory, 21 Oct. 2009. Web. 16 June 2012. <http://wind.nrel.gov/airfoils/AirfoilList.html>.

Drakos, Nikos. "6.2.2 Determining Turbulence Parameters." *Fluent 6.1 Documentation*. Fluent Incorporated. Web. 15 Oct. 2011. <http://jullio.pe.kr/fluent6.1/help/html/ug/node178.htm>.

Ferziger, J. H. and M. Perić (2002). *Computational Methods for Fluid Dynamics*. Berlin, Germany: Springer-Verlag.

Filon, L. N. G. (1926). “The forces on a cylinder in a stream of viscous fluid.” *Proceedings of the Royal Society of London A*, 113, 7-27.

Firoz, A., H. Ho, H. Chowdhury, and A. Subic (2011). “Aerodynamics of Baseball.” *5th Asia-Pacific Congress on Sports Technology (APCST).*

Gibson, B., C. Cox, C. Hendrix, and Y. Dwant (2010). “The Madaras wind power plant: history and modernization.” Internal Report, Mechanical Engineering Dept. Vanderbilt Univ.

Glauert, M. B. (1957). “The flow past a rapidly rotating circular cylinder.” *Proceedings of the Royal Society of London A*, 242(1228), 108-115.

Hoerner, S. F. and H. V. Borst (1985). *Fluid-Dynamic Lift: Practical Information on Aerodynamic and Hydrodynamic Lift*. New York, NY: Hoerner Fluid Dynamics.

Ingham, D. B. and T. Tang (1990). “A numerical investigation into the steady flow past a rotating circular cylinder at low and intermediate Reynolds numbers.” *Journal of Computation Physics*, 87(1), 91-107.

Ishihara, Takeshi (2010). “Guidelines for Design of Wind Turbine Support Structures and Foundation December 2010.” *Task Committee of Structural Engineering, Japan Society of Civil Engineers,* 80-96.

Kollár, L., and E. Dulácska (1984). "Buckling of Cylindrical Shells." *Buckling of Shells for Engineers*. Budapest: Akadémiai Kiadó. 20-58. Print.

Layton, Julia (2006). "Modern Wind-power Technology." *HowStuffWorks*. N.p., n.d. Web. 17 June 2011. <http://science.howstuffworks.com/environmental/green-science/wind-power2.htm>.

Lichtabch, M., S. Little, C. Knapp, M. Goudreault, J. Hess, and M. Kostrzewa. "Colorado Anemometer Loan Program." *Colorado State University*. N.p., June 2009. Web. 17 June 2012. <http://www.engr.colostate.edu/ALP/ALP_96_Joes.html>.

Manville, Albert M. "Towers, Turbines, Power Lines, and Buildings - Steps Being Taken by the U.S. Fish and Wildlife Service to Avoid or Minimize Take of Migratory Birds at These Structures." Partners in Flight, n.d. Web. 15 Sept. 2012. <http://www.partnersinflight.org/pubs/mcallenproc/articles/pif09_anthropogenic%20impacts/manville_pif09.pdf>.

McCormac, Jack C. (2008). "Introduction to Axially Loaded Compression Members." *Structural Steel Design*. Upper Saddle River, NJ: Pearson/Prentice Hall. 127-95. Print.

Mehmetoglu, S., WIPO Patent Application No. 2008/111922. 18 September 2008.

Mittal, S. and K. Bhaskar (2003). “Flow past a rotating cylinder.” *Journal of Fluid Mechanics*, 476, 303-334.

"NACA 4412 Charateristics." NACA 4412 Charateristics. N.p., n.d. Web. 15 Sept. 2012. <http://library.propdesigner.co.uk/html/naca_4412_charateristics.html>.

Nair, M. T., T. K. Sengupta, and U. S. Chauhan (1997). “Flow past rotating cylinders at high Reynolds numbers using higher order upwind scheme.” *Computers and Fluids*: 27(1), 47-70.

Nunn, R. H. (1989). *Intermediate Fluid Mechanics*. New York, NY: Hemisphere Publishing Corporation.

"Overview of Materials for AISI 4000 Series Steel." *Overview of Materials for AISI 4000 Series Steel*. MatWeb: Material Property Data. Web. 03 Sept. 2011. <http://www.matweb.com/search/DataSheet.aspx?MatGUID=210fcd12132049d0a3e0cabe7d091eef>.

Ragheb, M. (2010). “Wind energy converters concepts.”

Rhodes, Ed J. and A. C. Walker (1987). "Lower Bound Methods in Shell Buckling." *Developments in Thin-Walled Structures*.Vol. 3. London: Elsevier Applied Science. 117-65. Print.

Salter, S., G. Sortino, and J. Lantham (2008). “Sea-going hardware for the cloud albedo method of reversing global warming.” *Philosophical Transactions of the Royal Society A*, 366, 3989-4006.

Stojković, D., M. Breuer, and R. Durst (2002). “Effect of high rotation rates on the laminar flow around a circular cylinder.” *Physics of Fluids*, 14(9), 3160-3198.

Tang, T. and D.B. Ingham (1991). “On steady flow past a rotating circular cylinder at Reynolds numbers 60 and 100.” *Computers & Fluids*, 19(2), 217-230.

United States of America. U.S. Navy. Department of Naval Sea System Command. *The Magnus Effect: An Overview of Its Past and Future Practical Applications*. By J. Borg. Atascadero, CA: Borg-Luther Group, 1986. Print.

"Visual Impact." *Molonglo Landscape Guardians*. N.p., 13 Dec. 2008. Web. 22 Sept. 2012. <http://www.mlg.org.au/visual.htm>.

Wendt, J. F. (2009). *Computational Fluid Dynamics: An Introduction*. Berlin, Germany: Springer-Verlag.

Weng, M., P. Catalano, and G. Iaccarino (2001). “Prediction of high Reynolds number flow over a circular cylinder using LES with wall modeling.” *Center for Turbulence Research: Annual Research Briefs 2001*.

Whitford, D. H., J. E. Minardi, B. S. West, and R. J. Dominic (1978). “An analysis of the Madaras rotor power plant: an alternative method for extracting large amounts of power from the wind.” *DOE Report DSE-2554-78/2*, Vol. 2.

"Wind Energy." *NRDC: Renewable Energy for America: Wind*. Natural Resources Defense Council. Web. 04 June 2012. <http://www.nrdc.org/energy/renewables/wind.asp>.

"Wind Energy Resource Atlas of the United States." *Wind Energy Resource Atlas of the United States*. National Renewable Energy Laboratory. Web. 20 May 2012. <http://rredc.nrel.gov/wind/pubs/atlas/maps/chap2/2-01m.html>.

"Winglets." *Winglets*. Ed. Tom Benson. National Aeronautics and Space Administration, 02 Aug. 2010. Web. 17 May 2012. <http://www.grc.nasa.gov/WWW/k-12/airplane/winglets.html>.